LONG-TIME SOLUTIONS FOR BLOOD FLOW IN A PIPE

AZADEH ELAHIAN

A THESIS SUBMITTED TO THE FACULTY OF GRADUATE STUDIES
IN PARTIAL FULFILMENT OF THE REQUIREMENTS
FOR THE DEGREE OF
MASTERS OF SCIENCE

GRADUATE PROGRAM IN MATHEMATICS AND STATISTICS
YORK UNIVERSITY
TORONTO, ONTARIO

MAY 2025

Abstract

This thesis presents an efficient Chebyshev-tau spectral solver solver to compute numerical solutions of the equations of motion of a viscous fluid in a circular pipe subject to the generalized Oldroyd-B stress model of Yeleswarapu [1] corresponding to the flow of a viscoelastic fluid with a shear rate dependent viscosity function. The code relies on an explicit fourth order Runge-Kutta time stepping procedure with $\mathcal{O}(N \log N)$ operations per time step enabled by the use of fast cosine transforms. The resulting code is spectrally accurate in the number of spatial discetization points N. This solver is a significant improvement to what was previously available for this problem [1] and allows us to compare solutions corresponding to different shear rate dependent viscosity models by Powell-Eyring, Yeleswarapu and Carreau over long evolution times.

Dedication

I dedicate this thesis to my mom and dad who devoted their lives to me, and I appreciate their nonstop support.

Acknowledgements

I am grateful to the Natural Sciences and Engineering Research Council of Canada for funding me throughout my M.Sc. program. I am also grateful to the Agent-Based Modelling Laboratory at York University for supplying computational resources.

Table of Contents

List of Tables

List of Figures

Chapter 1

Introduction

1.1 A Background on the Analysis of Blood Flow

The problem of oscillatory flow in a tube is of fundamental importance in biomedical engineering and has numerous applications in other branches of the physical sciences. While in the past oscillating flow has been studied almost exclusively in connection with blood flow, other applications have been found in the super-charging system of reciprocating engines and surging in power plants [2]. More recently, oscillating flows have been investigated for conservation purposes such as the enhancement of heat transfer [3]. It has also been suggested that introducing an oscillating pressure gradient may even delay the onset of turbulence. An excellent review of modern approaches to blood flow problems is given by Ku [4].

Much of the early mathematical analysis of blood flow is based on the assumptions of a Newtonian fluid and circular pipes. Oscillating flow in circular tubes was investigated by Sexl [5], Uchida [2], and Womersley [6]. Sexl introduced the first expressions describing oscillating flow in rigid circular tubes subject to a single harmonic pressure gradient. The theory was subsequently extended to multiple harmonics in the pressure by Uchida and to circular elastic tubes by Womersley. These studies, which resulted in relatively simple analytical expressions describing the flow quantities, were useful to practitioners in rheology in order to understand basic properties of the flows.

Later studies of blood flow began to document essential non-Newtonian features of the fluid [4]. Firstly, experiments have conclusively demonstrated that the viscosity of blood is highly dependent on the local shear rates of the fluid [7]. Such a dependence is not captured by the Newtonian model for stress, requiring a more complex constitutive relation for the viscous stress. One of the simplest ways of including the effects of shear rate dependence is through a model for a generalized Newtonian fluid, which relates the stress tensor and deformation rate tensor via a viscosity function (as opposed to a constant viscosity in the Newtonian case) [7, 8].

Blood is also known to display strong visco-elastic properties, particularly in small vessels. Viscoelastic fluids are a type of non-Newtonian fluid formed by a viscous component and an elastic one. In the case of blood, the viscous component arises through the viscosity of blood plasma, while the elastic component arises from the deformation of red blood cells [8]. There have been several attempts to include viscoelastic properties in a constitutive relation for the viscous stress but Oldroyd's 1950 article [9] is the first attempt to formulate constitutive models for viscoelastic fluids in a way that respects material frame indifference. An excellent review of the history of the problem as well as the current state of research in Oldroyd-B fluids is given by Renardy [10].

Since blood is known to exhibit both a dependence on local shear rates as well as viscoelastic properties, there have been efforts towards incorporating both in so-called generalized Oldroyd-B stress models. Models were proposed by Yeleswarapu [1], Anand and Rajagopal [11], Sun and DeKee [12], Owens [13] and others. Yeleswarapu's model, which showed good agreement with experimental data is an extension of the standard Oldroyd-B model where a shear rate dependence is included in way analogous to generalized Newtonian models. Yeleswarapu's generalized Oldroyd-B model includes both important effects of local shear rate dependence and viscoelasticity, has been shown to agree well with experimental data, and lends itself well to high-order numerical approximation. Yeleswaapu's model therefore forms the basis of the numerical algorithms developed in this thesis.

1.2 Present Work

The purpose of the present work is to develop a robust and accurate numerical solver using Yeleswarapu's generalized Oldroyd-B model for viscous stress in order to examine the long-time behaviour of the flows subject to different (but well-known) models for the dependence of viscosity on the local shear rates. Previous solvers for this problem [1, 14] based on finite difference methods in the former study or an expansion in terms of Legendre polynomials in the latter, required an iteration at each time step to resolve the nonlinear terms and were prohibitively slow and low order in the time stepping. These drawbacks, in turn, limited the use of previous algorithms for studying the flow, especially its long-time behaviour, in detail. Our belief is that the Yeleswarapu model, even when restricted to simple assumptions on the geometry, is of significant interest to practitioners in rheology, but the absence of a simple and effective approach to compute solutions presents a major roadblock in its use; we aim to remedy this issue in the present work.

This thesis presents an efficient Chebyshev-tau spectral solver solver to compute numerical solutions of the equations which result from Yeleswarapu's stress model while simultaneously using different models for the viscosity in a comparative study. Our algorithm relies on a fourth order Runge-Kutta time stepping procedure with $\mathcal{O}(N \log N)$ operations per time step enabled by the use of fast cosine transforms. The resulting code is spectrally accurate in the number of spatial discetization points N.

1.3 Basic Principles and Assumptions

Problems related to blood flow in the cardiovascular system are accompanied by a large array of difficulties which must be overcome to completely describe the behaviour of the fluid. Many of these difficulties, however, are not commonly encountered in scientific applications. Among these factors are the pulsation of the flow, elastic walls, non-Newtonian fluids, vessel tapering, wave reflections, and non-circular cross-sections. All of these factors interact in the determination of the flow characteristics in the blood vessel system. In order to obtain quantitative results from a relatively simple model that does not require the application of high-performance computing, it is necessary to adopt an idealization of the flow. In our case, we greatly simplify the vessel geometry, representing it by a long straight rigid circular tube. While some of the complexities listed above will not be accounted for in the model, many important features specifically related to the viscous stress will indeed be retained. We believe the simplified model (and corresponding numerical results) should still remain useful in predicting important flow features.

1.4 Outline of the Thesis

The remainder of this thesis is organized as follows. In Chapter 2 we review the mathematical formulation of blood flow problems, including viscous stress models which retain physical features specific to this problem. In particular, models for a shear rate dependent viscosity are presented in the context of generalized Newtonian fluids; models for visco-elastic fluids are presented in terms of the classic Oldroyd-B stress model; finally, a generalization of the Oldroyd-B model which combines both a shear rate dependent viscosity in addition to visco-elastic effects is presented and this model will form the basis for the analysis in this thesis.

In Chapter 3 we specialize our model for generalized Oldroyd-B fluids to flow in long straight circular tubes. As we detail, this simplification in geometry reduces the full vector and tensor equations applicable to the general problem to a coupled set of three nonlinear partial differential governing equations which form the basis for the numerical investigations in this thesis.

In Chapter 4 we produce analytical solutions of the (usually) nonlinear governing equations in the special case of constant viscosity. In this case, our Generlized Oldroyd-B model reduces to the standard Oldroyd-B model and expressions for the flow quantities are derived in terms of Bessel functions. These exact expressions are useful to validate our numerical code for these specific cases.

In Chapter 5 we review essential elements of Chebyshev approximation, which form the basis for the spatial treatment of our problems. In particular, we define fast transform pairs applicable to data sampled at the zeros of Chebyshev polynomials. We then review well-known algorithms for numerical integration and differentiation of data defined as a Chebyshev series.

In Chapter 6 we present a Chebyshev-tau method combined with 4th order Runge-Kutta time stepping for the numerical solution of the problem. This formulation requires a special formulation of the boundary conditions. The stability of the algorithm is investigated.

In Chapter 7 we provide several examples detailing the performance of our numerical implementation for cases of low, moderate and high Womersley numbers (an analogue to the Reyolds number for oscillatory flows). Finally in Chapter 8 we summarize our results and propose how this work can be extended in future directions.

Chapter 2

Stress and Viscosity Models

2.1 Continuum Equations

The continuum equations (i.e., the equations of motion of a fluid) are derived by enforcing a balance of momentum of a viscous fluid in a region $\Omega \subseteq \mathbb{R}^3$; see, for example, [15]. We thus obtain

$$\frac{\partial \mathbf{u}}{\partial t} + \mathbf{u} \cdot \nabla \mathbf{u} = \frac{1}{\rho} \nabla \cdot \mathbf{T}, \tag{2.1}$$

where $\mathbf{u} = \mathbf{u}(\mathbf{r}, t)$ is the fluid velocity at location $\mathbf{r} \in \Omega$, $\mathbf{T} = \mathbf{T}(\mathbf{r}, t)$ is the Cauchy stress tensor and $\rho = \rho(\mathbf{r}, t)$ is the fluid density, which we assume is a constant throughout this work. The required boundary conditions for this problem are taken as no-slip conditions $\mathbf{u} = \mathbf{0}$ for $\mathbf{r} \in \partial\Omega$. In some circumstances, it may also be necessary to impose conditions that the stress and velocity fields remain finite for all $\mathbf{r} \in \Omega$. Initial conditions are also required; when needed in this work we will take these to be a flow at rest, i.e. all field quantities are set to zero. The continuum equations are typically supplemented with an equation enforcing conservation of mass, which follows directly from enforcing a vanishing velocity flux over the surface of the fluid region $\partial\Omega$, and subsequently results in a vanishing divergence throughout Ω as a consequence of Gauss' theorem. We thus obtain the incompressibility constraint (or mass continuity constraint)

$$\nabla \cdot \mathbf{u} = 0. \tag{2.2}$$

To properly understand why the stress is represented by a rank 2 tensor $\mathbf{T}$, we note that this quantity represents a force per unit area. Consequently, there are two directions associated with stress: the direction of the force and the direction (or orientation) of the area. In three-dimensional rectangular coordinates, for example, the stress tensor can be arranged in the matrix form as

$$\mathbf{T} = \begin{bmatrix} \tau_{xx} & \tau_{xy} & \tau_{xz} \\ \tau_{yx} & \tau_{yy} & \tau_{yz} \\ \tau_{zx} & \tau_{zy} & \tau_{zz} \end{bmatrix}. \tag{2.3}$$

The various components of $\mathbf{T}$ are depicted in Figure 2.1. The components of stress normal to a coordinate plane are τ_{xx}, τ_{yy} and τ_{zz} and these are referred to as normal stresses. The stress components that act perpendicular to these normals (i.e. τ_{xy}, τ_{yx}, τ_{xz}, τ_{zx}, τ_{yz}, τ_{zy}) are known as shear stresses. The convention is that the first subscript of the stress component τ_{ij} tells us the direction in which the area faces, and the second subscript tells us the direction of the force component on that face.

As is well-known the Cauchy stress tensor $\mathbf{T} = \mathbf{T}(\mathbf{r}, t)$ can be expressed as

$$\mathbf{T} = -p\mathbf{I} + \mathbf{S}, \tag{2.4}$$

where $\mathbf{S} = \mathbf{S}(\mathbf{r}, t)$ is known as the extra stress tensor or deviatoric stress tensor, $\mathbf{I}$ is the identity tensor and $p = p(\mathbf{r}, t)$ is the fluid pressure. The extra stress tensor $\mathbf{S}$ can easily be written in a matrix form similar to equation (2.3). The continuum equations (2.1) actually apply to both fluids and solids; the specification of the problem to fluids is accomplished by defining how the stress is related to local deformation rates through a constitutive relation. Constitutive relations are empirical in nature and indeed, these are at their essence a model for the stress applicable to various different physical problems. Application of these models typically reduces the number of unknowns in the problem, allowing for solution.

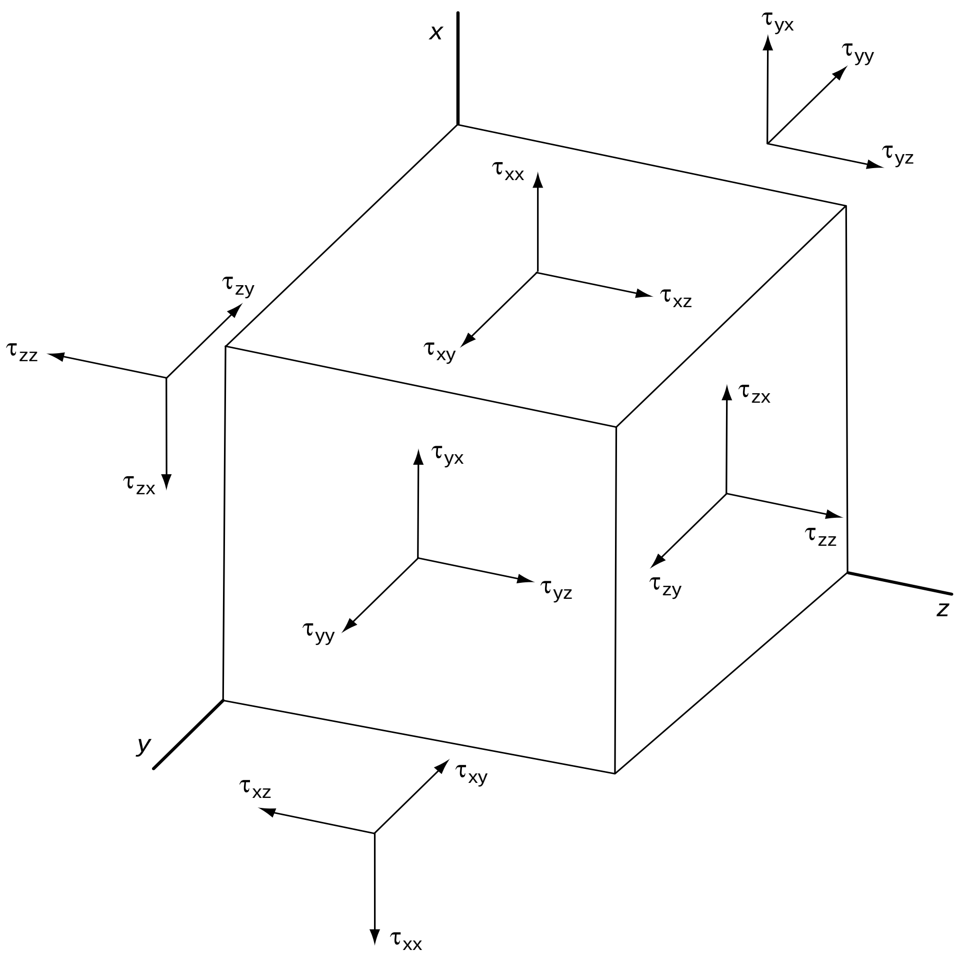

Figure 2.1: Positive directions of Cauchy stress components τ_{ij} in three-dimensional rectangular coordinates. From [16]

2.2 Newtonian Fluids

For a broad array of important fluids (e.g. water, air, alcohol), we can adopt a simple constitutive relation defining the relationship between the stress and the local deformation rates. Indeed, for a homogeneous isotropic incompressible fluid it can be assumed that the stress is linearly dependent on local deformation rates, i.e.,

$$\mathbf{S} = 2\mu\mathbf{D}, \tag{2.5}$$

where the deformation rate tensor $\mathbf{D} = \mathbf{D}(\mathbf{r}, t)$ is given in terms of the velocity gradient tensor as [15]

$$\mathbf{D} = \frac{1}{2}\left(\nabla\mathbf{u} + (\nabla\mathbf{u})^T\right). \tag{2.6}$$

It should be clear from equation (2.6) that the deformation rate tensor is symmetric, and therefore so is the stress tensor (2.5). The constant of proportionality μ in equation (2.5), known as the coefficient of viscosity, is determined experimentally. Under these assumptions the momentum balance (2.1) together with the mass continuity constraint (2.2) yield the celebrated Navier-Stokes equations for an incompressible fluid:

$$\begin{aligned} \frac{\partial\mathbf{u}}{\partial t} + (\mathbf{u}\cdot\nabla)\mathbf{u} &= -\frac{1}{\rho}\nabla p + \frac{\mu}{\rho}\nabla^2\mathbf{u}, \\ \nabla\cdot\mathbf{u} &= 0. \end{aligned} \tag{2.7}$$

While the Navier-Stokes equations represent the 'gold standard' for fluid fluid models in many important situations, they are not suitable in all contexts, in particular blood flow.

2.3 Generalized Newtonian Fluids and Shear Rate Dependence

As is well-known, blood flow exhibits a dependence on local shear rates of the fluid [7, 8]. Such a dependence is not captured by the Newtonian model, requiring a more complex constitutive relation. One of the simplest ways of including the effects of shear rate dependence is through a model for a generalized Newtonian fluid, which relates the stress tensor and deformation rate tensor via a viscosity function (as opposed to a viscosity constant in the Newtonian case) as [7, 8]

$$\mathbf{S} = 2\mu(\dot{\gamma})\mathbf{D}. \tag{2.8}$$

The quantity $\dot{\gamma}$, on which the viscosity explicitly depends, is known as the shear rate (a measure of the rate of deformation). The shear rate is defined in terms of the trace of the deformation rate tensor as [8]

$$\dot{\gamma} = \sqrt{2\mathrm{Tr}(\mathbf{D}^2)} = \sqrt{-4\mathbf{II}_D}. \tag{2.9}$$

The quantity $\mathbf{II}_D$, which appears in equation (2.9), denotes the second principal invariant of the tensor $\mathbf{D}$ and is given by [8]

$$\mathbf{II}_D = \frac{1}{2}\left((\mathrm{Tr}(\mathbf{D}))^2 - \mathrm{Tr}(\mathbf{D}^2)\right). \tag{2.10}$$

Later in the development of this work we will take the shear rate to be the absolute value of a smooth odd function $\dot{\gamma} = |A(r,t)|$.

Viscosity functions can be written in the general form

$$\mu(\dot{\gamma}) = \mu_\infty + (\mu_0 - \mu_\infty)F(\dot{\gamma}), \tag{2.11}$$

where μ_0 and μ_∞ are the asymptotic viscosity values at zero and infinite shear rates, respectively. The non-dimensional viscosity function $F(\dot{\gamma})$ smoothly transitions the viscosity from

μ_0 to μ_∞ as a function of the shear rate. Asymptotic viscosity values applicable to blood flow and consistent with other experimentally determined values for the parameters listed below are $\mu_0 = 0.056$ Pa·s and $\mu_\infty = 0.00345$ Pa·s, leading to the ratio $\beta = \mu_\infty/\mu_0 = 0.0616$, which is used later in this work. Following immediately from equation (2.11), the non-dimensional viscosity function can be expressed as

$$F(\dot{\gamma}) = \frac{\mu(\dot{\gamma}) - \mu_\infty}{\mu_0 - \mu_\infty}. \tag{2.12}$$

In order to properly transition the viscosity between its asymptotic values, the non-dimensional function (2.12) must satisfy the following natural limit conditions

$$\lim_{\dot{\gamma}\to 0} F(\dot{\gamma}) = 1 \qquad \text{and} \qquad \lim_{\dot{\gamma}\to\infty} F(\dot{\gamma}) = 0. \tag{2.13}$$

Different choices of the function $F(\dot{\gamma})$ correspond to different models for the shear rate dependence of the fluid. We will summarize below some common viscosity models that have been considered in the literature for application to blood flows.

A very well-known example of the non-dimensional viscosity function corresponds to the Powell-Eyring model, and is given by

$$F_1(\dot{\gamma}) = \frac{\sinh^{-1}(\Lambda\dot{\gamma})}{\Lambda\dot{\gamma}}. \tag{2.14}$$

The shear thinning parameter Λ which appears in the Powell-Eyring model (and other models below) has typical values $\Lambda = 5.383$ sec in blood flow applications when used with the Powell-Eyring model [8]. In order to compare the Powell-Eyring model with other shear thinning models below, it's useful to examine its asymptotic behavior. Indeed, in the limit $z \to 0$, where we temporarily replace $z = \dot{\gamma}$, we have

$$F_1(z) = 1 - \frac{1}{6}(\Lambda z)^2 + \mathcal{O}(\Lambda z)^4. \tag{2.15}$$

On the other hand, for $z \to \infty$ we have

$$F_1(z) \sim \frac{\ln(\Lambda z)}{\Lambda z} + \frac{\ln 2}{\Lambda z} + \mathcal{O}\left(\frac{1}{(\Lambda z)^3}\right). \tag{2.16}$$

Clearly the Powell-Eyring model (2.14) satisfies the natural limit conditions in equation (2.13). Note also that model (2.14) is an even function of $z = \dot{\gamma}$.

Another more recent shear thinning model is due to Yeleswarapu [1] and is given by

$$F_2(\dot{\gamma}) = \frac{1 + \ln(1 + \Lambda\dot{\gamma})}{1 + \Lambda\dot{\gamma}}. \tag{2.17}$$

The authors showed that this model is a good fit for experimental data [1]. They determine the shear thinning parameter for porcupine blood to be $\Lambda = 11.14$ sec, although we will adopt slightly different values in what follows in order to compare shear thinning models. In the limit $z \to 0$ the Yeleswarapu model gives

$$F_2(z) = 1 - \frac{1}{2}(\Lambda z)^2 + \frac{5}{6}(\Lambda z)^3 + \mathcal{O}(\Lambda z)^4. \tag{2.18}$$

On the other hand, for $z \to \infty$ we have

$$F_2(z) \sim \frac{\ln(\Lambda z)}{\Lambda z} + \frac{1}{\Lambda z} + \mathcal{O}\left(\frac{\ln(\Lambda z)}{(\Lambda z)^2}\right). \tag{2.19}$$

Clearly the Yeleswarapu model (2.17) also satisfies the natural limit conditions in equation (2.13) and the dominant terms in both expansions (2.18) and (2.19) match those corresponding to the Powell-Eyring model. Indeed, both the Powell-Eyring and Yeleswarapu models are very similar with one subtle difference we would like to point out. Notice from equation (2.18) that the Yeleswarapu model is not strictly even about $z = 0$. That means that when $z = \dot{\gamma} = |A(r,t)|$ the third derivative of the function is continuuous but the fourth derivative is singular. Such singularities cannot be physical and have implications for the convergence rates of the numerical algorithms applied; while the limitations are not severe in this case, a spectral convergence rate in the numerical algorithm cannot be achieved as a result. Viscosity

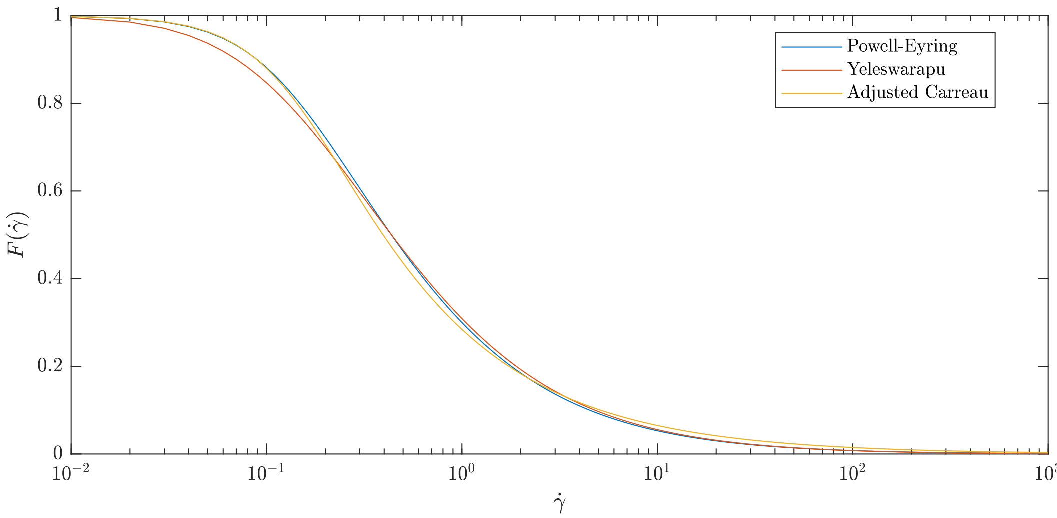

Figure 2.2: Non-dimensional viscosity functions corresponding to the Powell-Eyring, Yeleswarapu and Adjusted Carreau models with $\Lambda = 10$. The horizontal axis is plotted on a logarithmic scale.

models that are even functions of $\dot{\gamma}$ do not suffer from these self-inflicted problems and are likely more physically realistic models on that basis.

Lastly, we examine the Carreau model defined by the non-dimensional viscosity function

$$F_3(\dot{\gamma}) = \left(1 + (\Lambda\dot{\gamma})^2\right)^{-(1-n)/2}. \tag{2.20}$$

The parameters Λ and n which appear in the Carreau model have typical values $\Lambda = 3.313$ sec with $n = 0.3568$ in blood flow applications [8]. In the limit $z \to 0$ the Carreau model gives

$$F_3(z) = 1 - \frac{1-n}{2}\,(\Lambda z)^2 + \mathcal{O}(\Lambda z)^4. \tag{2.21}$$

On the other hand, for $z \to \infty$ we have

$$F_3(z) \sim \left(\frac{1}{\Lambda z}\right)^{1-n} - \frac{1-n}{2}\left(\frac{1}{\Lambda z}\right)^{3-n} + \mathcal{O}\left(\frac{1}{\Lambda z}\right)^{5-n}. \tag{2.22}$$

Clearly for the natural limit conditions in equation (2.13) to be satisfied in the limit $z \to \infty$

we require $n < 1$. Note also that model (2.20) is an even function of $z = \dot{\gamma}$.

In order to conduct what we feel is an apples-to-apples comparison of the last three models, we introduce an adjustment to the Carreau model (2.20) to improve it's agreement with the Powell-Eyring and the Yeleswarapu models. Using $n = 0.3568$ as before we define the Adjusted Carreau model as

$$F_4(\dot{\gamma}) = \left(1 + (0.7\Lambda\dot{\gamma})^2\right)^{-0.3216}. \tag{2.23}$$

Plots of the Powell-Eyring, Yeleswarapu and Adjusted Carreau models generated by evaluating these functions in Matlab are shown in Figure 2.2 using the parameter $\Lambda = 10$.

2.4 The Oldroyd-B Stress Model and Viscoelastic Fluids

Blood has complex mechanical properties that are not adequately described under the assumptions of a Newtonian fluid, particularly in small vessels. In addition to the shear thinning effects discussed in the previous section, blood is known to exhibit viscoelastic properties. Viscoelastic fluids are a type of non-Newtonian fluid formed by a viscous component and an elastic one. In the case of blood, the viscous component arises through the viscosity of blood plasma, while the elastic component arises from the deformation of red blood cells [8].

There have been several attempts to include viscoelastic properties in a constitutive relation but Oldroyd's 1950 article [9] is the first attempt to formulate constitutive models for viscoelastic fluids in a way that respects material frame indifference. The principle of material frame indifference is an important concept in continuum mechanics. This principle embodies the idea that constitutive laws describing the behaviour of a material should be independent of the frame of reference or the motion of the observer. An excellent review of the history of viscoelastic models as well as the current state of research in Oldroyd-B fluids is given by Renardy [10]. The constitutive relation corresponding to the Oldroyd-B stress model, which accounts for the viscoelastic effects of a fluid, can be written as [8, 10, 17]

$$\mathbf{S} + \lambda_1 \ddot{\mathbf{S}} = 2\mu \left(\mathbf{D} + \lambda_2 \ddot{\mathbf{D}} \right). \tag{2.24}$$

In equation (2.24) we denote the relaxation and retardation times as λ_1 and λ_2, respectively, with $\lambda_1 > \lambda_2 \geq 0$, while the quantity μ is the (constant) coefficient of viscosity as in the case of Newtonian fluids. When a force is applied to a non-Newtonian fluid, such as shear stress, the fluid's microstructure undergoes a deformation. The relaxation time λ_1 is a measure of how quickly the fluid's microstructure returns to its original state (equilibrium point) when the applied force is removed. Similarly, when a force is applied to a non-Newtonian fluid, the fluid's microstructure needs time to adjust to the new state of deformation. The retardation time λ_2 is a measure of how long it takes for the fluid's microstructure to fully adjust and reach a new equilibrium state under the influence of the applied force. Values of the relaxation and retardation times which match experiments for human blood are $\lambda_1 = 0.1530$ sec and $\lambda_2 = 0.0101$ sec [11].

The upper-convected time derivatives of the extra stress tensor and deformation rate tensor that appear in equation (2.24) are, respectively,

$$\ddot{\mathbf{S}} = \frac{\partial \mathbf{S}}{\partial t} + \mathbf{u} \cdot \nabla \mathbf{S} - \left[(\nabla \mathbf{u})^T \cdot \mathbf{S} + \mathbf{S} \cdot (\nabla \mathbf{u}) \right] \tag{2.25}$$

and

$$\ddot{\mathbf{D}} = \frac{\partial \mathbf{D}}{\partial t} + \mathbf{u} \cdot \nabla \mathbf{D} - \left[(\nabla \mathbf{u})^T \cdot \mathbf{D} + \mathbf{D} \cdot (\nabla \mathbf{u}) \right]. \tag{2.26}$$

The terms in square brackets on the right-hand sides of both equations (2.25) and (2.26) were added by Oldroyd to the material derivative in order to ensure invariance of the model under a superimposed rotation [10].

2.5 A Generalized Oldroyd-B Stress Model

Since blood is known to exhibit both a dependence on local shear rates as well as viscoelastic properties, there have been efforts towards incorporating both in so-called generalized Oldroyd-B Stress models. Models were proposed by Yeleswarapu [1], Anand and Rajagopal [11], Sun and DeKee [12], Owens [13] and others. Yeleswarapu's model, which showed good agreement with experimental data is an extension of the Oldroyd-B model (2.24) where a shear rate dependence is included as follows

$$\mathbf{S} + \lambda_1 \ddot{\mathbf{S}} = 2\mu(\dot{\gamma})\mathbf{D} + 2\mu_0 \lambda_2 \ddot{\mathbf{D}}. \tag{2.27}$$

As in the Oldroyd-B model, in (2.27) we denote the relaxation and retardation times as λ_1 and λ_2, respectively, while μ_0 is the asymptotic viscosity at zero shear. The upper-convected time derivatives of the extra stress tensor and deformation rate tensor that appear in equation (2.27) are defined in (2.25) and (2.26), respectively. The viscosity function $\mu(\dot{\gamma})$ incorporates a dependence on shear rate $\dot{\gamma}$ in an identical way as outlined above for generalized Newtonian fluids. While Yeleswarapu's model as presented in [1] also included the use of the shear model (2.17), which was delveloped as part of the same work, it is also possible to use the Powell-Ering and Carreau models for $\mu(\dot{\gamma})$ in a comparative study.

In summary, the the Yeleswarapu model includes both important effects of local shear rate dependence and viscoelasticity; it has been shown to agree well with experimental data; and, it lends itself well to high-order numerical approximation. Yeleswaapu's model (2.27) will therefore form the basis of the numerical algorithms developed in this thesis. We hope to extend the numerical algorithms we develop to treat this problem to some of the adjacent models listed above in future work.

Chapter 3

Governing Equations for Blood Flow in a Pipe

Problems related to the modelling of blood flow in the cardiovascular system are accompanied by a large array of difficulties which must be overcome to completely describe the behaviour of the fluid. Among these factors are the pulsation of the flow, elastic walls, non-Newtonian fluids, vessel tapering, wave reflections, and non-circular cross-sections [18]. All of these factors interact in the determination of flow characteristics in the blood vessel system. In order to obtain quantitative results from a relatively simple model that does not require the application of high-performance computing, it is necessary to adopt an idealization of the flow. In our case, we greatly simplify the vessel geometry, representing it by a long straight rigid circular tube. While some of the complexities listed above will not be accounted for in the model, many important features specifically related to the viscous stress will indeed be retained. We believe the simplified model (and corresponding numerical results) should still remain useful in predicting important flow features.

In what follows we will derive the governing equations for fluid motion in a long straight circular tube corresponding to the Generalized Oldroyd-B model of Yeleswarapu [1] embodied in equation (2.27). Yeleswarapu did present these equations in his publication, but few details regarding the derivation were supplied. At the behest of the supervisory committee, a full derivation from first principles is included in this chapter. Since much of the derivation starting from equations (2.1), (2.2) and (2.27) relies on vector and tensor formalisms. We first define the needed vector and tensor quantities specialized to a cylindrical coordinate system. After this, the problem is reduced to the case of fully-developed flow in a circular pipe along the z-axis and governing equations from that case are presented in dimensional and non-dimensional forms.

3.1 Vector and Tensor Calculus in the Cylindrical Coordinate System

An excellent reference to review vector and tensor formalisms at an introductory level is given by Reddy [15]. The cylindrical coordinate system is defined by the coordinate transformation

$$\begin{aligned} x(r,\theta,z) &= r\cos\theta \\ y(r,\theta,z) &= r\sin\theta \\ z(r,\theta,z) &= z \end{aligned} \tag{3.1}$$

where r is the polar radius, θ is the polar angle (measured from the positive x-axis, and is taken as a positive angle in the counter-clockwise direction) and z, the elevation above the xy-plane remains unchanged. The coordinate ranges are $-\pi < \theta \leq \pi$, $0 \leq r < \infty$ and $-\infty < z < \infty$. A position vector is given by

$$\mathbf{r} = x(r,\theta,z)\hat{\mathbf{e}}_x + y(r,\theta,z)\hat{\mathbf{e}}_y + z(r,\theta,z)\hat{\mathbf{e}}_z, \tag{3.2}$$

where $\hat{\mathbf{e}}_x$, $\hat{\mathbf{e}}_y$ and $\hat{\mathbf{e}}_z$ are the standard Cartesian (unit) basis vectors.

The unit vectors corresponding to the cylindrical coordinate system are given by

$$\begin{aligned}
\hat{\mathbf{e}}_r &= \cos\theta\,\hat{\mathbf{e}}_x + \sin\theta\,\hat{\mathbf{e}}_y \\
\hat{\mathbf{e}}_\theta &= -\sin\theta\,\hat{\mathbf{e}}_x + \cos\theta\,\hat{\mathbf{e}}_y \\
\hat{\mathbf{e}}_z &= \hat{\mathbf{e}}_z
\end{aligned} \tag{3.3}$$

As is well-known, this set of vectors forms an orthonormal basis for $\mathbb{R}^3$, i.e.,

$$\hat{\mathbf{e}}_i \cdot \hat{\mathbf{e}}_j = \delta_{ij}, \tag{3.4}$$

where δ_{ij} is the Kronecker delta symbol. In equation (3.4) and below, we allow indices i and j to represent directions r, θ or z. A vector in $\mathbb{R}^3$ may thus be expressed as

$$\mathbf{u} = u_r\hat{\mathbf{e}}_r + u_\theta\hat{\mathbf{e}}_\theta + u_z\hat{\mathbf{e}}_z = u_i\hat{\mathbf{e}}_i \tag{3.5}$$

The tensor product (or dyadic product) of two vectors (or rank 1 tensors) $\mathbf{a}$ and $\mathbf{b}$ is denoted $\mathbf{a} \otimes \mathbf{b}$. This is associated with the outer product of two vectors, i.e., if $\mathbf{a}$ and $\mathbf{b}$ are column vectors of dimension 3×1 then

$$\mathbf{a} \otimes \mathbf{b} = \mathbf{a}\mathbf{b}^T = \begin{bmatrix} a_1 \\ a_2 \\ a_3 \end{bmatrix} \begin{bmatrix} b_1 & b_2 & b_3 \end{bmatrix} = \begin{bmatrix} a_1b_1 & a_1b_2 & a_1b_3 \\ a_2b_1 & a_2b_2 & a_2b_3 \\ a_3b_1 & a_3b_2 & a_3b_3 \end{bmatrix}. \tag{3.6}$$

The result of the dyadic product of two vectors is a rank 2 tensor. In the cylindrical basis, the standard unit vectors $\hat{\mathbf{e}}_r$, $\hat{\mathbf{e}}_\theta$ and $\hat{\mathbf{e}}_z$ have representations

$$\hat{\mathbf{e}}_r = \begin{bmatrix} 1 \\ 0 \\ 0 \end{bmatrix} \qquad \hat{\mathbf{e}}_\theta = \begin{bmatrix} 0 \\ 1 \\ 0 \end{bmatrix} \qquad \hat{\mathbf{e}}_z = \begin{bmatrix} 0 \\ 0 \\ 1 \end{bmatrix} \tag{3.7}$$

Tensor (dyadic) products of the standard unit vectors form standard basis dyads. For example,

$$\hat{\mathbf{e}}_r \otimes \hat{\mathbf{e}}_r = \begin{bmatrix} 1 & 0 & 0 \\ 0 & 0 & 0 \\ 0 & 0 & 0 \end{bmatrix} \qquad \text{and} \qquad \hat{\mathbf{e}}_\theta \otimes \hat{\mathbf{e}}_z = \begin{bmatrix} 0 & 0 & 0 \\ 0 & 0 & 1 \\ 0 & 0 & 0 \end{bmatrix}. \tag{3.8}$$

In general, the only non-zero element of $\hat{\mathbf{e}}_i \otimes \hat{\mathbf{e}}_j$ is the value of unity lying at the intersection of the ith row and jth column. In this way we can define several tensors of interest, such as the extra stress tensor

$$\begin{aligned} \mathbf{S} &= S_{rr}\hat{\mathbf{e}}_r \otimes \hat{\mathbf{e}}_r + S_{r\theta}\hat{\mathbf{e}}_r \otimes \hat{\mathbf{e}}_\theta + S_{rz}\hat{\mathbf{e}}_r \otimes \hat{\mathbf{e}}_z \\ &+ S_{\theta r}\hat{\mathbf{e}}_\theta \otimes \hat{\mathbf{e}}_r + S_{\theta\theta}\hat{\mathbf{e}}_\theta \otimes \hat{\mathbf{e}}_\theta + S_{\theta z}\hat{\mathbf{e}}_\theta \otimes \hat{\mathbf{e}}_z \\ &+ S_{zr}\hat{\mathbf{e}}_z \otimes \hat{\mathbf{e}}_r + S_{z\theta}\hat{\mathbf{e}}_z \otimes \hat{\mathbf{e}}_\theta + S_{zz}\hat{\mathbf{e}}_z \otimes \hat{\mathbf{e}}_z \end{aligned} \tag{3.9}$$

or the identity tensor

$$\mathbf{I} = \hat{\mathbf{e}}_r \otimes \hat{\mathbf{e}}_r + \hat{\mathbf{e}}_\theta \otimes \hat{\mathbf{e}}_\theta + \hat{\mathbf{e}}_z \otimes \hat{\mathbf{e}}_z. \tag{3.10}$$

Both of these tensors can be conveniently abbreviated as

$$\mathbf{S} = S_{ij}\hat{\mathbf{e}}_i \otimes \hat{\mathbf{e}}_j \tag{3.11}$$

and

$$\mathbf{I} = \delta_{ij}\hat{\mathbf{e}}_i \otimes \hat{\mathbf{e}}_j, \tag{3.12}$$

where, again, indices i and j represent directions r, θ or z. The transpose of a rank 2 tensor can be expressed as

$$\mathbf{S}^T = S_{ji}\hat{\mathbf{e}}_i \otimes \hat{\mathbf{e}}_j = S_{ij}\hat{\mathbf{e}}_j \otimes \hat{\mathbf{e}}_i. \tag{3.13}$$

A rank 2 tensor is symmetric if and only if $\mathbf{S}^T = \mathbf{S}$, i.e., $S_{ij} = S_{ji}$.

We can define the dot product of a vector (a rank 1 tensor) and a rank 2 tensor as

$$\mathbf{u} \cdot \mathbf{S} = (u_i \hat{\mathbf{e}}_i) \cdot (S_{jk} \hat{\mathbf{e}}_j \otimes \hat{\mathbf{e}}_k) = u_i S_{jk} (\hat{\mathbf{e}}_i \cdot \hat{\mathbf{e}}_j) \hat{\mathbf{e}}_k = u_i S_{jk} \delta_{ij} \hat{\mathbf{e}}_k = u_i S_{ik} \hat{\mathbf{e}}_k \tag{3.14}$$

This operation is known as a *simple contraction*, because the order of the tensors is contracted: i.e., to begin there was a tensor of rank 2 and a tensor of rank 1, and to end there is a tensor of rank 1. We can also define a dot product or simple contraction of two tensors of rank 2 as follows:

$$\mathbf{S} \cdot \mathbf{T} = (S_{ij} \hat{\mathbf{e}}_i \otimes \hat{\mathbf{e}}_j) \cdot (T_{k\ell} \hat{\mathbf{e}}_k \otimes \hat{\mathbf{e}}_\ell) = S_{ij} T_{k\ell} (\hat{\mathbf{e}}_j \cdot \hat{\mathbf{e}}_k) \hat{\mathbf{e}}_i \otimes \hat{\mathbf{e}}_\ell = S_{ij} T_{j\ell} \hat{\mathbf{e}}_i \otimes \hat{\mathbf{e}}_\ell \tag{3.15}$$

We note that $\mathbf{S} \cdot \mathbf{T} \neq \mathbf{T} \cdot \mathbf{S}$ since

$$\mathbf{T} \cdot \mathbf{S} = (T_{ij} \hat{\mathbf{e}}_i \otimes \hat{\mathbf{e}}_j) \cdot (S_{k\ell} \hat{\mathbf{e}}_k \otimes \hat{\mathbf{e}}_\ell) = T_{ij} S_{k\ell} (\hat{\mathbf{e}}_j \cdot \hat{\mathbf{e}}_k) \hat{\mathbf{e}}_i \otimes \hat{\mathbf{e}}_\ell = T_{ij} S_{j\ell} \hat{\mathbf{e}}_i \otimes \hat{\mathbf{e}}_\ell. \tag{3.16}$$

The symbolic vector operator ∇ is called the del operator. One can write this in cylindrical coordinates as

$$\nabla = \hat{\mathbf{e}}_r \frac{\partial}{\partial r} + \frac{1}{r} \hat{\mathbf{e}}_\theta \frac{\partial}{\partial \theta} + \hat{\mathbf{e}}_z \frac{\partial}{\partial z}. \tag{3.17}$$

Given a vector field $\mathbf{u}$ defined in (3.5), its divergence is given by the scalar obtained by applying the dot product of the del operator in equation (3.17) on the left side to $\mathbf{u}$ to obtain

$$\begin{aligned} \nabla \cdot \mathbf{u} \;&=\; \hat{\mathbf{e}}_r \cdot \left(\frac{\partial u_r}{\partial r} \hat{\mathbf{e}}_r + \frac{\partial u_\theta}{\partial r} \hat{\mathbf{e}}_\theta + \frac{\partial u_z}{\partial r} \hat{\mathbf{e}}_z \right) \\ &+\; \frac{1}{r} \hat{\mathbf{e}}_\theta \cdot \left(\frac{\partial}{\partial \theta} (u_r \hat{\mathbf{e}}_r) + \frac{\partial}{\partial \theta} (u_\theta \hat{\mathbf{e}}_\theta) + \frac{\partial u_z}{\partial \theta} \hat{\mathbf{e}}_z \right) \\ &+\; \hat{\mathbf{e}}_z \cdot \left(\frac{\partial u_r}{\partial z} \hat{\mathbf{e}}_r + \frac{\partial u_\theta}{\partial z} \hat{\mathbf{e}}_\theta + \frac{\partial u_z}{\partial z} \hat{\mathbf{e}}_z \right). \end{aligned} \tag{3.18}$$

To simplify this a little, we note the dependence of $\hat{\mathbf{e}}_r$ and $\hat{\mathbf{e}}_\theta$ on θ in equation (3.3) which leads to the important (but easilty derived) differential relations

$$\frac{\partial}{\partial\theta}\hat{\mathbf{e}}_r = \hat{\mathbf{e}}_\theta \qquad \text{and} \qquad \frac{\partial}{\partial\theta}\hat{\mathbf{e}}_\theta = -\hat{\mathbf{e}}_r. \tag{3.19}$$

Using the differential relations (3.19) and orthogonality relations (3.4) the expression for the divergence of the vector field $\mathbf{u}$ as

$$\nabla\cdot\mathbf{u} = \frac{\partial u_r}{\partial r} + \frac{1}{r}\left(\frac{\partial u_\theta}{\partial\theta} + u_r\right) + \frac{\partial u_z}{\partial z}. \tag{3.20}$$

With these details illustrated in the case of the divergence of a vector field, we can present analogous expressions for other quantities of interest in vector and tensor calculus more briefly. The gradient of a vector field $\mathbf{u}$ is given by the rank 2 tensor obtained by applying the del operator in equation (3.17) on the left side to $\mathbf{u}$ and using differential relations (3.19) to get the tensor expression

$$\begin{aligned}
\nabla\mathbf{u} &= \frac{\partial u_r}{\partial r}\hat{\mathbf{e}}_r\otimes\hat{\mathbf{e}}_r + \frac{\partial u_\theta}{\partial r}\hat{\mathbf{e}}_r\otimes\hat{\mathbf{e}}_\theta + \frac{\partial u_z}{\partial r}\hat{\mathbf{e}}_r\otimes\hat{\mathbf{e}}_z \\
&+ \frac{1}{r}\left(\frac{\partial u_r}{\partial\theta} - u_\theta\right)\hat{\mathbf{e}}_\theta\otimes\hat{\mathbf{e}}_r + \frac{1}{r}\left(\frac{\partial u_\theta}{\partial\theta} + u_r\right)\hat{\mathbf{e}}_\theta\otimes\hat{\mathbf{e}}_\theta + \frac{1}{r}\frac{\partial u_z}{\partial\theta}\hat{\mathbf{e}}_\theta\otimes\hat{\mathbf{e}}_z \\
&+ \frac{\partial u_r}{\partial z}\hat{\mathbf{e}}_z\otimes\hat{\mathbf{e}}_r + \frac{\partial u_\theta}{\partial z}\hat{\mathbf{e}}_z\otimes\hat{\mathbf{e}}_\theta + \frac{\partial u_z}{\partial z}\hat{\mathbf{e}}_z\otimes\hat{\mathbf{e}}_z.
\end{aligned} \tag{3.21}$$

The deformation rate tensor (which is clearly symmetric) is then given by

$$\begin{aligned}
\mathbf{D} &= \frac{1}{2}\left(\nabla\mathbf{u} + (\nabla\mathbf{u})^T\right) \\
&= \frac{\partial u_r}{\partial r}\hat{\mathbf{e}}_r\otimes\hat{\mathbf{e}}_r + \frac{1}{2}\left[\frac{1}{r}\left(\frac{\partial u_r}{\partial\theta} - u_\theta\right) + \frac{\partial u_\theta}{\partial r}\right]\hat{\mathbf{e}}_r\otimes\hat{\mathbf{e}}_\theta + \frac{1}{2}\left(\frac{\partial u_z}{\partial r} + \frac{\partial u_r}{\partial z}\right)\hat{\mathbf{e}}_r\otimes\hat{\mathbf{e}}_z \\
&+ \frac{1}{2}\left[\frac{1}{r}\left(\frac{\partial u_r}{\partial\theta} - u_\theta\right) + \frac{\partial u_\theta}{\partial r}\right]\hat{\mathbf{e}}_\theta\otimes\hat{\mathbf{e}}_r + \frac{1}{r}\left(\frac{\partial u_\theta}{\partial\theta} + u_r\right)\hat{\mathbf{e}}_\theta\otimes\hat{\mathbf{e}}_\theta + \frac{1}{2}\left(\frac{\partial u_\theta}{\partial z} + \frac{1}{r}\frac{\partial u_z}{\partial\theta}\right)\hat{\mathbf{e}}_\theta\otimes\hat{\mathbf{e}}_z \\
&+ \frac{1}{2}\left(\frac{\partial u_z}{\partial r} + \frac{\partial u_r}{\partial z}\right)\hat{\mathbf{e}}_z\otimes\hat{\mathbf{e}}_r + \frac{1}{2}\left(\frac{\partial u_\theta}{\partial z} + \frac{1}{r}\frac{\partial u_z}{\partial\theta}\right)\hat{\mathbf{e}}_z\otimes\hat{\mathbf{e}}_\theta + \frac{\partial u_z}{\partial z}\hat{\mathbf{e}}_z\otimes\hat{\mathbf{e}}_z.
\end{aligned} \tag{3.22}$$

Note that the trace of both the velocity gradient tensor and the deformation rate tensor is equal to the divergence of the velocity field:

$$\mathrm{Tr}(\nabla\mathbf{u}) = \mathrm{Tr}(\mathbf{D}) = \sum_{i=1}^{3}(\nabla\mathbf{u})_{ii} = \nabla\cdot\mathbf{u}. \tag{3.23}$$

The vanishing of the trace of these tensors is an easy check to verify that the mass continuity constraint for an incompressible fluid is satisfied.

Next, applying the dot product of $\mathbf{u} = (u_r, u_\theta, u_z)$ to the left side of the tensor in equation (3.21) using the rule (3.14) for vector-tensor dot products yields the important vector quantity

$$\begin{aligned}\mathbf{u}\cdot\nabla\mathbf{u} = & \left[u_r\frac{\partial u_r}{\partial r} + \frac{u_\theta}{r}\left(\frac{\partial u_r}{\partial\theta} - u_\theta\right) + u_z\frac{\partial u_r}{\partial z}\right]\hat{\mathbf{e}}_r + \left[u_r\frac{\partial u_\theta}{\partial r} + \frac{u_\theta}{r}\left(\frac{\partial u_\theta}{\partial\theta} + u_r\right) + u_z\frac{\partial u_\theta}{\partial z}\right]\hat{\mathbf{e}}_\theta \\ + & \left[u_r\frac{\partial u_z}{\partial r} + \frac{u_\theta}{r}\frac{\partial u_z}{\partial\theta} + u_z\frac{\partial u_z}{\partial z}\right]\hat{\mathbf{e}}_z.\end{aligned} \tag{3.24}$$

These are the inertial terms in the equations of motion (2.1). Also needed by those equations is the divergence of the stress tensor. The divergence of the extra stress tensor (or any generic rank 2 tensor for that matter) computed by applying the del operator (3.17) to the left side of the tensor (3.9) and effectively using the vector-tensor dot product rule (3.14) together with differential relations (3.19) to obtain the expression

$$\begin{aligned}\nabla\cdot\mathbf{S} = & \left[\frac{\partial S_{rr}}{\partial r} + \frac{1}{r}\left(\frac{\partial S_{\theta r}}{\partial\theta} + S_{rr} - S_{\theta\theta}\right) + \frac{\partial S_{zr}}{\partial z}\right]\hat{\mathbf{e}}_r \\ & + \left[\frac{\partial S_{r\theta}}{\partial r} + \frac{1}{r}\left(\frac{\partial S_{\theta\theta}}{\partial\theta} + S_{r\theta} + S_{\theta r}\right) + \frac{\partial S_{z\theta}}{\partial z}\right]\hat{\mathbf{e}}_\theta \\ & + \left[\frac{\partial S_{rz}}{\partial r} + \frac{1}{r}\left(\frac{\partial S_{\theta z}}{\partial\theta} + S_{rz}\right) + \frac{\partial S_{zz}}{\partial z}\right]\hat{\mathbf{e}}_z.\end{aligned} \tag{3.25}$$

Finally, in computing the upper-convected time derivatives of the extra stress tensor and deformation rate tensor which appear in the constitutive relation (2.27) we require an expression for the gradient of a tensor. Indeed, applying the del operator (3.17) to the left side of the tensor (3.9) and using differential relations (3.19) results in the rank 3 tensor expression for the gradient of $\mathbf{S}$ given by

$$
\begin{aligned}
\nabla \mathbf{S} = & \frac{\partial S_{rr}}{\partial r} \hat{\mathbf{e}}_r \otimes \hat{\mathbf{e}}_r \otimes \hat{\mathbf{e}}_r + \frac{\partial S_{r\theta}}{\partial r} \hat{\mathbf{e}}_r \otimes \hat{\mathbf{e}}_r \otimes \hat{\mathbf{e}}_\theta + \frac{\partial S_{rz}}{\partial r} \hat{\mathbf{e}}_r \otimes \hat{\mathbf{e}}_r \otimes \hat{\mathbf{e}}_z \\
& + \frac{\partial S_{\theta r}}{\partial r} \hat{\mathbf{e}}_r \otimes \hat{\mathbf{e}}_\theta \otimes \hat{\mathbf{e}}_r + \frac{\partial S_{\theta\theta}}{\partial r} \hat{\mathbf{e}}_r \otimes \hat{\mathbf{e}}_\theta \otimes \hat{\mathbf{e}}_\theta + \frac{\partial S_{\theta z}}{\partial r} \hat{\mathbf{e}}_r \otimes \hat{\mathbf{e}}_\theta \otimes \hat{\mathbf{e}}_z \\
& + \frac{\partial S_{zr}}{\partial r} \hat{\mathbf{e}}_r \otimes \hat{\mathbf{e}}_z \otimes \hat{\mathbf{e}}_r + \frac{\partial S_{z\theta}}{\partial r} \hat{\mathbf{e}}_r \otimes \hat{\mathbf{e}}_z \otimes \hat{\mathbf{e}}_\theta + \frac{\partial S_{zz}}{\partial r} \hat{\mathbf{e}}_r \otimes \hat{\mathbf{e}}_z \otimes \hat{\mathbf{e}}_z \\
& + \frac{1}{r} \left(\frac{\partial S_{rr}}{\partial \theta} - S_{r\theta} - S_{\theta r} \right) \hat{\mathbf{e}}_\theta \otimes \hat{\mathbf{e}}_r \otimes \hat{\mathbf{e}}_r + \frac{1}{r} \left(\frac{\partial S_{r\theta}}{\partial \theta} + S_{rr} - S_{\theta\theta} \right) \hat{\mathbf{e}}_\theta \otimes \hat{\mathbf{e}}_r \otimes \hat{\mathbf{e}}_\theta \\
& + \frac{1}{r} \left(\frac{\partial S_{rz}}{\partial \theta} - S_{\theta z} \right) \hat{\mathbf{e}}_\theta \otimes \hat{\mathbf{e}}_r \otimes \hat{\mathbf{e}}_z + \frac{1}{r} \left(\frac{\partial S_{\theta r}}{\partial \theta} + S_{rr} - S_{\theta\theta} \right) \hat{\mathbf{e}}_\theta \otimes \hat{\mathbf{e}}_\theta \otimes \hat{\mathbf{e}}_r \\
& + \frac{1}{r} \left(\frac{\partial S_{\theta\theta}}{\partial \theta} + S_{\theta r} + S_{r\theta} \right) \hat{\mathbf{e}}_\theta \otimes \hat{\mathbf{e}}_\theta \otimes \hat{\mathbf{e}}_\theta + \frac{1}{r} \left(\frac{\partial S_{\theta z}}{\partial \theta} + S_{rz} \right) \hat{\mathbf{e}}_\theta \otimes \hat{\mathbf{e}}_\theta \otimes \hat{\mathbf{e}}_z \\
& + \frac{1}{r} \left(\frac{\partial S_{zr}}{\partial \theta} - S_{z\theta} \right) \hat{\mathbf{e}}_\theta \otimes \hat{\mathbf{e}}_z \otimes \hat{\mathbf{e}}_r + \frac{1}{r} \left(\frac{\partial S_{z\theta}}{\partial \theta} + S_{zr} \right) \hat{\mathbf{e}}_\theta \otimes \hat{\mathbf{e}}_z \otimes \hat{\mathbf{e}}_\theta \\
& + \frac{1}{r} \frac{\partial S_{zz}}{\partial \theta} \hat{\mathbf{e}}_\theta \otimes \hat{\mathbf{e}}_z \otimes \hat{\mathbf{e}}_z \\
& + \frac{\partial S_{rr}}{\partial z} \hat{\mathbf{e}}_z \otimes \hat{\mathbf{e}}_r \otimes \hat{\mathbf{e}}_r + \frac{\partial S_{r\theta}}{\partial z} \hat{\mathbf{e}}_z \otimes \hat{\mathbf{e}}_r \otimes \hat{\mathbf{e}}_\theta + \frac{\partial S_{rz}}{\partial z} \hat{\mathbf{e}}_z \otimes \hat{\mathbf{e}}_r \otimes \hat{\mathbf{e}}_z \\
& + \frac{\partial S_{\theta r}}{\partial z} \hat{\mathbf{e}}_z \otimes \hat{\mathbf{e}}_\theta \otimes \hat{\mathbf{e}}_r + \frac{\partial S_{\theta\theta}}{\partial z} \hat{\mathbf{e}}_z \otimes \hat{\mathbf{e}}_\theta \otimes \hat{\mathbf{e}}_\theta + \frac{\partial S_{\theta z}}{\partial z} \hat{\mathbf{e}}_z \otimes \hat{\mathbf{e}}_\theta \otimes \hat{\mathbf{e}}_z \\
& + \frac{\partial S_{zr}}{\partial z} \hat{\mathbf{e}}_z \otimes \hat{\mathbf{e}}_z \otimes \hat{\mathbf{e}}_r + \frac{\partial S_{z\theta}}{\partial z} \hat{\mathbf{e}}_z \otimes \hat{\mathbf{e}}_z \otimes \hat{\mathbf{e}}_\theta + \frac{\partial S_{zz}}{\partial z} \hat{\mathbf{e}}_z \otimes \hat{\mathbf{e}}_z \otimes \hat{\mathbf{e}}_z .
\end{aligned}
\tag{3.26}
$$

The needed quantity $\mathbf{u} \cdot \nabla \mathbf{S}$ is the rank 2 tensor that results from the simple contraction by applying the the dot product of $\mathbf{u}$ to the leftmost vector in each triplet $\hat{\mathbf{e}}_i \otimes \hat{\mathbf{e}}_j \otimes \hat{\mathbf{e}}_k$ and using orthogonality relations (3.4). This can be expressed as

$$
\mathbf{u} \cdot \nabla \mathbf{S} = u_r \mathbf{V}_1 + u_\theta \mathbf{V}_2 + u_z \mathbf{V}_3 \tag{3.27}
$$

where

$$
\begin{aligned}
\mathbf{V}_1 = \frac{\partial \mathbf{S}}{\partial r} = & \frac{\partial S_{rr}}{\partial r}\hat{\mathbf{e}}_r \otimes \hat{\mathbf{e}}_r + \frac{\partial S_{r\theta}}{\partial r}\hat{\mathbf{e}}_r \otimes \hat{\mathbf{e}}_\theta + \frac{\partial S_{rz}}{\partial r}\hat{\mathbf{e}}_r \otimes \hat{\mathbf{e}}_z \\
& + \frac{\partial S_{\theta r}}{\partial r}\hat{\mathbf{e}}_\theta \otimes \hat{\mathbf{e}}_r + \frac{\partial S_{\theta\theta}}{\partial r}\hat{\mathbf{e}}_\theta \otimes \hat{\mathbf{e}}_\theta + \frac{\partial S_{\theta z}}{\partial r}\hat{\mathbf{e}}_\theta \otimes \hat{\mathbf{e}}_z \\
& + \frac{\partial S_{zr}}{\partial r}\hat{\mathbf{e}}_z \otimes \hat{\mathbf{e}}_r + \frac{\partial S_{z\theta}}{\partial r}\hat{\mathbf{e}}_z \otimes \hat{\mathbf{e}}_\theta + \frac{\partial S_{zz}}{\partial r}\hat{\mathbf{e}}_z \otimes \hat{\mathbf{e}}_z,
\end{aligned}
\tag{3.28}
$$

$$
\begin{aligned}
\mathbf{V}_2 \;\; = & \frac{1}{r}\left(\frac{\partial S_{rr}}{\partial \theta} - S_{r\theta} - S_{\theta r}\right)\hat{\mathbf{e}}_r \otimes \hat{\mathbf{e}}_r + \frac{1}{r}\left(\frac{\partial S_{r\theta}}{\partial \theta} + S_{rr} - S_{\theta\theta}\right)\hat{\mathbf{e}}_r \otimes \hat{\mathbf{e}}_\theta \\
+ & \frac{1}{r}\left(\frac{\partial S_{rz}}{\partial \theta} - S_{\theta z}\right)\hat{\mathbf{e}}_r \otimes \hat{\mathbf{e}}_z + \frac{1}{r}\left(\frac{\partial S_{\theta r}}{\partial \theta} + S_{rr} - S_{\theta\theta}\right)\hat{\mathbf{e}}_\theta \otimes \hat{\mathbf{e}}_r \\
+ & \frac{1}{r}\left(\frac{\partial S_{\theta\theta}}{\partial \theta} + S_{\theta r} + S_{r\theta}\right)\hat{\mathbf{e}}_\theta \otimes \hat{\mathbf{e}}_\theta + \frac{1}{r}\left(\frac{\partial S_{\theta z}}{\partial \theta} + S_{rz}\right)\hat{\mathbf{e}}_\theta \otimes \hat{\mathbf{e}}_z \\
+ & \frac{1}{r}\left(\frac{\partial S_{zr}}{\partial \theta} - S_{z\theta}\right)\hat{\mathbf{e}}_z \otimes \hat{\mathbf{e}}_r + \frac{1}{r}\left(\frac{\partial S_{z\theta}}{\partial \theta} + S_{zr}\right)\hat{\mathbf{e}}_z \otimes \hat{\mathbf{e}}_\theta \\
+ & \frac{1}{r}\frac{\partial S_{zz}}{\partial \theta}\hat{\mathbf{e}}_z \otimes \hat{\mathbf{e}}_z,
\end{aligned}
\tag{3.29}
$$

and

$$
\begin{aligned}
\mathbf{V}_3 = \frac{\partial \mathbf{S}}{\partial z} = & \frac{\partial S_{rr}}{\partial z}\hat{\mathbf{e}}_r \otimes \hat{\mathbf{e}}_r + \frac{\partial S_{r\theta}}{\partial z}\hat{\mathbf{e}}_r \otimes \hat{\mathbf{e}}_\theta + \frac{\partial S_{rz}}{\partial z}\hat{\mathbf{e}}_r \otimes \hat{\mathbf{e}}_z \\
& + \frac{\partial S_{\theta r}}{\partial z}\hat{\mathbf{e}}_\theta \otimes \hat{\mathbf{e}}_r + \frac{\partial S_{\theta\theta}}{\partial z}\hat{\mathbf{e}}_\theta \otimes \hat{\mathbf{e}}_\theta + \frac{\partial S_{\theta z}}{\partial z}\hat{\mathbf{e}}_\theta \otimes \hat{\mathbf{e}}_z \\
& + \frac{\partial S_{zr}}{\partial z}\hat{\mathbf{e}}_z \otimes \hat{\mathbf{e}}_r + \frac{\partial S_{z\theta}}{\partial z}\hat{\mathbf{e}}_z \otimes \hat{\mathbf{e}}_\theta + \frac{\partial S_{zz}}{\partial z}\hat{\mathbf{e}}_z \otimes \hat{\mathbf{e}}_z.
\end{aligned}
\tag{3.30}
$$

3.2 Fully Developed Flow in a Circular Tube

In what follows, we specialize the general equations developed in the previous section to the case of a fully developed flow of a viscous fluid in a circular tube of radius R and of infinite length, with the center line of the tube lying on the z-axis. In the fully developed regime, the pressure gradient acts only in the axial direction and the transverse velocity components are identically zero [19]. In this greatly simplified situation, the flow does not depend on any particular location along the axis of the pipe; the only non-zero velocity component acts in the z-direction and depends only on time and the transverse coordinates. Furthermore, in our particular case, since the tube cross section possesses circular symmetry, the axial velocity is assumed independent of the angular coordinate θ. We therefore assume a velocity profile of the form

$$\mathbf{u}(r, \theta, z, t) = u_z(r, t)\hat{\mathbf{e}}_z. \tag{3.31}$$

This velocity field must obey no-slip boundary conditions on the wall of the tube $r = R$, i.e., $u_z(R, t) = 0$ for all $t > 0$.

In the case of fully developed flow with velocity field defined by (3.31), the velocity gradient tensor in equation (3.21) and the deformation rate tensor in equation (3.22) become, respectively,

$$\nabla\mathbf{u} = \frac{\partial u_z}{\partial r}\hat{\mathbf{e}}_r \otimes \hat{\mathbf{e}}_z \tag{3.32}$$

and

$$\mathbf{D} = \frac{1}{2}\left(\nabla\mathbf{u} + (\nabla\mathbf{u})^T\right) = \frac{1}{2}\frac{\partial u_z}{\partial r}\left(\hat{\mathbf{e}}_r \otimes \hat{\mathbf{e}}_z + \hat{\mathbf{e}}_z \otimes \hat{\mathbf{e}}_r\right). \tag{3.33}$$

It is not difficult to see that the trace of both the velocity gradient tensor and the deformation rate tensor vanishes, and hence by equation (3.23), the mass continuity constraint (2.2) is always satisfied by the velocity profile (3.31).

In what immediately follows, we will evaluate the terms on the right-hand side of the constitutive relation (2.27), which will suggest an appropriate form to assume for the extra stress tensor $\mathbf{S}$ to be used on the left-hand side of (2.27). Using the rule (3.15) for a simple contraction of two tensors, it's not hard to show that

$$\mathbf{D}^2 = \mathbf{D}\cdot\mathbf{D} = \frac{1}{4}\left(\frac{\partial u_z}{\partial r}\right)^2\left(\hat{\mathbf{e}}_r \otimes \hat{\mathbf{e}}_r + \hat{\mathbf{e}}_z \otimes \hat{\mathbf{e}}_z\right). \tag{3.34}$$

Using equation (3.34) it is now straightforward to show the the shear rate, given by equation

(2.9), simplifies to the following expression in fully developed flow:

$$\dot{\gamma} = \sqrt{2\mathrm{Tr}(\mathbf{D}^2)} = \left| \frac{\partial u_z}{\partial r} \right| \tag{3.35}$$

Next, using the expression (3.26) for the gradient of a tensor, in fully developed flow, the gradient of the deformation rate tensor simplifies to

$$\nabla \mathbf{D} = \frac{1}{2} \frac{\partial^2 u_z}{\partial r^2} \left(\hat{\mathbf{e}}_r \otimes \hat{\mathbf{e}}_r \otimes \hat{\mathbf{e}}_z + \hat{\mathbf{e}}_r \otimes \hat{\mathbf{e}}_z \otimes \hat{\mathbf{e}}_r \right) \tag{3.36}$$

Taking the dot product of (3.36) on the left with the velocity field $\mathbf{u}$ it is easy to see that in the fully-developed case that $\mathbf{u} \cdot \nabla \mathbf{D} = \mathbf{0}$. Next, using the rule (3.15) for a simple contraction of two tensors, we find the simplified expressions applicable to fully developed flow

$$(\nabla \mathbf{u})^T \cdot \mathbf{D} = \mathbf{D} \cdot (\nabla \mathbf{u}) = \frac{1}{2} \left(\frac{\partial u_z}{\partial r} \right)^2 \hat{\mathbf{e}}_z \otimes \hat{\mathbf{e}}_z. \tag{3.37}$$

Using the brief calculations outlined immediately above, we can see that the upper-convected time derivative of deformations rate tensor (2.26) in the fully developed case becomes

$$\ddot{\mathbf{D}} = \frac{1}{2} \frac{\partial^2 u_z}{\partial t \partial r} \left(\hat{\mathbf{e}}_r \otimes \hat{\mathbf{e}}_z + \hat{\mathbf{e}}_z \otimes \hat{\mathbf{e}}_r \right) - \left(\frac{\partial u_z}{\partial r} \right)^2 \hat{\mathbf{e}}_z \otimes \hat{\mathbf{e}}_z. \tag{3.38}$$

While this quantity will shortly play an important role in determining our equations of motion, at this point we simply note that both $\mathbf{D}$ and $\ddot{\mathbf{D}}$ are symmetric rank 2 tensors. This implies that both the right and left hand sides of the generalized Oldroyd-B stress equation (2.27) are symmetric rank 2 tensors; in particular $\mathbf{S}$ and $\ddot{\mathbf{S}}$ must both be symmetric. Furthermore, in the case of fully developed flow, it can be seen that the only non-zero tensor components on the right-hand side of the constitutive relation (2.27) are the rz, zr and zz components, and that these depend only on variables r and t. This implies that, on the left-hand side of (2.27) we must have stress components as follows:

$$S_{rr} = 0 \qquad S_{\theta\theta} = 0 \qquad S_{r\theta} = S_{\theta r} = 0 \qquad S_{z\theta} = S_{\theta z} = 0 \qquad S_{rz} = S_{zr}. \tag{3.39}$$

Overall, based on the analysis above, we conclude that the appropriate assumed form of the extra stress tensor in fully developed flow is

$$\mathbf{S}(r,\theta,z,t) = S_{rz}(r,t)\hat{\mathbf{e}}_r \otimes \hat{\mathbf{e}}_z + S_{rz}(r,t)\hat{\mathbf{e}}_z \otimes \hat{\mathbf{e}}_r + S_{zz}(r,t)\hat{\mathbf{e}}_z \otimes \hat{\mathbf{e}}_z. \tag{3.40}$$

Next, using the expression (3.26) for the gradient of a tensor, in fully developed flow, the gradient of the extra stress tensor (3.40) simplifies to

$$\begin{aligned} \nabla\mathbf{S} &= \frac{\partial S_{rz}}{\partial r}\hat{\mathbf{e}}_r \otimes \hat{\mathbf{e}}_r \otimes \hat{\mathbf{e}}_z + \frac{\partial S_{rz}}{\partial r}\hat{\mathbf{e}}_r \otimes \hat{\mathbf{e}}_z \otimes \hat{\mathbf{e}}_r + \frac{\partial S_{zz}}{\partial r}\hat{\mathbf{e}}_r \otimes \hat{\mathbf{e}}_z \otimes \hat{\mathbf{e}}_z \\ &+ \frac{S_{rz}}{r}\hat{\mathbf{e}}_\theta \otimes \hat{\mathbf{e}}_\theta \otimes \hat{\mathbf{e}}_z + \frac{S_{rz}}{r}\hat{\mathbf{e}}_\theta \otimes \hat{\mathbf{e}}_z \otimes \hat{\mathbf{e}}_\theta \end{aligned} \tag{3.41}$$

Taking the dot product of (3.41) on the left with the velocity field $\mathbf{u}$ it is easy to see that in the fully-developed case that $\mathbf{u} \cdot \nabla\mathbf{S} = \mathbf{0}$. Next, using the rule (3.15) for a simple contraction of two tensors, we find using (3.32) the simplified expressions applicable to fully developed flow:

$$(\nabla\mathbf{u})^T \cdot \mathbf{S} = \mathbf{S} \cdot (\nabla\mathbf{u}) = S_{rz}\frac{\partial u_z}{\partial r}\hat{\mathbf{e}}_z \otimes \hat{\mathbf{e}}_z. \tag{3.42}$$

Using the brief calculations outlined immediately above, we can see that the upper-convected time derivative of the extra stress tensor (2.25) in the fully developed case becomes

$$\ddot{\mathbf{S}} = \frac{\partial S_{rz}}{\partial t}\left(\hat{\mathbf{e}}_r \otimes \hat{\mathbf{e}}_z + \hat{\mathbf{e}}_z \otimes \hat{\mathbf{e}}_r\right) + \left(\frac{\partial S_{zz}}{\partial t} - 2S_{rz}\frac{\partial u_z}{\partial r}\right)\hat{\mathbf{e}}_z \otimes \hat{\mathbf{e}}_z. \tag{3.43}$$

Substituting the expressions (3.33), (3.38), (3.40) and (3.43) into the constitutive relation (2.27) results in three equations corresponding to the rz, zr and zz tensor components. Unsurprisingly, due to the symmetry of the tensors, the rz and zr components yield the same equation, which reads

$$S_{rz} + \lambda_1\frac{\partial S_{rz}}{\partial t} = \mu(\dot{\gamma})\frac{\partial u_z}{\partial r} + \mu_0\lambda_2\frac{\partial^2 u_z}{\partial t\partial r}. \tag{3.44}$$

The zz component of the tensor equation, on the other hand, yields

$$S_{zz} + \lambda_1 \left(\frac{\partial S_{zz}}{\partial t} - 2\frac{\partial u_z}{\partial r} S_{rz} \right) = -2\mu_0 \lambda_2 \left(\frac{\partial u_z}{\partial r} \right)^2 . \tag{3.45}$$

Equations (3.44) and (3.45) are two of our governing equations of motion. In order to derive a third equation, we substitute (3.31) and (3.40) into (2.4) and (2.1). Using tensor formulas in equations (3.24) and (3.25) we thus obtain the vector equation

$$\frac{1}{\rho}\frac{\partial p}{\partial r}\hat{\mathbf{e}}_r + \frac{1}{r\rho}\frac{\partial p}{\partial \theta}\hat{\mathbf{e}}_\theta + \left[\frac{\partial u_z}{\partial t} + \frac{1}{\rho}\frac{\partial p}{\partial z} - \frac{1}{\rho}\left(\frac{\partial S_{rz}}{\partial r} + \frac{S_{rz}}{r} \right) \right] \hat{\mathbf{e}}_z = \mathbf{0}. \tag{3.46}$$

The equations resulting from the r and θ components imply that the pressure gradient is not a function of r or θ. Since u_z and S_{rz} depend only on r and t, this implies that $\partial p/(\partial z)$ must only be a function of time, and this becomes a prescribed input to the problem. The z component of (3.46) gives

$$\frac{\partial u_z}{\partial t} = -\frac{1}{\rho}\frac{\partial p}{\partial z} + \frac{1}{\rho}\left(\frac{\partial S_{rz}}{\partial r} + \frac{S_{rz}}{r} \right). \tag{3.47}$$

Equation (3.47) represents the last needed governing equation of motion. Taken together with equations (3.44) and (3.45), we now have a system of three coupled partial differential equations for the three unknowns u_z, S_{rz} and S_{zz}. The required boundary conditions remain the no-slip boundary conditions on the wall of the tube $r = R$, i.e., $u_z(R, t) = 0$ for all $t > 0$. We will also impose conditions that the velocity and stress fields remain finite.

An additional quantity of interest in fluid mechanics, and rheology in particular, is the volumetric flow rate $Q = Q(t)$, which measures the volume of fluid passing through a surface $\partial\Omega$ of a region Ω per unit time. Generally the volumetric flow rate is defined as the surface integral

$$Q(t) = \iint_{\partial\Omega} \mathbf{n} \cdot \mathbf{u} \, dS, \tag{3.48}$$

where $\mathbf{n}$ is an outward unit normal vector to $\partial\Omega$ with surface element dS. Specialized to the case of fully developed pipe flow where the integral is taken over the circular cross section we have $\mathbf{n} = \hat{\mathbf{e}}_z$ and

$$Q(t) = \int_{-\pi}^{\pi}\int_{0}^{R} u_z(r,t) r dr d\theta = 2\pi \int_{0}^{R} u_z(r,t) r dr. \tag{3.49}$$

In what follows, we will scale the equations presented in this section in order to obtain non-dimensional expressions useful in describing a wide variety of physical configurations.

3.3 Non-Dimensional Equations

In order to arrive at a set of non-dimensional equations, we must select a length and a time scale (or alternatively a length and velocity scale). The majority of this thesis deals with oscillating flows in circular tubes driven by a prescribed pressure gradient $\partial p/(\partial z)$ which oscillates with fundamental frequency ω. It is therefore natural to scale the problem using the tube radius R and the frequency of oscillation ω of the pressure gradient. We introduce non-dimensional variables (indicated by a '$*$') as follows:

$$\begin{gathered} r^* = \frac{r}{R}, \quad t^* = \omega t, \quad \lambda_1^* = \omega\lambda_1, \quad \lambda_2^* = \omega\lambda_2, \quad \gamma^* = \frac{\gamma}{\omega}, \quad \Lambda^* = \omega\Lambda, \\ u_z^* = \frac{u_z}{\omega R}, \quad S_{rz}^* = \frac{S_{rz}}{\rho(\omega R)^2}, \quad S_{zz}^* = \frac{S_{zz}}{\rho(\omega R)^2}, \quad p^* = \frac{p}{\rho(\omega R)^2}, \quad Q^* = \frac{Q}{\omega R^3}. \end{gathered} \tag{3.50}$$

Dropping the '$*$' notation from each variable, the non-dimensional field equations are expressed as

$$\frac{\partial u_z}{\partial t} = -f(t) + \frac{\partial S_{rz}}{\partial r} + \frac{S_{rz}}{r} \tag{3.51}$$

$$S_{rz} + \lambda_1 \frac{\partial S_{rz}}{\partial t} = \frac{1-\beta}{\mathrm{Wo}} F(\dot{\gamma}) \frac{\partial u_z}{\partial r} + \frac{\beta}{\mathrm{Wo}} \frac{\partial u_z}{\partial r} + \frac{\lambda_2}{\mathrm{Wo}} \frac{\partial^2 u_z}{\partial t \partial r} \tag{3.52}$$

$$S_{zz} + \lambda_1 \left(\frac{\partial S_{zz}}{\partial t} - 2\frac{\partial u_z}{\partial r} S_{rz} \right) = -\frac{2\lambda_2}{\mathrm{Wo}} \left(\frac{\partial u_z}{\partial r} \right)^2. \tag{3.53}$$

The non-dimensional Womersley number, which is assumed to be an $\mathcal{O}(1)$ constant, is given by

$$\mathrm{Wo} = \frac{\rho \omega R^2}{\mu_0}. \tag{3.54}$$

The Womersley number can be viewed in much the same way as a Reynolds number applied to oscillatory flows. Indeed, if one were to assume that a characteristic velocity for the flow is the angular velocity $v = \omega R$ then the Womersley number becomes

$$\mathrm{Wo} = \frac{\rho v R}{\mu_0}, \tag{3.55}$$

which is the usual definition of the Reynolds number for flow in a pipe of radius R. Appropriate boundary conditions for the non-dimensional equations are no-slip boundary conditions on the wall of the tube $r = 1$, i.e., $u_z(1, t) = 0$ for all $t > 0$. We will also impose conditions that the flow quantities remain finite. Note that in equation (3.51) we have introduced the convenient notation for the non-dimensional pressure gradient (a function of time alone)

$$f(t) = \frac{\partial p}{\partial z}, \tag{3.56}$$

which drives the flow and will be a prescribed input to the problem. In equation (3.52) we have used the non-dimensional viscosity function $F(\dot{\gamma})$ defined as per equation (2.12). With the argument of the function understood to be the non-dimensional shear rate, in the definitions of the functions used in this work given by (2.14), (2.17) and (2.20) one should therefore take the quantity Λ to be the non-dimensional version $\Lambda^* = \omega\Lambda$. We have also introduced the viscosity ratio

$$\beta = \mu_\infty / \mu_0 \tag{3.57}$$

Finally, the non-dimensional volumetric flow rate may be computed from the integral expression

$$Q(t) = 2\pi \int_0^1 u_z(r, t) r dr. \tag{3.58}$$

As part of this work, we will produce numerical solutions of the non-dimensional equations (3.51), (3.52) and (3.53) for different values of the non-dimensional parameters β, Wo, λ_1, λ_2 and Λ. In particular, a meaningful set of parameters in line with what one would expect to use in bloodflow applications can be obtained as follows. We will assume a pulsation frequency of

2 Hz or equivalently $\omega = 4\pi$ rad/sec and a vessel diameter of 2 mm or equivalently a radius $R = 10^{-3}$ m. Using a blood density $\rho = 1054$ kg/m^3 and asymptotic viscosity values as per equation (2.11) given by $\mu_0 = 0.056$ Pa $\cdot$ s and $\mu_\infty = 0.00345$ Pa $\cdot$ s we obtain

$$\mathrm{Wo} = 0.2365 \qquad \text{and} \qquad \beta = 0.0616. \tag{3.59}$$

Further, assuming dimensional values $\lambda_1 = 0.1530$ sec, $\lambda_2 = 0.0101$ sec and $\Lambda = 11.14$ sec, we obtain the needed non-dimensional versions for use in our code as follows:

$$\lambda_1^* = 1.923, \qquad \lambda_2^* = 0.127, \quad \text{and} \quad \Lambda^* = 140. \tag{3.60}$$

Given the low value of the Womersley number, we can see that this set of physical parameters corresponds to a creeping flow.

Chapter 4

Exact Solutions in the Case of Constant Viscosity

In this thesis chapter we will produce analytical solutions of the problem in the case of constant viscosity, when $\mu_\infty = \mu_0$ and hence $\beta = 1$ corresponding to the standard Oldroyd-B stress model (2.24). The same results can be achieved with $\beta = 1/2$ and $F = 1$, but this later case represents a better test of our code as it uses all subroutines, in particular those needed for the (usually nonlinear) viscosity function calculation. The non-dimensional governing equations (3.51), (3.52) and (3.53) reduce to

$$\frac{\partial u_z}{\partial t} = -f(t) + \frac{\partial S_{rz}}{\partial r} + \frac{S_{rz}}{r} \tag{4.1}$$

$$S_{rz} + \lambda_1 \frac{\partial S_{rz}}{\partial t} = \frac{1}{\mathrm{Wo}} \frac{\partial u_z}{\partial r} + \frac{\lambda_2}{\mathrm{Wo}} \frac{\partial^2 u_z}{\partial t \partial r} \tag{4.2}$$

$$S_{zz} + \lambda_1 \left(\frac{\partial S_{zz}}{\partial t} - 2 \frac{\partial u_z}{\partial r} S_{rz} \right) = -\frac{2\lambda_2}{\mathrm{Wo}} \left(\frac{\partial u_z}{\partial r} \right)^2 . \tag{4.3}$$

We haven't seen the solutions produced in this chapter elsewhere in the literature, but solutions to closely related problems can be found in [20], for example, and our solution methodology mirrors widely used techniques [18].

4.1 Steady Flow

Prior to addressing the problem of oscillating flow in a circular tubes, it is instructive to first examine the case when the axial pressure gradient is constant. The purpose of this section is to establish some basic features of flow in tubes of circular cross-section which will later serve as useful benchmarks for comparison when examining the properties of oscillating flows.

In the case of steady flow, the velocity and stress fields are functions only of the spatial variables and are independent of time. Indeed, the flow is driven by the constant pressure gradient

$$f(t) = k. \tag{4.4}$$

Since the velocity field does not depend on time, equation (4.1) then simplifies to

$$\frac{dS_{rz}}{dr} + \frac{S_{rz}}{r} = k. \tag{4.5}$$

This non-homogeneous ordinary differential equation is straightforward to solve since the corresponding homogeneous problem is separable and it's easy to deduce that a particular solution must have the form Cr, where C is a constant. In this way we can show that the solution of the problem is

$$S_{rz}(r) = \frac{kr}{2} + \frac{\alpha}{r}, \tag{4.6}$$

where α is an arbitrary constant. Enforcing conditions that the stress (and hence veclocity) remain finite in the domain, we set $\alpha = 0$ and thus obtain the linear rz stress profile

$$S_{rz}(r) = \frac{kr}{2}. \tag{4.7}$$

Next, substituting the result (4.7) into equation (4.2) and setting all time derivatives to zero results in the ordinary differential equation

$$\frac{du_z}{dr} = \mathrm{Wo}\, S_{rz} = \mathrm{Wo}\frac{kr}{2} \tag{4.8}$$

Integrating both sides of this last equation yields

$$u_z(r) = \mathrm{Wo}\frac{kr^2}{4} + \alpha, \tag{4.9}$$

where α is another arbitrary constant (separate from any value used in computing an expression for the stress S_{rz} above). Enforcing no slip conditions $u_z(\pm 1) = 0$ leads us to select $\alpha = -\mathrm{Wo}k/4$ and hence we obtain the steady flow velocity profile corresponding to Poiseuille flow

$$u_z(r) = \mathrm{Wo}\frac{k}{4}\left(r^2 - 1\right). \tag{4.10}$$

A few comments about the steady velocity profile (4.10) are in order. The expression for the velocity depends on the Womersley number, Wo, which itself depends on a frequency of oscillation ω, and yet the underlying flow is steady. This represents something of a problem in imposing a physical interpretation on the expression (4.10). While we did not commit any mathematical errors, a more sensible (and indeed traditional) approach would have been to rescale the problem using a length scale R and characteristic velocity scale v from which a time scale R/v could be obtained. Doing precisely this would have resulted in the appearance of the Reynolds number $\mathrm{Re} = \rho v R/\mu_0$ in place of the Womersley number in (4.10). Still, the expression (4.10) will be useful in validating (in the sub case of steady flow) our numerical solver which has the Womersley number hard-coded.

Continuing with our analyis of steady flow, setting time derivatives to zero in equation (4.3) yields

$$S_{zz} = 2\lambda_1 \frac{du_z}{dr} S_{rz} - \frac{2\lambda_2}{\mathrm{Wo}} \left(\frac{du_z}{dr}\right)^2. \tag{4.11}$$

Substituting expressions (4.7) and (4.8) into this last equation results in the quadratic zz stress profile

$$S_{zz}(r) = \frac{\mathrm{Wo}}{2}(kr)^2(\lambda_1 - \lambda_2). \tag{4.12}$$

Finally, substituting the velocity profile (4.10) into the expression (3.58) yields the steady non-dimensional flow rate

$$Q = -\frac{\pi k \mathrm{Wo}}{8}. \tag{4.13}$$

4.2 Oscillating Flow

The problem of fully developed oscillating flow in tubes of circular cross-section is now addressed. From the governing equations presented in the previous chapter, we will derive analytical expressions for the velocity, stress fields and volumetric flow rate in the steady state. Similar expressions can be found in the literature [18]. In the case of oscillating flow, the velocity and stress fields are functions of both radial position and time, and the flow is driven by a time-harmonic pressure gradient of the form

$$f(t) = k\cos(t) \qquad \text{or} \qquad f(t) = k\sin(t). \tag{4.14}$$

The mathematical analysis is greatly simplified if instead of considering these two cases separately, we consider their complex combination

$$f(t) = k\mathrm{e}^{it}. \tag{4.15}$$

Owing to the linearity of the governing equations solutions for the velocity u_z and stress S_{rz} can then be obtained assuming the same complex time dependence, with real and imaginary parts extracted corresponding to a cosine and sine input pressure gradient respectively. As detailed below, we will have to be a little more careful handling the stress S_{zz} due to the presence of a nonlinear term in its governing equation.

As detailed above, we will assume a complex time dependence for the velocity u_z and stress S_{rz} as follows:

$$u_z(r,t) = w(r)\mathrm{e}^{it} \tag{4.16}$$

$$S_{rz}(r,t) = s_{rz}(r)\mathrm{e}^{it} \tag{4.17}$$

Substituting these assumed forms into the governing equations (4.1) and (4.2) yield the ordinary differential equations

$$iw(r) = -k + s'_{rz}(r) + \frac{s_{rz}(r)}{r} \tag{4.18}$$

and

$$(1 + i\lambda_1)s_{rz}(r) = \frac{1}{\mathrm{Wo}}(1 + i\lambda_2)w'(r), \tag{4.19}$$

respectively, where the prime indicates a total derivative. Equation (4.19) immediately simplifies to

$$s_{rz}(r) = \frac{1}{\psi}w'(r), \tag{4.20}$$

where we denote the complex constant

$$\psi = \frac{(1 + i\lambda_1)\mathrm{Wo}}{1 + i\lambda_2}. \tag{4.21}$$

Substituting (4.20) into the differential equation (4.18) then yields the second order problem

$$w''(r) + \frac{1}{r}w'(r) - i\psi w(r) = k\psi. \tag{4.22}$$

As can be verified, equation (4.22) is an inhomogeneous Bessel equation which has general solution

$$w(r) = ik + \alpha_1 J_0\left(\sqrt{-i\psi}r\right) + \alpha_2 Y_0\left(\sqrt{-i\psi}r\right). \tag{4.23}$$

Here we denote $J_0(x)$ and $Y_0(x)$ as the Bessel functions of the first and second kinds, respectively, of order 0 [21] [22]. The quantities α_1 and α_2 are arbitrary constants. As is well-known, when $x \to 0$ we have [21, eqn.9.1.8]

$$Y_0(x) \sim \frac{2}{\pi}\ln(x), \tag{4.24}$$

revealing that the Bessel Function of the second kind possesses a logarithmic singularity at $x = 0$. In order to ensure the flow quantities remain finite in the domain, we therefore set $\alpha_2 = 0$. Next, enforcing no slip conditions $w(1) = 0$ immediately leads us to select the constant

$$\alpha_1 = \frac{-ik}{J_0\left(\sqrt{-i\psi}\right)}. \tag{4.25}$$

We therefore obtain the complex velocity profile

$$w(r) = ik\left[1 - \frac{J_0\left(\sqrt{-i\psi}r\right)}{J_0\left(\sqrt{-i\psi}\right)}\right]. \tag{4.26}$$

The time-dependent complex velocity is then simply obtained from equation (4.26) as

$$u_z(r,t) = ik\left[1 - \frac{J_0\left(\sqrt{-i\psi}r\right)}{J_0\left(\sqrt{-i\psi}\right)}\right]\mathrm{e}^{it}. \tag{4.27}$$

It is now straightforward to find an expression for the rz stress. Since $J_0'(x) = -J_1(x)$ [21, eqn.9.1.28] we have

$$w'(r) = \frac{ik\sqrt{-i\psi}J_1\left(\sqrt{-i\psi}r\right)}{J_0\left(\sqrt{-i\psi}\right)}, \tag{4.28}$$

and hence

$$s_{rz}(r) = \frac{ik\sqrt{-i\psi}J_1\left(\sqrt{-i\psi}r\right)}{\psi J_0\left(\sqrt{-i\psi}\right)}. \tag{4.29}$$

The time-dependent complex rz stress is then simply obtained from equation (4.17) as

$$S_{rz}(r,t) = \frac{ik\sqrt{-i\psi}J_1\left(\sqrt{-i\psi}r\right)}{\psi J_0\left(\sqrt{-i\psi}\right)}\mathrm{e}^{it}. \tag{4.30}$$

Finally, to find an expression for the zz stress, we have to be a little more careful due the presence of nonlinear terms in the governing equation (4.3). In this case, we must include both real and imaginary parts of expressions in our analysis. We first seek an expression for the zz stress corresponding to the real part of the complex pressure gradient (4.15), i.e.,

$$f(t) = \frac{1}{2}\left(k\mathrm{e}^{it} + k\mathrm{e}^{-it}\right) = k\cos(t) \tag{4.31}$$

In this case, we use the real parts of the velocity and stress expressions derived above; in particular,

$$\frac{\partial u_z}{\partial r} = \frac{1}{2}\left(w'(r)\mathrm{e}^{it} + \bar{w}'(r)\mathrm{e}^{-it}\right) \tag{4.32}$$

and

$$S_{rz} = \frac{1}{2}\left(s'(r)\mathrm{e}^{it} + \bar{s}'(r)\mathrm{e}^{-it}\right). \tag{4.33}$$

With these last two expressions, the nonlinear terms in equation (4.3) become, with the help of equation (4.20),

$$\begin{aligned} &2\lambda_1 \frac{\partial u_z}{\partial r} S_{rz} - \frac{2\lambda_2}{\mathrm{Wo}}\left(\frac{\partial u_z}{\partial r}\right)^2 \\ = &\frac{(\lambda_1 - \lambda_2)}{\mathrm{Wo}}\left[\frac{|w'|^2}{(1+\lambda_1^2)} + \frac{(w')^2}{2(1+i\lambda_1)}\mathrm{e}^{2it} + \frac{(\bar{w}')^2}{2(1-i\lambda_1)}\mathrm{e}^{-2it}\right]. \end{aligned} \tag{4.34}$$

This leads us to assume the form for the zz stress as follows:

$$S_{zz}(r,t) = s_{zz}^{(0)}(r) + s_{zz}^{(2)}(r)\mathrm{e}^{2it} + \bar{s}_{zz}^{(2)}(r)\mathrm{e}^{-2it}. \tag{4.35}$$

Substituting this form of solution into equation (4.3) then leads us to the expressions corresponding to the real part of the complex pressure gradient (4.15):

$$s_{zz}^{(0)}(r) = \frac{(\lambda_1 - \lambda_2)|w'|^2}{\mathrm{Wo}(1+\lambda_1^2)} \tag{4.36}$$

and

$$s_{zz}^{(2)}(r) = \frac{(\lambda_1 - \lambda_2)(w')^2}{2\mathrm{Wo}(1+i\lambda_1)(1+2i\lambda_1)}. \tag{4.37}$$

Proceeding in a nearly identical manner as above, we seek an expression for the zz stress corresponding to the imaginary part of the complex pressure gradient (4.15), i.e.,

$$f(t) = \frac{1}{2i}\left(k\mathrm{e}^{it} - k\mathrm{e}^{-it}\right) = k\sin(t). \tag{4.38}$$

In this case, we use the imaginary parts of the velocity and stress expressions derived above.

In particular,

$$\frac{\partial u_z}{\partial r} = \frac{1}{2i}\left(w'(r)\mathrm{e}^{it} - \bar{w}'(r)\mathrm{e}^{-it}\right) \tag{4.39}$$

and

$$S_{rz} = \frac{1}{2i}\left(s'(r)\mathrm{e}^{it} - \bar{s}'(r)\mathrm{e}^{-it}\right). \tag{4.40}$$

With these last two expressions, the nonlinear terms in equation (4.3) become, with the help of equation (4.20),

$$\begin{aligned} & 2\lambda_1 \frac{\partial u_z}{\partial r} S_{rz} - \frac{2\lambda_2}{\mathrm{Wo}}\left(\frac{\partial u_z}{\partial r}\right)^2 \\ = \quad & \frac{(\lambda_1 - \lambda_2)}{\mathrm{Wo}}\left[\frac{|w'|^2}{(1+\lambda_1^2)} - \frac{(w')^2}{2(1+i\lambda_1)}\mathrm{e}^{2it} - \frac{(\bar{w}')^2}{2(1-i\lambda_1)}\mathrm{e}^{-2it}\right]. \end{aligned} \tag{4.41}$$

This results in us assuming the same form of S_{zz} stress in (4.35), for which we find component functions as follows:

$$s_{zz}^{(0)}(r) = \frac{(\lambda_1 - \lambda_2)|w'|^2}{\mathrm{Wo}(1+\lambda_1^2)} \tag{4.42}$$

and

$$s_{zz}^{(2)}(r) = -\frac{(\lambda_1 - \lambda_2)(w')^2}{2\mathrm{Wo}(1+i\lambda_1)(1+2i\lambda_1)}. \tag{4.43}$$

The last quantity of interest for which we need an expression is the volumetric flow rate. To find this, it's a simple matter of using the expression for the time-dependent complex velocity in (4.27) together with the expression for the flow rate (3.58). The resulting integral is not difficult to evaluate with the help of the Bessel function identity [22]

$$\frac{d}{dx}(x^n J_n(x)) = x^n J_{n-1}(x). \tag{4.44}$$

With some elementary manipulations, it's not difficult to find the expression for the complex volumetric flow rate as follows:

$$Q(t) = i\pi k\left[1 - \frac{2J_1\left(\sqrt{-i\psi}\right)}{\sqrt{-i\psi}\,J_0\left(\sqrt{-i\psi}\right)}\right]\mathrm{e}^{it}. \tag{4.45}$$

In summary, we have found useful analytical solutions to the problem when the pressure gradient is a constant and when it is a simple harmonic function of time. In the later case, it can be seen that the velocity $u_z(r,t)$ and shear stress $S_{rz}(r,t)$ are 2π-periodic functions, while the normal stress $S_{zz}(r,t)$ is a π-periodic function. Using a simple Matlab implementation (in which we always take the principal square root of $\sqrt{-i\psi}$ to evaluate complex expressions), we generate plots of the velocity and stress profiles for the linear case $\beta = 1$. Plots for differing values of the code parameters Wo, λ_1, λ_2 over one period in time P are shown in Figure 4.1, Figure 4.2, Figure 4.3 and Figure 4.4.

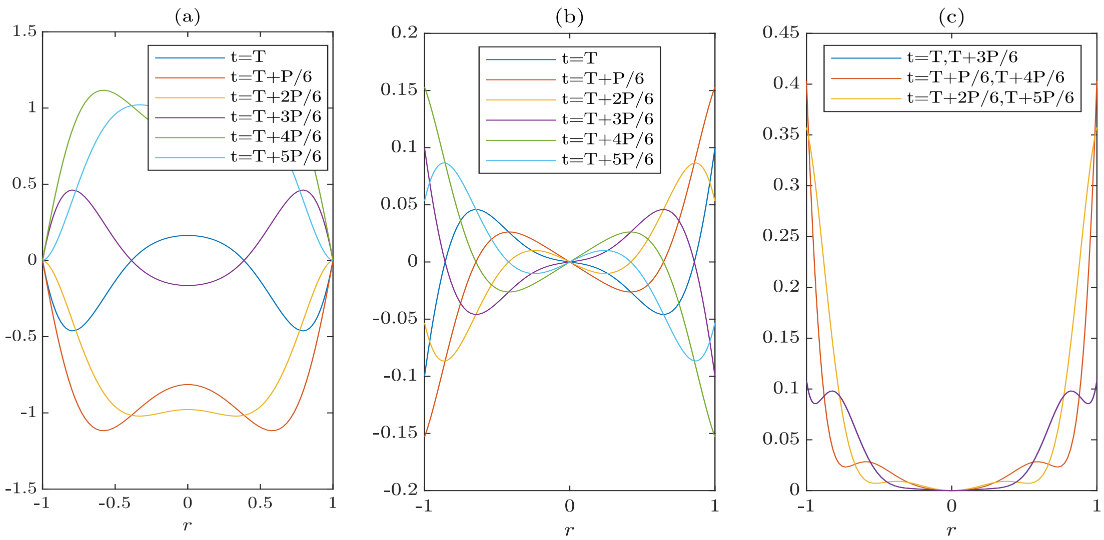

Figure 4.1: Exact solutions for linear case $\beta = 1$ with parameters $\lambda_1 = 1$, $\lambda_2 = 1/2$, $\beta = 1$, Wo $= 30$ and $f(t) = \cos(t)$. The velocity profile $u_z(r,t)$ and stress profiles $S_{rz}(r,t)$ and $S_{zz}(r,t)$ are plotted in figures (a), (b) and (c), respectively, at different times over one period starting at $t = T = 0$ using $M = 90$ points.

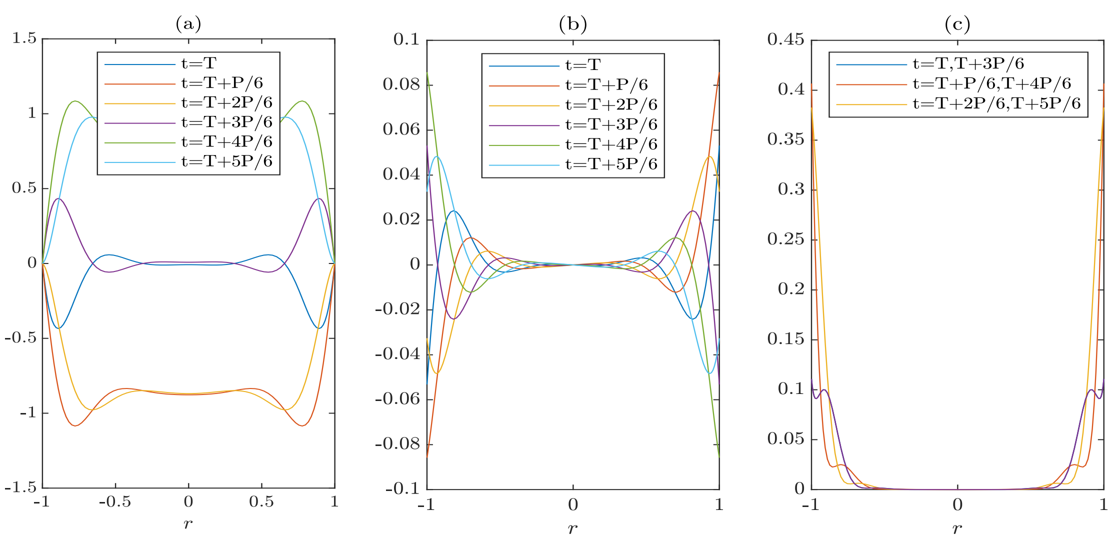

Figure 4.2: Exact solutions for linear case $\beta = 1$ with parameters $\lambda_1 = 1$, $\lambda_2 = 1/2$, $\beta = 1$, Wo $= 100$ and $f(t) = \cos(t)$. The velocity profile $u_z(r,t)$ and stress profiles $S_{rz}(r,t)$ and $S_{zz}(r,t)$ are plotted in figures (a), (b) and (c), respectively, at different times over one period starting at $t = T = 0$ using $M = 90$ points.

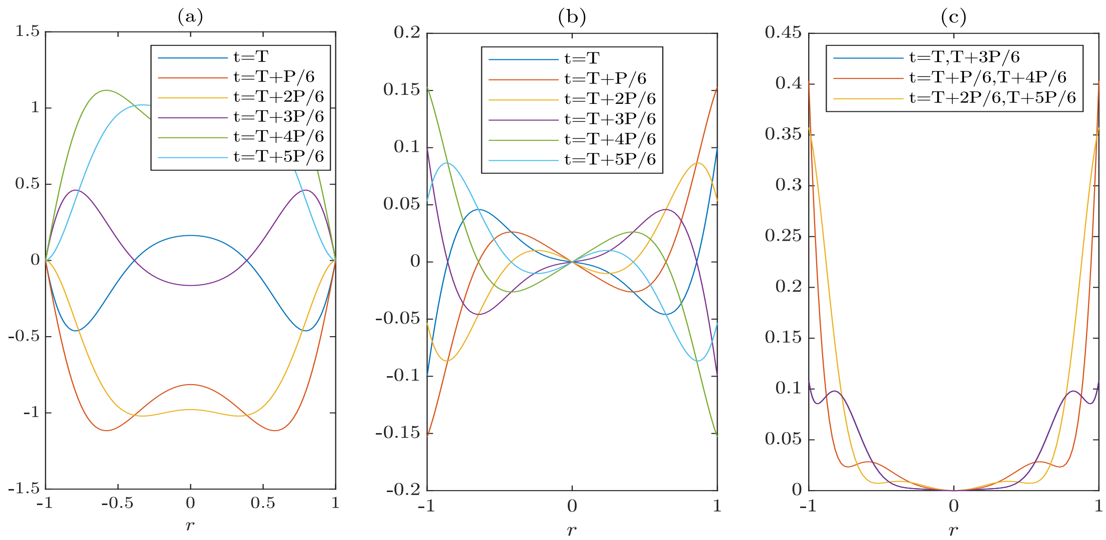

Figure 4.3: Exact solutions for linear case $\beta = 1$ with parameters $\lambda_1 = 3/4$, $\lambda_2 = 2/5$, $\beta = 1$, Wo $= 30$ and $f(t) = \cos(t)$. The velocity profile $u_z(r,t)$ and stress profiles $S_{rz}(r,t)$ and $S_{zz}(r,t)$ are plotted in figures (a), (b) and (c), respectively, at different times over one period starting at $t = T = 0$ using $M = 90$ points.

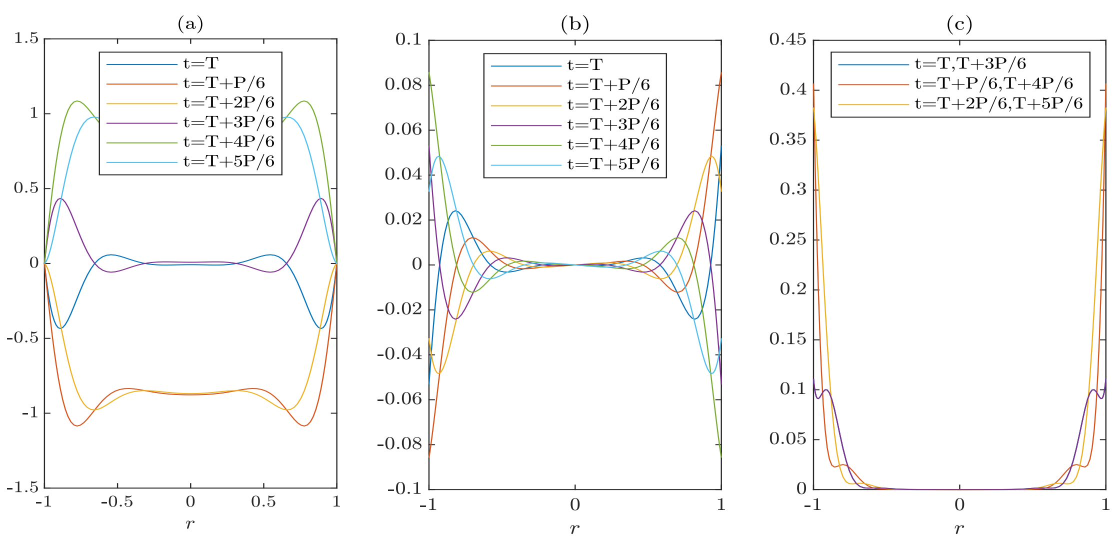

Figure 4.4: Exact solutions for linear case $\beta = 1$ with parameters $\lambda_1 = 3/4$, $\lambda_2 = 2/5$, $\beta = 1$, Wo $= 100$ and $f(t) = \cos(t)$. The velocity profile $u_z(r,t)$ and stress profiles $S_{rz}(r,t)$ and $S_{zz}(r,t)$ are plotted in figures (a), (b) and (c), respectively, at different times over one period starting at $t = T = 0$ using $M = 90$ points.

Chapter 5

Chebyshev Approximation

5.1 Basic Properties of Chebyshev Polynomials

The Chebyshev polynomial of the first kind, $T_n(x)$, is a polynomial of degree n defined by the relation

$$T_n(x) = \cos(n\theta) \qquad \text{when} \qquad x = \cos\theta. \tag{5.1}$$

The range of variable x is the interval $[-1, 1]$ which allows one to take the range of the corresponding variable θ to be the interval $[0, \pi]$, resulting in a one-to-one mapping. It is readily seen from the trigonometric forms that the Chebyshev polynomials must obey the stable recurrence

$$T_{n+1}(x) = 2xT_n(x) - T_{n-1}(x) \tag{5.2}$$

with starting values $T_0(x) = 1$ and $T_1(x) = x$. As is well-known [23, 24] for $n > 0$ the Chebyshev polynomials have the explicit expansion

$$T_n(x) = \sum_{k=0}^{[n/2]} \frac{(-1)^k}{2^{2k-n+1}} \frac{n}{n-k} \binom{n-k}{k} x^{n-2k} \tag{5.3}$$

with $T_0(x) = 1$.

The Chebyshev polynomial $T_n(x)$ has precisely n zeros and $n+1$ extrema in the interval

$x \in [-1, 1]$. Since $T_n(\cos\theta) = \cos(n\theta)$, the zeros must correspond to the n zeros in θ of $\cos(n\theta)$ for $\theta \in [0, \pi]$ which occur when

$$n\theta = \left(k - \frac{1}{2}\right)\pi \qquad k = 1, 2, \ldots, n. \tag{5.4}$$

The zeros of $T_n(x)$ must therefore be

$$x = x_k = \cos\left[\left(k - \frac{1}{2}\right)\frac{\pi}{n}\right] \qquad k = 1, 2, \ldots, n. \tag{5.5}$$

Similarly, the $n+1$ extrema of $T_n(x)$ must correspond to the $n+1$ extrema of $\cos(n\theta)$ for $\theta \in [0, \pi]$ which occur when

$$n\theta = k\pi \qquad k = 0, 1, \ldots, n. \tag{5.6}$$

Hence the extrema of $T_n(x)$ occur when

$$x = x_k = \cos\left(\frac{k\pi}{n}\right) \qquad k = 0, 1, \ldots, n. \tag{5.7}$$

All of the maxima satisfy $T_n(x_k) = 1$ and all of the minima satisfy $T_n(x_k) = -1$.

Generally speaking, Chebyshev methods applied to the solution of partial differential equations (such as those that we develop in this work) involve the testing or evaluation of quantities at the zeros (5.5) or extrema (5.7), each resulting in a slightly different, but rapidly converging algorithm.

5.2 Orthogonality and Series Expansions

As is well-known, the first-kind Chebyshev polynomials are mutually orthogonal on the interval $[-1, 1]$ with respect to the weight function $1/\sqrt{1-x^2}$. Specifically they have orthogonality relation

$$\int_{-1}^{1} \frac{T_n(x)T_m(x)}{\sqrt{1-x^2}}dx = \int_0^{\pi} \cos(n\theta)\cos(m\theta)d\theta = \begin{cases} \pi & n = m = 0 \\ \pi/2 & n = m > 0 \\ 0 & \text{otherwise} \end{cases} . \tag{5.8}$$

The orthogonality relations (5.8) allow us to expand (nonsingular) functions defined on the interval $x \in [-1, 1]$ in a series of Chebyshev polynomials. Indeed, the Chebyshev series expansion of a function $f(x)$ is given by

$$f(x) = \sum_{n=1}^{\infty}{}' a_n T_{n-1}(x) = \sum_{n=1}^{\infty} a_n T_{n-1}(x) - \frac{a_1}{2}, \tag{5.9}$$

where, as indicated in the right sum, the prime in the left sum indicates that the coefficient associated with $T_0(x) = 1$ is to be halved. Owing to the orthogonality relations (5.8), the coefficients a_n are related to the original function $f(x)$ via the Chebyshev transform

$$a_n = \frac{2}{\pi}\int_{-1}^{1} \frac{T_{n-1}(x)f(x)}{\sqrt{1-x^2}}dx \qquad n = 1, 2, \ldots . \tag{5.10}$$

Indeed, equations (5.9) and (5.10) constitute the Chebyshev transform pair of the function $f(x)$. As is well-known, with the change of variables $x = \cos\theta$ we have $T_n(\cos\theta) = \cos(n\theta)$ and the Chebyshev expansion (5.9) becomes a cosine series (of an even periodic function) in the θ-variable, while the Chebyshev transform in (5.10) becomes a cosine transform of that function in the θ-variable. This observation is important, since it explains how the Chebyshev expansions inherit several properties of Fourier expansions, in particular, the super-algebraic convergence rate of the series when the function $f(x)$ is infinitely differentiable.

In the development of numerical schemes for the solution of practical problems on bounded domains, the set of Chebyshev polynomials $T_n(x)$ is a natural choice of basis functions to represent an unknown function to be determined. Of course, a truncation of the expansion

(5.9) is required:

$$f(x) \approx \sum_{i=1}^{N}{}' a_i T_{i-1}(x) = \sum_{i=1}^{N} a_i T_{i-1}(x) - \frac{a_1}{2} \tag{5.11}$$

Given the relationship of the Chebyshev series of a function $f(x)$ in the x-variable to the cosine series of the even periodic function $f(\cos\theta)$ in the θ-variable, it follows that the series coefficients (5.10) may be produced (where necessary) in $\mathcal{O}(N \log N)$ operations by means of a fast cosine transform [25] (also see discussion below). The use of such an expansion is highly advantageous: in the case of an infinitely differentiable function $f \in C^\infty[-1,1]$, the Chebyshev series (5.11) thus converges faster than $\mathcal{O}(N^{-m})$ for any positive integer m—i.e. it achieves super-algebraic convergence.

Numerical schemes which involve Chebyshev approximation typically rely on discrete samplings of a function $f_k = f(x_k)$ at a set of nodes x_k for $k = 1, 2, \ldots, N$. The specific choice of sampling points x_k is an important consideration in determining which fast transform algorithm should be applied to the problem (there are different algorithms available to compute a fast cosine transform, known as the DCT-I, DCT-II, DCT-III, etc, applicable to specific point samplings). To elaborate further on this, suppose x_k are the N zeros of $T_N(x)$ given by equation (5.5). A well-known discrete orthogonality relation involving these points is [25, eqn 5.8.6]

$$\sum_{k=1}^{N} T_i(x_k) T_j(x_k) = \begin{cases} 0 & i \neq j \\ N/2 & 0 < i = j < N \\ N & i = j = 0 \end{cases} . \tag{5.12}$$

for $i, j < N$. Assuming an equality in the relation (5.11), an assumption justified by the typically rapid convergence of such expansions, and testing the function $f(x)$ at the zeros x_k for $k = 1, 2, \ldots, N$ in (5.5) gives

$$f_k = f(x_k) = \sum_{i=1}^{N}{}' a_i T_{i-1}(x_k) \tag{5.13}$$

Multiplying each side of equation (5.13) by $T_{j-1}(x_k)$ and summing over indices $k = 1, 2, \ldots, N$

we obtain

$$\sum_{k=1}^{N} f(x_k)T_{j-1}(x_k) = \sum_{i=1}^{N}{}' a_i \left(\sum_{k=1}^{N} T_{i-1}(x_k)T_{j-1}(x_k) \right) \tag{5.14}$$

for $j = 1, 2, \ldots, N$. Applying the discrete orthogonality relation (5.12) to equation (5.14) then immediately gives the formula for the coefficients

$$a_i = \frac{2}{N} \sum_{k=1}^{N} f(x_k)T_{i-1}(x_k), \qquad i = 1, 2, \ldots, N. \tag{5.15}$$

Using the identity

$$T_{i-1}(x_k) = \cos\left[\left(k - \frac{1}{2}\right)\frac{(i-1)\pi}{N}\right] \tag{5.16}$$

in equations (5.13) and (5.15) then finally results in the standard formulas

$$a_k = \frac{2}{N} \sum_{i=1}^{N} f(x_i)\cos\left[\left(i - \frac{1}{2}\right)\frac{(k-1)\pi}{N}\right], \qquad k = 1, 2, \ldots, N. \tag{5.17}$$

and

$$f_k = f(x_k) = \frac{a_1}{2} + \sum_{i=2}^{N} a_i \cos\left[\left(k - \frac{1}{2}\right)\frac{(i-1)\pi}{N}\right] \qquad k = 1, 2, \ldots, N. \tag{5.18}$$

Note that we swapped indices $i \leftrightarrow k$ in obtaining the expression (5.17) . Equations (5.17) and (5.18) constitute the important cosine transform pair known as the (normalized) DCT-II and DCT-III, respectively. While both the definitions (5.17) and (5.18) show precisely what is computed by the DCT-II and the DCT-III respectively, we generally do not directly adapt the summations in these formulas as an $\mathcal{O}(N^2)$ algorithm. Instead both of these quantities are computed using fast $\mathcal{O}(N \log N)$ algorithms; see for example details on the fast Fourier transform in [25]. In particular, in this work, we use numerical routines from the FFTW3 [26] package that have been developed by experts and substantially tested. Available numerical routines for fast DCT-II and DCT-III algorithms typically produce un-normalized quantities; the normalized transforms can subsequently be obtained by applying multiplicative factors. In detail, suppose the discrete function values and spectral amplitudes are stored in N-element arrays as

$$\mathbf{f} = \{f(x_k)\}_{k=1}^{N} \qquad \text{and} \qquad \mathbf{a} = \{a_k\}_{k=1}^{N}. \tag{5.19}$$

These array quantities are related through the N-point un-normalied DCT-II and DCT-III as

$$\mathbf{a} = \frac{1}{N}\text{DCTII}(\mathbf{f}) \qquad \text{and} \qquad \mathbf{f} = \frac{1}{2}\text{DCTIII}(\mathbf{a}). \tag{5.20}$$

The normalization of the transforms is accomplished by applying multiplicative factors $1/N$ or $1/2$, which are included above. To coincide precisely with definitions in the FFTW3 package, we define the kth element of the un-normalized DCT-II as

$$\text{DCTII}(\mathbf{f})_k = 2\sum_{i=1}^{N} f(x_i)\cos\left[\left(i - \frac{1}{2}\right)\frac{(k-1)\pi}{N}\right], \qquad k = 1, 2, \ldots, N. \tag{5.21}$$

Similarly, we define the kth element of the un-normalized DCT-II as

$$\text{DCTIII}(\mathbf{a})_k = a_1 + 2\sum_{i=2}^{N} a_i \cos\left[\left(k - \frac{1}{2}\right)\frac{(i-1)\pi}{N}\right] \qquad k = 1, 2, \ldots, N. \tag{5.22}$$

In closing for this section, we mention briefly that the DCT-II and DCT-III are not the only possibilities for handling data represented as a Chebyshev series. Indeed, it is also possible to sample the data at the extrema (5.7). In this case a modification of the discrete orthogonality relation (5.12) is required to deduce an expression for the Chebyshev series coefficients, and gives rise to the well-known DCT-I discrete cosine transform.

5.3 Indefinite and definite integrals

A major benefit of considering the Chebyshev representation of a function is that basic operations on that data such as integration and differentiation can done very quickly and accurately in the transformed space. We will illustrate this in what follows, presenting formulas needed later to develop our numerical algorithms.

We first consider indefinite integrals of the Chebyshev polynomials. Using the usual substitution $x = \cos\theta$ and the identity $T_n(\cos\theta) = \cos(n\theta)$ we have

$$\int T_n(x)dx = -\int \cos(n\theta)\sin\theta d\theta = -\frac{1}{2}\int \left[\sin(n+1)\theta - \sin(n-1)\theta\right] d\theta \tag{5.23}$$

Evaluation of the right-hand integral leads directly to

$$\int T_0(x)dx = \cos\theta = T_1(x), \qquad \int T_1(x)dx = \frac{1}{4}\cos(2\theta) = \frac{1}{4}T_2(x) \tag{5.24}$$

and

$$\int T_n(x)dx = \frac{1}{2}\left[\frac{\cos(n+1)\theta}{n+1} - \frac{\cos(n-1)\theta}{n-1}\right] = \frac{1}{2}\left[\frac{T_{n+1}(x)}{n+1} - \frac{T_{n-1}(x)}{n-1}\right]; \quad n > 1. \tag{5.25}$$

It is now a straightforward matter to produce an anti-derivative of a function defined in terms of a Chebyshev series. If $f(x)$ is defined as the truncated expansion (5.11) then the anti-derivative is

$$\int f(x)dx = \text{const} + \frac{1}{2}a_1T_1(x) + \frac{1}{4}a_2T_2(x) + \sum_{n=3}^{N}\frac{a_n}{2}\left[\frac{T_n(x)}{n} - \frac{T_{n-2}(x)}{n-2}\right]. \tag{5.26}$$

The expression (5.26) is valid for all $N > 0$ provided we adopt the usual convention that the sum vanish when the upper index is smaller than the lower index. This is easily rearranged into the truncated Chebyshev series

$$\int f(x)dx = {\sum_{n=1}^{N+1}}' A_nT_{n-1}(x) \tag{5.27}$$

with $A_1 = 2 * \text{const}$ determined in terms of the constant of integration and

$$A_n = \frac{a_{n-1} - a_{n+1}}{2(n-1)}, \quad n > 1. \tag{5.28}$$

Unsurprisingly, the algorithm for the anti-derivative of a polynomial of degree N results in a polynomial of degree $N+1$. In a practical implementation we would set $a_{N+1} = a_{N+2} = 0$ in

(5.28) (an assumption justfied in view of the rapid convergence of such expansions) since we only know the original N-member set $a_1, a_2, \ldots, a_N$, giving rise to the expressions

$$A_N = \frac{a_{N-1}}{2(N-1)} \qquad \text{and} \qquad A_{N+1} = \frac{a_N}{2N}. \tag{5.29}$$

An expression for the definite integral of a Chebyshev expansion of the form (5.11) over the intverval $x \in [-1, 1]$ (a quantity of frequent interest) can easily be derived. Indeed, applying limits of integration to (5.24) and (5.25) and using the well-known identities [23]

$$T_n(1) = 1 \qquad \text{and} \qquad T_n(-1) = (-1)^n, \qquad n \geq 0. \tag{5.30}$$

we obtain

$$\int_{-1}^{1} T_0(x)dx = 2, \qquad \int_{-1}^{1} T_1(x)dx = 0 \tag{5.31}$$

and

$$\int_{-1}^{1} T_n(x)dx = \frac{1}{2}\left[\frac{1}{n+1} - \frac{1}{n-1}\right][1-(-1)^n]; \quad n > 1. \tag{5.32}$$

These last few results may be neatly summarized as

$$\int_{-1}^{1} T_{2n+1}(x)dx = 0 \quad \text{and} \quad \int_{-1}^{1} T_{2n}(x)dx = \frac{2}{1-4n^2}, \quad n \geq 0. \tag{5.33}$$

Integrating the expansion (5.11) over the interval $x \in [-1, 1]$ on a term-by-term basis and retaining only the non-zero terms then yields the expression

$$\int_{-1}^{1} f(x)dx = {\sum_{n=1}^{N}}' a_n \int_{-1}^{1} T_{n-1}(x)dx = \frac{a_1}{2}\int_{-1}^{1} T_0(x)dx + 2\sum_{n=2}^{[M/2]} a_{2n-1}\int_{-1}^{1} T_{2n-2}(x)dx, \tag{5.34}$$

where $[M/2]$ denotes the floor of $M/2$, i.e., the greatest integer not exceeding this quantity. Including the explicit expressions in (5.33) finally produces the desired quadrature formula

$$\int_{-1}^{1} f(x)dx = a_1 + 2\sum_{n=2}^{[M/2]} \frac{a_{2n-1}}{1-(2n-2)^2} = a_1 - 2\sum_{n=2}^{[M/2]} \frac{a_{2n-1}}{(2n-1)(2n-3)}. \tag{5.35}$$

Equation (5.35) is the celebrated Clenshaw-Curtis quadrature formula [25, eqn. 5.9.3].

Next we derive an expression for the definite integral of a Chebyshev expansion of the form (5.11) over the interval $x \in [0,1]$; An integral of data over this interval is required in order to compute volumetric flow rates. In order to derive a quadrature formula for this case, it simplifies matters to separate outthe contributions from even and odd Chebyshev polynomials in our formula for the anti-derivative (5.26). We obtain

$$\begin{aligned}\int f(x)dx &= \text{const} + \frac{1}{2}a_1T_1(x) + \frac{1}{4}a_2T_2(x) + \sum_{n=1}^{\left[\frac{N-1}{2}\right]} \frac{a_{2n+1}}{2}\left[\frac{T_{2n+1}(x)}{2n+1} - \frac{T_{2n-1}(x)}{2n-1}\right] \\ &+ \sum_{n=1}^{\left[\frac{N-2}{2}\right]} \frac{a_{2n+2}}{2}\left[\frac{T_{2n+2}(x)}{2n+2} - \frac{T_{2n}(x)}{2n}\right]. \qquad (5.36)\end{aligned}$$

Applying the upper limit $x = 1$ to the formula (5.26) with $T_n(1) = 1$ and applying the lower limit to (5.36) with

$$T_{2n}(0) = (-1)^n \qquad \text{and} \qquad T_{2n+1}(0) = 0, \qquad n \geq 0, \qquad (5.37)$$

we obtain the needed quadrature formula as the difference of the upper and lower limits to be

$$\int_0^1 f(x)dx = \frac{1}{2}a_1 + \frac{3}{4}a_2 - \sum_{n=3}^{N} \frac{a_n}{n(n-2)} + \frac{1}{4}\sum_{n=1}^{\left[\frac{N-2}{2}\right]} \frac{(-1)^n(2n+1)a_{2n+2}}{n(n+1)}. \qquad (5.38)$$

In pretty much an identical way as we did for the sums in (5.36), for the middle sum in equation (5.38), we can separate contributions from the even and odd polynomials by writing

$$\sum_{n=3}^{N} \frac{a_n}{n(n-2)} = \sum_{n=1}^{\left[\frac{N-1}{2}\right]} \frac{a_{2n+1}}{(2n+1)(2n-1)} + \frac{1}{4}\sum_{n=1}^{\left[\frac{N-2}{2}\right]} \frac{a_{2n+2}}{n(n+1)}. \qquad (5.39)$$

Substituting (5.39) in (5.38) then leads directly to the final form of our numerical quadrature formula:

$$\int_0^1 f(x)dx = \frac{1}{2}a_1 + \frac{3}{4}a_2 - \sum_{n=1}^{\left[\frac{N-1}{2}\right]} \frac{a_{2n+1}}{(2n+1)(2n-1)} - \frac{1}{4}\sum_{n=1}^{\left[\frac{N-2}{2}\right]} \frac{1-(-1)^n(2n+1)}{n(n+1)}a_{2n+2}. \quad (5.40)$$

5.4 Computing derivatives of data

We now turn our attention to the important task of evaluating derivatives of data represented as a Chebyshev expansion. Notice that the recurrence (5.28) defining the anti derivative of a function can also be used to define a derivative by interchanging the order. Specifically, we seek the derivative of truncated expansion (5.11). The derivative of the function will have it's own Chebyshev series, i.e.,

$$\frac{d}{dx}f(x) = {\sum_{n=1}^{N}}' b_n T_{n-1}(x), \quad (5.41)$$

where the coefficients of the derivative of the function are related to those of the original function through the backwards recurrence relation

$$b_{n-1} = 2(n-1)a_n + b_{n+1} \quad (5.42)$$

for $n = N-1, N-2, \ldots, 3, 2$ starting with values $b_N = 0$ and

$$b_{N-1} = 2(N-1)a_N. \quad (5.43)$$

In the development of our numerical algorithms in this thesis, we will be interested in computing derivatives of functions which are either strictly even or odd. We will specialize the algorithm outlined above for general data to the particular cases of even or odd functions in that follows.

Consider first the *odd* truncated Chebyshev series expansion

$$f(x) = \sum_{i=1}^{N} A_{2i} T_{2i-1}(x). \tag{5.44}$$

The derivative of this function will necessarily be *even* and can therefore be represented as

$$\frac{d}{dx} f(x) = {\sum_{i=1}^{N}}' B_{2i-1} T_{2i-2}(x), \tag{5.45}$$

with coefficients given by [23, eqn. 2.52]

$$B_{2i-1} = 2 \sum_{\ell=i}^{N} (2\ell - 1) A_{2\ell}, \qquad i = 1, 2, \ldots, N. \tag{5.46}$$

We can see that this gives rise to the following useful backwards recursion

$$B_{2i-1} = B_{2i+1} + 2(2i-1) A_{2i}, \qquad k = N-1, \ldots, 2, 1. \tag{5.47}$$

with starting value $B_{2N-1} = 2(2N-1)A_{2N}$. These are well-known results; see for example [23, eqn. 2.51].

The results corresponding to the derivative of an even Chebyshev series are nearly identical; we state them here for convenience in developing our numerical algorithm. Given the *even* truncated Chebyshev series expansion

$$f(x) = {\sum_{i=1}^{N}}' A_{2i-1} T_{2i-2}(x) \tag{5.48}$$

we have the derivative, which is necessarily an *odd* function, defined as

$$\frac{d}{dr} f(x) = \sum_{i=1}^{N} B_{2i} T_{2i-1}(x). \tag{5.49}$$

The coefficients of the expansion are given by [23, eqn. 2.52]

$$B_{2i} = 4 \sum_{\ell=i}^{N-1} \ell A_{2\ell+1}, \qquad i = 1, 2, \ldots, N. \tag{5.50}$$

Taking the convention that the sum vanishes when the sum index exceeds the upper limit, this formula gives rise to the following useful backwards recursion

$$B_{2i} = B_{2i+2} + 4iA_{2i+1}, \qquad k = N-1, \ldots, 1, \tag{5.51}$$

with starting value $B_{2N} = 0$.

5.5 Other useful series manipulations

We consider the *odd* Chebyshev expansion (5.44). In view of the recurrence relation (5.2) for the first kind polynomials, the product of an odd function with its variable will necessarily be *even* and can be represented as

$$xf(x) = \sum_{i=1}^{N} A_{2i} x T_{2i-1}(x) = \sum_{i=1}^{N} \frac{A_{2i}}{2} \left(T_{2i}(x) + T_{2i-2}(x) \right). \tag{5.52}$$

The simple index change $i = n - 1$ in the first term of the right sum of equation (5.52) results in

$$\sum_{i=1}^{N} \frac{A_{2i}}{2} T_{2i}(x) = \sum_{n=2}^{N+1} \frac{A_{2n-2}}{2} T_{2n-2}(x). \tag{5.53}$$

Substituting this result into equation (5.52) allows us to easily combine the sums, resulting in the expansion

$$xf(x) = {\sum_{i=1}^{N+1}}' B_{2i-1} T_{2i-2}(x), \tag{5.54}$$

where $B_1 = A_2$, $B_{2N+1} = A_{2N}/2$ and

$$B_{2i-1} = \frac{1}{2}(A_{2i} + A_{2i-2}), \qquad i = 2, 3, \ldots, N. \tag{5.55}$$

In a similar way, we consider the *even* Chebyshev expansion (5.48). In view of the recurrence relation (5.2) for the first kind polynomials, the product of an even function with its variable will necessarily be *odd* and can be represented as

$$xf(x) = {\sum_{i=1}^{N}}' A_{2i-1} x T_{2i-2}(x) = \frac{A_1}{2} + \sum_{i=2}^{N} \frac{A_{2i-1}}{2} \left(T_{2i-1}(x) + T_{2i-3}(x) \right) \tag{5.56}$$

The simple index change $i = n + 1$ in the second term of the right sum of equation (5.56) results in

$$\sum_{i=2}^{N} \frac{A_{2i-1}}{2} T_{2i-3}(x) = \sum_{n=1}^{N-1} \frac{A_{2n+1}}{2} T_{2n-1}(x). \tag{5.57}$$

Substituting this result into equation (5.56) allows us to easily combine the sums, resulting in the expansion

$$xf(x) = \sum_{i=1}^{N} B_{2i} T_{2i-1}(x), \tag{5.58}$$

where $B_{2N} = A_{2N-1}/2$ and

$$B_{2i} = \frac{1}{2}(A_{2i-1} + A_{2i+1}), \qquad i = 1, 3, \ldots, N - 1. \tag{5.59}$$

We conclude this section with the presentation of a final result, which is applicable to *odd* Chebyshev expansions (5.44). The quotient of an odd function with its variable will necessarily be *even* and can be represented as

$$\frac{f(x)}{x} = \sum_{i=1}^{N} A_{2i} \frac{T_{2i-1}(x)}{x}. \tag{5.60}$$

The quotient of an odd Chebyshev polynomial with its variable is given by the identity

$$\frac{T_{2n-1}(x)}{x} = 2(-1)^n \sum_{i=1}^{n}{}' (-1)^i T_{2i-2}(x), \qquad n \geq 1. \tag{5.61}$$

Substituting equation (5.61) in (5.60) and reversing the order of summation yields the even Chebyshev expansion

$$\frac{f(x)}{x} = \sum_{i=1}^{N}{}' B_{2i-1} T_{2i-2}(x), \qquad N \geq 1, \tag{5.62}$$

where

$$B_{2i-1} = 2(-1)^i \sum_{\ell=i}^{N} (-1)^\ell A_{2\ell} \qquad i = 1, \ldots, N. \tag{5.63}$$

We can see that this gives rise to the following useful backwards recursion: $B_{2N-1} = 2A_{2N}$,

$$B_{2i-1} = 2A_{2i} - B_{2i+1}, \qquad i = N-1, \ldots, 1. \tag{5.64}$$

This is consistent with [25, eqn. 5.8.13].

Chapter 6

Numerical Methods

In this Chapter we develop our numerical treatment of the problem. A excellent reference text useful in understanding basic numerical approaches to blood flow problems was produced by Owens and Phillips [27]. For the specific problem at hand, numerical solutions of the system of equations produced by Yeleswarapu et. al [1] based on finite difference methods were shown to agree well with experiment in several cases of physiological interest. Another numerical method devised by Pontrelli [14] is based on a Crank-Nicholson scheme together with iteration at each time step to resolve the nonlinear terms. The numerical method at each step of iteration requires the inversion of a non-banded linear system by means of Gaussian elimination. The resulting method is first order in time and very slow. The novel numerical method we will outline as part of this work will be based on a spectral Chebyshev-tau method [28] and a fourth-order Runge-Kutta time stepping scheme [25, 28].

6.1 Equivalent System of Equations

In order to present an equivalent system of equations to (3.51), (3.52) and (3.53) in a clean and systematic way, we make the following replacements for the dependent variables:

$$\begin{aligned}
\frac{\partial u_z}{\partial r} &= A(r,t) && (6.1)\\
S_{rz}(r,t) &= \frac{r}{2}f(t) + B(r,t) && (6.2)\\
S_{zz}(r,t) &= C(r,t) && (6.3)
\end{aligned}$$

The functions $A(r,t)$, $B(r,t)$ and $C(r,t)$ will be the unknowns of our problem. These replacements will be useful in easily identifying spatial versus spectral representations of the dependent variables and organizing our numerical treatment of the problem. Explicitly extracting the pressure function $f(t)$ in equation (6.2) will also be useful in simplifying the boundary conditions to be applied to the problem. Taking the r-derivative of equation (3.51), interchanging the order of r and t derivatives on the left-hand side, and using the variable replacements above, we obtain

$$\frac{\partial A}{\partial t} = \frac{\partial}{\partial r}\left(\frac{\partial B}{\partial r} + \frac{B}{r}\right) \tag{6.4}$$

Next, using the replacements (6.1), (6.2) and (6.3) in equations (3.52) and (3.53) leads directly to

$$\frac{\partial B}{\partial t} = -\frac{1}{\lambda_1}B - \frac{r}{2}\left(f'(t) + \frac{1}{\lambda_1}f(t)\right) + \frac{1}{\lambda_1 \mathrm{Wo}}\left((1-\beta)G + \beta A + \lambda_2\frac{\partial A}{\partial t}\right) \tag{6.5}$$

and

$$\frac{\partial C}{\partial t} = -\frac{1}{\lambda_1}C + H. \tag{6.6}$$

Note that in equations (6.5) and (6.6) we have introduced the functions representing the nonlinear terms

$$G = G(r,t) = A(r,t)F(A(r,t)) \tag{6.7}$$

and

$$H = H(r,t) = 2A(r,t)\left(\frac{r}{2}f(t) + B(r,t) - \frac{\lambda_2}{\lambda_1 \mathrm{Wo}}A(r,t)\right). \tag{6.8}$$

The function F in (6.7) remains the non-dimensional viscosity function defined in equation (2.12). Equations (6.4), (6.5) and (6.6) will form the basis for our numerical treatment of the blood flow problem in this thesis. In their new form, it's clear that the time evolution of the problem does not actually rely on the velocity u_z but rather its spatial derivative represented here by the function A. This will have implications on the boundary conditions that we impose. It's also important to note that interchanging the order of r and t derivatives in arriving at equation (6.4) relies on certain assumptions on the smoothness of the solution that were not necessarily present in the original system of equations. This will motivate us to also present an alternative treatment of the pressure function in order to ensure smoothness of the solutions, particularly around $t = 0$.

6.2 Constraints on the Solution

An inspection of our system of equations (6.4), (6.5) and (6.6) allows us to make several observations that will be useful in imposing constraints on the solution. Since the system contains two r-derivatives of B, but no r-derivatives of A and C we should expect to impose two spatial conditions on the solution. We will produce the two needed conditions in what follows.

Our first condition is based on required symmetry properties of the solution. In particular, the velocity profile must be symmetric about the tube centerline owing to the circular symmetry of the domain boundary and the no-slip conditions that we apply there. Indeed, the velocity $u_z(r,t)$ must be an even function, i.e., $u_z(-r,t) = u_z(r,t)$. This, in turn, implies that the r-derivative of u_z, and hence A, must be an odd function of r, i.e., $A(-r,t) = -A(r,t)$. If A is odd, then B and G must also necessarily be odd (since, as discussed in section $F = F(A)$ is an even function of A and hence an even function of r). Further, if A is and B are odd, then C and H must be even. Imposing these symmetry constraints as indicated, together with the requirement that solutions remain finite in the domain (and on the tube center line in particular), constitutes our first condition on the solution. These constraints will be realized by the expansions for the unknowns that we introduce in what follows.

Our second condition is based on no-slip boundary conditions on the wall of the tube $r = \pm 1$, i.e., $u_z(\pm 1, t) = 0$ for all $t > 0$. The system of equations (6.4), (6.5) and (6.6) does not contain u_z directly, and indeed, we develop our condition from consideration of one of the original equations (3.51). Imposing a vanishing time derivative of the velocity at the wall we require

$$\lim_{r=\pm 1} \frac{\partial u_z}{\partial t} = \lim_{r=\pm 1} \left(-f(t) + \frac{\partial S_{rz}}{\partial r} + \frac{S_{rz}}{r} \right) = 0 \tag{6.9}$$

This condition will be equivalent to the no-slip condition $u_z(\pm 1, t) = 0$ provided the initial velocity at $t = 0$ also vanishes at $r = \pm 1$ and that the velocity is a continuous function of time at $t = 0$. Indeed we need to guarantee certain smoothness conditions in the t variable, in particular avoiding discontinuous initial conditions, such as impulsively started pressure gradients at $t = 0$. We will discuss this in more detail below. In terms of the new dependent variables above, our second condition to be imposed on the solution may be stated as

$$\lim_{r=\pm 1} \left(\frac{\partial B}{\partial r} + \frac{B}{r} \right) = 0. \tag{6.10}$$

6.3 Chebyshev Expansion of the Unknowns

In this section we will set up a spatial grid for the problem together with appropriate expansions for the unknown quantities. We will seek spatial values of the solution at $M = 2N$ points for $r \in (-1, 1)$ and N a positive integer; while the spatial expansions of the solution will indeed possess M points, the spectral representations will contain only N non-zero values due to even/odd properties. Note that the cylindrical coordinate system requires $r > 0$; our choice to extend this to $r \in (-1, 1)$ is allowed by the required symmetry properties of the solution and fits naturally into the theory of Chebyshev approximation.

Following details regarding Chebyshev expansions in Chapter 5 we will test the unknown functions at the zeros of the Chebyshev polynomial $T_M(x)$ which occur at radial positions

$$r_k = \cos\left[\left(k - \frac{1}{2}\right)\Delta\theta\right] \qquad k = 1, 2, \ldots, M. \tag{6.11}$$

The constant stepsize in the θ-variable is given by

$$\Delta\theta = \frac{\pi}{M}, \tag{6.12}$$

where $M = 2N$. For $k = 1, 2, \ldots, M$ we use the following expansions for the solutions and related field quantities:

$$A(r_k, t) = \frac{1}{2}\hat{A}_1(t) + \sum_{i=2}^{M} \hat{A}_i(t) T_{i-1}(r_k), \tag{6.13}$$

$$B(r_k, t) = \frac{1}{2}\hat{B}_1(t) + \sum_{i=2}^{M} \hat{B}_i(t) T_{i-1}(r_k), \tag{6.14}$$

$$C(r_k, t) = \frac{1}{2}\hat{C}_1(t) + \sum_{i=2}^{M} \hat{C}_i(t) T_{i-1}(r_k), \tag{6.15}$$

$$G(r_k, t) = \frac{1}{2}\hat{G}_1(t) + \sum_{i=2}^{M} \hat{G}_i(t) T_{i-1}(r_k), \tag{6.16}$$

$$H(r_k, t) = \frac{1}{2}\hat{H}_1(t) + \sum_{i=2}^{M} \hat{H}_i(t) T_{i-1}(r_k). \tag{6.17}$$

All solutions in this form will remain finite in the domain, provided the expansion coefficients also remain finite. For $i = 1, 2, \ldots, M$ the coefficients may be obtained by means of the expansions

$$\hat{A}_i(t) = \frac{2}{M} \sum_{k=1}^{M} A(r_k, t) T_{i-1}(r_k), \tag{6.18}$$

$$\hat{B}_i(t) = \frac{2}{M} \sum_{k=1}^{M} B(r_k, t) T_{i-1}(r_k), \tag{6.19}$$

$$\hat{C}_i(t) = \frac{2}{M}\sum_{k=1}^{M} C(r_k,t)T_{i-1}(r_k), \tag{6.20}$$

$$\hat{G}_i(t) = \frac{2}{M}\sum_{k=1}^{M} G(r_k,t)T_{i-1}(r_k), \tag{6.21}$$

$$\hat{H}_i(t) = \frac{2}{M}\sum_{k=1}^{M} H(r_k,t)T_{i-1}(r_k). \tag{6.22}$$

In the formulation of our numerical solver, it will be convenient to express the field quantities and their corresponding spectral amplitudes in terms of M-element arrays as follows:

$$\mathbf{A}(t) = \{A(r_k,t)\}_{k=1}^{M}, \qquad \hat{\mathbf{A}}(t) = \{\hat{A}_i(t)\}_{i=1}^{M}, \tag{6.23}$$

$$\mathbf{B}(t) = \{B(r_k,t)\}_{k=1}^{M}, \qquad \hat{\mathbf{B}}(t) = \{\hat{B}_i(t)\}_{i=1}^{M}, \tag{6.24}$$

$$\mathbf{C}(t) = \{C(r_k,t)\}_{k=1}^{M}, \qquad \hat{\mathbf{C}}(t) = \{\hat{C}_i(t)\}_{i=1}^{M}, \tag{6.25}$$

$$\mathbf{G}(t) = \{G(r_k,t)\}_{k=1}^{M}, \qquad \hat{\mathbf{G}}(t) = \{\hat{G}_i(t)\}_{i=1}^{M}, \tag{6.26}$$

$$\mathbf{H}(t) = \{H(r_k,t)\}_{k=1}^{M}, \qquad \hat{\mathbf{H}}(t) = \{\hat{H}_i(t)\}_{i=1}^{M}. \tag{6.27}$$

Finally, we can relate the field quantities and their spectral amplitudes using the *un-normalized* M-element DCT-II and DCT-III transforms as follows:

$$\hat{\mathbf{A}}(t) = \frac{1}{M}\mathrm{DCTII}(\mathbf{A}(t)), \qquad \mathbf{A}(t) = \frac{1}{2}\mathrm{DCTIII}(\hat{\mathbf{A}}(t)) \tag{6.28}$$

$$\hat{\mathbf{B}}(t) = \frac{1}{M}\mathrm{DCTII}(\mathbf{B}(t)), \qquad \mathbf{B}(t) = \frac{1}{2}\mathrm{DCTIII}(\hat{\mathbf{B}}(t)) \tag{6.29}$$

$$\hat{\mathbf{C}}(t) = \frac{1}{M}\mathrm{DCTII}(\mathbf{C}(t)), \qquad \mathbf{C}(t) = \frac{1}{2}\mathrm{DCTIII}(\hat{\mathbf{C}}(t)) \tag{6.30}$$

$$\hat{\mathbf{G}}(t) = \frac{1}{M}\mathrm{DCTII}(\mathbf{G}(t)), \qquad \mathbf{G}(t) = \frac{1}{2}\mathrm{DCTIII}(\hat{\mathbf{G}}(t)) \tag{6.31}$$

$$\hat{\mathbf{H}}(t) = \frac{1}{M}\mathrm{DCTII}(\mathbf{H}(t)), \qquad \mathbf{H}(t) = \frac{1}{2}\mathrm{DCTIII}(\hat{\mathbf{H}}(t)) \tag{6.32}$$

The normalization of the transforms is accomplished by applying multiplicative factors $1/M$ or $1/2$, which are included above.

The required even/odd properties of the solutions can be enforced by considering the corresponding properties of the Chebyshev polynomials, namely, $T_j(-r) = (-1)^j T_j(r)$. In order to ensure odd functions we therefore require

$$\hat{A}_{2i-1}(t) = 0, \qquad \hat{A}_{2i}(t) = a_i, \qquad i = 1, 2, \ldots, N. \tag{6.33}$$

$$\hat{B}_{2i-1}(t) = 0, \qquad \hat{B}_{2i}(t) = b_i, \qquad i = 1, 2, \ldots, N. \tag{6.34}$$

$$\hat{G}_{2i-1}(t) = 0, \qquad \hat{G}_{2i}(t) = g_i, \qquad i = 1, 2, \ldots, N. \tag{6.35}$$

Similarly, in order to ensure even functions we require

$$\hat{C}_{2i-1}(t) = c_i, \qquad \hat{C}_{2i}(t) = 0, \qquad i = 1, 2, \ldots, N. \tag{6.36}$$

$$\hat{H}_{2i-1}(t) = h_i, \qquad \hat{H}_{2i}(t) = 0, \qquad i = 1, 2, \ldots, N. \tag{6.37}$$

We can therefore see that the dimension of the problem in the spectral domain, where the unknowns are a_i, b_i, c_i, g_i and h_i, is one half of the dimension of the problem in the spatial domain.

6.4 Equivalent Boundary Conditions

As we saw in the previous section, the required symmetry/finiteness constraint on the solution can be satisfied with a careful choice of function expansion. Our method for satisfying the boundary conditions (6.10), on the other hand, involves a careful manipulation of one of these expansions. In particular, for the function $B(r, t)$ expanded in terms of odd Chebyshev polynomials as per equations (6.14) and (6.34), we form the quantity $U(r,t)$ as

$$U(r,t) = \frac{\partial B}{\partial r}(r,t) + \frac{B(r,t)}{r} = {\sum_{i=1}^{N}}{}' \hat{U}_{2i-1}(t) T_{2i-2}(r). \tag{6.38}$$

The expansion of the right-hand side of equation (6.38) is necessarily even since $B(r,t)$ is an odd function in r. The formula for the Chebyshev coefficients of the derivative of an odd function (5.46) together with the formula for the quotient of an odd function with its spatial variable (5.63) lead directly the the following expression for the Chebyshev coefficients of $U(r,t)$:

$$\hat{U}_{2i-1}(t) = 2\sum_{\ell=i}^{N}(2\ell-1)\hat{B}_{2\ell}(t) + 2\sum_{\ell=i}^{N}(-1)^{i+\ell}\hat{B}_{2\ell}(t), \qquad i = 1, 2, \ldots, N. \tag{6.39}$$

Once the Chebyshev coefficients (6.39) have been obtained, it is straightforward to evaluate the Chebyshev expansion for $U(r,t)$ on the endpoints $r = \pm 1$ using the endpoint conditions for Chebyshev polynomials (5.30). In particular, the following limit, important to the formualtion of our boundary conditions, may be obtained:

$$\lim_{r=\pm 1}\left(\frac{\partial B}{\partial r} + \frac{B}{r}\right) = {\sum_{i=1}^{N}}{}' \hat{U}_{2i-1}(t). \tag{6.40}$$

In what follows, we will show that if $\hat{U}_{2i-1}(t)$ is defined as in equation (6.39), then the sum on the right hand side of equation (6.40) simplifies to

$$\begin{aligned} {\sum_{i=1}^{N}}{}' \hat{U}_{2i-1}(t) &= 2{\sum_{i=1}^{N}}{}'\sum_{\ell=i}^{N}(2\ell-1)\hat{B}_{2\ell}(t) + 2{\sum_{i=1}^{N}}{}'\sum_{\ell=i}^{N}(-1)^{i+\ell}\hat{B}_{2\ell}(t) \\ &= \sum_{i=1}^{N}\left[1 + (2i-1)^2\right]\hat{B}_{2i}(t). \end{aligned} \tag{6.41}$$

Hence the boundary conditions (6.10) are satisfied provided

$$\sum_{i=1}^{N} \left[1 + (2i-1)^2\right] \hat{B}_{2i}(t) = 0. \tag{6.42}$$

Equivalently, with vanishing initial conditions chosen such that $\hat{B}_{2k}(0) = 0$ for $k = 1, \ldots N$ and initial data with a continuous derivative at $t = 0$, we can also enforce the following condition on the time derivatives of $\hat{B}_{2k}(t)$:

$$\sum_{i=1}^{N} \left[1 + (2i-1)^2\right] \hat{B}'_{2i}(t) = 0. \tag{6.43}$$

In order to establish the validity of equation (6.41), we will employ a series rearrangment technique that can be found in reference [29]. Indeed, for n, k and N integers and $\alpha_{k,n}$ a series coefficient we have the equivalence

$$\sum_{n=0}^{N} \sum_{k=0}^{n} \alpha_{k,n} = \sum_{n=0}^{N} \sum_{k=0}^{N-n} \alpha_{k,n+k}. \tag{6.44}$$

This summation identity has the following equivalent form, more suitable for our needs:

$$\sum_{n=1}^{N} \sum_{k=1}^{n} \alpha_{k,n} = \sum_{n=1}^{N} \sum_{k=1}^{N-n+1} \alpha_{k,n+k-1}. \tag{6.45}$$

The summation equivalence (6.45) may be interpreted as summing elements in an upper-triangular matrix in different orders; the left-hand side of (6.45) corresponds to a summation on a column by column basis, where data in one column is summed from the first row down to the main diagonal element; the right-hand side of (6.45) corresponds to a summation along diagonal bands, starting with the main diagonal and then summing along the first upper diagonal band, followed by the second upper diagonal band, etc.

To see how this is applied, we consider the first double sum on the right-hand side of equation (6.41). Extracting the first term in the outer sum and ensuring that it is halved as per the meaning of the prime on the sum, we obtain

$$2 \sum_{i=1}^{N}{}' \sum_{\ell=i}^{N} (2\ell - 1)\hat{B}_{2\ell} = 2 \sum_{i=1}^{N} \sum_{\ell=i}^{N} (2\ell - 1)\hat{B}_{2\ell} - \sum_{i=1}^{N} (2i - 1)\hat{B}_{2i}. \tag{6.46}$$

Next, setting $j = \ell - i + 1$ in the first sum on the right-hand side of equation (6.46) gives

$$2 \sum_{i=1}^{N}{}' \sum_{\ell=i}^{N} (2\ell - 1)\hat{B}_{2\ell} = 2 \sum_{i=1}^{N} \sum_{j=1}^{N-i+1} (2j + 2i - 3)\hat{B}_{2j+2i-2} - \sum_{i=1}^{N} (2i - 1)\hat{B}_{2i}. \tag{6.47}$$

Applying the series rearrangement (6.45) to the first sum on the right-hand side above results in

$$2 \sum_{i=1}^{N}{}' \sum_{\ell=i}^{N} (2\ell - 1)\hat{B}_{2\ell} = 2 \sum_{i=1}^{N} \sum_{j=1}^{i} (2i - 1)\hat{B}_{2i} - \sum_{i=1}^{N} (2i - 1)\hat{B}_{2i}. \tag{6.48}$$

It can be seen that after the re-arrangement, the argument of the double sum no longer depends on the inner summation index, j. Furthermore, since

$$\sum_{j=1}^{i} (1) = i, \tag{6.49}$$

we obtain

$$2 \sum_{i=1}^{N}{}' \sum_{\ell=i}^{N} (2\ell - 1)\hat{B}_{2\ell} = 2 \sum_{i=1}^{N} i(2i - 1)\hat{B}_{2i} - \sum_{i=1}^{N} (2i - 1)\hat{B}_{2i}. \tag{6.50}$$

Combining the sums on the right-hand side, this last expression is easily simplified to obtain

$$2 \sum_{i=1}^{N}{}' \sum_{\ell=i}^{N} (2\ell - 1)\hat{B}_{2\ell} = \sum_{i=1}^{N} (2i - 1)^2 \hat{B}_{2i}. \tag{6.51}$$

Following essentially the same steps, we consider the second double sum on the right-hand side of equation (6.41). Extracting the first term in the outer sum and ensuring that it is halved as per the meaning of the prime on the sum, we obtain

$$2\sum_{i=1}^{N}{}' \sum_{\ell=i}^{N}(-1)^{i+\ell}\hat{B}_{2\ell} = 2\sum_{i=1}^{N}\sum_{\ell=i}^{N}(-1)^{i+\ell}\hat{B}_{2\ell} - \sum_{i=1}^{N}(-1)^{i+1}\hat{B}_{2i}. \tag{6.52}$$

Next, setting $j = \ell - i + 1$ in the first sum on the right-hand side of equation (6.52) gives

$$2\sum_{i=1}^{N}{}' \sum_{\ell=i}^{N}(-1)^{i+\ell}\hat{B}_{2\ell} = 2\sum_{i=1}^{N}\sum_{j=i}^{N-i+1}(-1)^{j+2i-1}\hat{B}_{2j+2i-2} - \sum_{i=1}^{N}(-1)^{i+1}\hat{B}_{2i}. \tag{6.53}$$

Applying the series rearrangement (6.45) to the first sum on the right-hand side above results in

$$2\sum_{i=1}^{N}{}' \sum_{\ell=i}^{N}(-1)^{i+\ell}\hat{B}_{2\ell} = 2\sum_{i=1}^{N}\hat{B}_{2i}\sum_{j=1}^{i}(-1)^{j-1} - \sum_{i=1}^{N}(-1)^{i+1}\hat{B}_{2i}. \tag{6.54}$$

Furthermore, since

$$\sum_{j=1}^{i}(-1)^{j-1} = \frac{1}{2}\left[1-(-1)^{i}\right], \tag{6.55}$$

we obtain the simplified result

$$2\sum_{i=1}^{N}{}' \sum_{\ell=i}^{N}(-1)^{i+\ell}\hat{B}_{2\ell} = \sum_{i=1}^{N}\hat{B}_{2i}. \tag{6.56}$$

Finally, making the replacements for the double sums in equation (6.41) as per (6.51) and (6.56) establishes the validity of the simplified form on the third line of that equation.

6.5 Solver

The idea of using a Runge-Kutta time discretization in combination with a spectral Chebyshev method as the basis of a PDE solver on a finite domain isn't new. Indeed, solvers constructed in such a way have been widely-used and remarkably successful; see [28] and references therein. The novelty on our part is to apply these tools to design a simple yet powerful algorithm to produce accurate numerical solutions to the blood flow problem outlined in this thesis, while addressing the implementation details that are unique to this problem along the way. In particular, we outline below an algorithm using an RK4 time stepping in combination with a Chebyshev tau method on $r \in (-1, 1)$ and $t > 0$.

As is typical for Chebyshev tau methods, the problem is formulated not in terms of spatial values of the solution but rather in terms of its Chebyshev coefficients. In the transformed space, equations (6.4), (6.5) and (6.6) result in a system of first order ordinary differential equations of the form

$$\begin{aligned} \frac{d}{dt}\hat{\mathbf{A}}(t) &= \mathbf{F}_A\Big[t, \hat{\mathbf{A}}(t), \hat{\mathbf{B}}(t), \hat{\mathbf{C}}(t)\Big], \\ \frac{d}{dt}\hat{\mathbf{B}}(t) &= \mathbf{F}_B\Big[t, \hat{\mathbf{A}}(t), \hat{\mathbf{B}}(t), \hat{\mathbf{C}}(t)\Big], \\ \frac{d}{dt}\hat{\mathbf{C}}(t) &= \mathbf{F}_C\Big[t, \hat{\mathbf{A}}(t), \hat{\mathbf{B}}(t), \hat{\mathbf{C}}(t)\Big], \end{aligned} \tag{6.57}$$

subject to initial conditions

$$\hat{\mathbf{A}}(0) = \hat{\mathbf{B}}(0) = \hat{\mathbf{C}}(0) = \mathbf{0}. \tag{6.58}$$

The functions $\mathbf{F}_X$ for subscript labels $X = A, B, C$ represent the normalized DCT-II of the right-hand side of equations (6.4), (6.5) and (6.6), respectively. As part of our algorithm description we will precisely define each of these functions in what follows. We will seek numerical solutions to the problem on the equi-spaced time grid

$$t_k = (k-1)\Delta t \qquad k = 1, 2, \ldots, N_t, \tag{6.59}$$

where N_t is the maximum number of time steps used in our code. Defining $T_{\max}$ as the final solution time, the time step is given by

$$\Delta t = \frac{T_{\max}}{N_t - 1}. \tag{6.60}$$

Applying the standard RK4 algorithm [30, 25] results in the following time stepping procedure:

$$\begin{aligned}
\hat{\mathbf{A}}(t_k + \Delta t) &= \hat{\mathbf{A}}(t_k) + \frac{\Delta t}{6}\left[\mathbf{K}_{A,1}(t_k) + 2\mathbf{K}_{A,2}(t_k) + 2\mathbf{K}_{A,3}(t_k) + \mathbf{K}_{A,4}(t_k)\right] \\
\hat{\mathbf{B}}(t_k + \Delta t) &= \hat{\mathbf{B}}(t_k) + \frac{\Delta t}{6}\left[\mathbf{K}_{B,1}(t_k) + 2\mathbf{K}_{B,2}(t_k) + 2\mathbf{K}_{B,3}(t_k) + \mathbf{K}_{B,4}(t_k)\right] \\
\hat{\mathbf{C}}(t_k + \Delta t) &= \hat{\mathbf{C}}(t_k) + \frac{\Delta t}{6}\left[\mathbf{K}_{C,1}(t_k) + 2\mathbf{K}_{C,2}(t_k) + 2\mathbf{K}_{C,3}(t_k) + \mathbf{K}_{C,4}(t_k)\right]
\end{aligned} \tag{6.61}$$

for $k = 1, 2, \ldots, N_t - 1$. We apply the time stepping only to the non-zero elements of $\hat{\mathbf{A}}$, $\hat{\mathbf{B}}$ and $\hat{\mathbf{C}}$ as per equations (6.33), (6.34) and (6.36), respectively. At each time step, we must enforce boundary conditions (6.42) on the updated solution at time $t = t_k + \Delta t$. We do this by replacing the $2N$-*th* element of $\hat{\mathbf{B}}$ with

$$\left\{\hat{\mathbf{B}}\right\}_{2N} = \frac{1}{1 + (2N-1)^2} \sum_{i=1}^{N-1} [1 + (2i-1)^2] \left\{\hat{\mathbf{B}}\right\}_{2i}, \tag{6.62}$$

or equivalently,

$$b_N(t) = \frac{1}{1 + (2N-1)^2} \sum_{i=1}^{N-1} [1 + (2i-1)^2] b_i(t). \tag{6.63}$$

The slopes $\mathbf{K}_{X,1}$, $\mathbf{K}_{X,2}$, $\mathbf{K}_{X,3}$ and $\mathbf{K}_{X,4}$ are computed for each $X = A, B, C$ by means of evaluating the functions $\mathbf{F}_X$ using various estimates of the solution as input arguments. The first slope is a direct evaluation of the function with known data:

$$\mathbf{K}_{X,1}(t_k) = \mathbf{F}_X\left[t_k, \hat{\mathbf{A}}(t_k), \hat{\mathbf{B}}(t_k), \hat{\mathbf{C}}(t_k)\right]. \tag{6.64}$$

In equation (6.64), it's assumed that the quantity $\hat{\mathbf{B}}(t_k)$ obeys boundary conditions (6.42) that are either satisfied by the initial conditions or enforced at the previous time step. To compute the second slope, we find approximate values of the solution at $t = t_k + (\Delta t)/2$

using linear extrapolation:

$$\begin{aligned}
\hat{\mathbf{A}}_{\text{app}}\left(t_k + \frac{\Delta t}{2}\right) &= \hat{\mathbf{A}}(t_k) + \frac{(\Delta t)}{2}\mathbf{K}_{A,1}(t_k) \\
\hat{\mathbf{B}}_{\text{app}}\left(t_k + \frac{\Delta t}{2}\right) &= \hat{\mathbf{B}}(t_k) + \frac{(\Delta t)}{2}\mathbf{K}_{B,1}(t_k) \\
\hat{\mathbf{C}}_{\text{app}}\left(t_k + \frac{\Delta t}{2}\right) &= \hat{\mathbf{C}}(t_k) + \frac{(\Delta t)}{2}\mathbf{K}_{C,1}(t_k)
\end{aligned}$$

Next we must enforce boundary conditions (6.42) on the solution estimate. We do this by replacing the $2N$-*th* element of $\hat{\mathbf{B}}_{\text{app}}$ with

$$\left\{\hat{\mathbf{B}}_{\text{app}}\right\}_{2N} = \frac{1}{1+(2N-1)^2}\sum_{i=1}^{N-1}[1+(2i-1)^2]\left\{\hat{\mathbf{B}}_{\text{app}}\right\}_{2i}. \tag{6.65}$$

The second slope is then computed as

$$\mathbf{K}_{X,2}(t_k) = \mathbf{F}_X\left[t_k + \frac{\Delta t}{2}, \hat{\mathbf{A}}_{\text{app}}\left(t_k + \frac{\Delta t}{2}\right), \hat{\mathbf{B}}_{\text{app}}\left(t_k + \frac{\Delta t}{2}\right), \hat{\mathbf{C}}_{\text{app}}\left(t_k + \frac{\Delta t}{2}\right)\right]. \tag{6.66}$$

Computing the remaining slopes follows a near identical procedure. Indeed, to compute the third slope we find approximate values of the solution at $t = t_k + (\Delta t)/2$ using linear extrapolation based on the previous estimates in equation (6.66):

$$\begin{aligned}
\hat{\mathbf{A}}_{\text{app}}\left(t_k + \frac{\Delta t}{2}\right) &= \hat{\mathbf{A}}(t_k) + \frac{(\Delta t)}{2}\mathbf{K}_{A,2}(t_k) \\
\hat{\mathbf{B}}_{\text{app}}\left(t_k + \frac{\Delta t}{2}\right) &= \hat{\mathbf{B}}(t_k) + \frac{(\Delta t)}{2}\mathbf{K}_{B,2}(t_k) \\
\hat{\mathbf{C}}_{\text{app}}\left(t_k + \frac{\Delta t}{2}\right) &= \hat{\mathbf{C}}(t_k) + \frac{(\Delta t)}{2}\mathbf{K}_{C,2}(t_k)
\end{aligned}$$

Such a procedure, where subsequent slope estimates are based on previous slope estimates, is characteristic of explicit Runge-Kutta methods [30]. We again enforce boundary conditions on the estimated solution $\hat{\mathbf{B}}_{\text{app}}$ using (6.65) and then compute the third slope as

$$\mathbf{K}_{X,3}(t_k) = \mathbf{F}_X\left[t_k + \frac{\Delta t}{2}, \hat{\mathbf{A}}_{\text{app}}\left(t_k + \frac{\Delta t}{2}\right), \hat{\mathbf{B}}_{\text{app}}\left(t_k + \frac{\Delta t}{2}\right), \hat{\mathbf{C}}_{\text{app}}\left(t_k + \frac{\Delta t}{2}\right)\right]. \tag{6.67}$$

Finally, we compute the fourth slope using approximate values of the solution at $t = t_k + \Delta t$ based on the slopes in equation (6.67):

$$\begin{aligned}
\hat{\mathbf{A}}_{\text{app}}(t_k + \Delta t) &= \hat{\mathbf{A}}(t_k) + (\Delta t)\mathbf{K}_{A,3}(t_k) \\
\hat{\mathbf{B}}_{\text{app}}(t_k + \Delta t) &= \hat{\mathbf{B}}(t_k) + (\Delta t)\mathbf{K}_{B,3}(t_k) \\
\hat{\mathbf{C}}_{\text{app}}(t_k + \Delta t) &= \hat{\mathbf{C}}(t_k) + (\Delta t)\mathbf{K}_{C,3}(t_k)
\end{aligned}$$

Enforcing boundary conditions on $\hat{\mathbf{B}}_{\text{app}}$ using (6.65) the fourth slope is then given as

$$\mathbf{K}_{X,4}(t_k) = \mathbf{F}_X\left[t_k + \Delta t, \hat{\mathbf{A}}_{\text{app}}(t_k + \Delta t), \hat{\mathbf{B}}_{\text{app}}(t_k + \Delta t), \hat{\mathbf{C}}_{\text{app}}(t_k + \Delta t)\right]. \tag{6.68}$$

With these four slopes in hand, we can compute a solution estimate at $t + \Delta t$ using the iteration (6.61) and then apply boundary conditions (6.62), thus advancing the solution one time level.

As can be seen, the RK4 time stepping outlined above requires the repeated evaluation of the functions $\mathbf{F}_X$ for subscript labels $X = A, B, C$. We will outline the algorithmic details used in our code below. Given input arguments $\hat{\mathbf{A}}(t)$, $\hat{\mathbf{B}}(t)$ and $\hat{\mathbf{C}}(t)$, these functions represent the time derivatives of the $M = 2N$ element arrays

$$\frac{d}{dt}\hat{\mathbf{A}}(t), \qquad \frac{d}{dt}\hat{\mathbf{B}}(t), \qquad \frac{d}{dt}\hat{\mathbf{C}}(t),$$

or equivalently, in view of the even/odd properties (6.33), (6.34) and (6.36), these functions represent the time derivatives of array components

$$\frac{d}{dt}a_i(t), \qquad \frac{d}{dt}b_i(t), \qquad \frac{d}{dt}c_i(t),$$

for $i = 1, 2, \ldots, N$. In what follows, we will understand the prime to indicate a time derivative, not to be confused with the prime notation associated with a summation.

In order to facilitate our presentation of our algorithm, we introduce the $M = 2N$ element arrays

$$\mathbf{U}(t) = \{U(r_k, t)\}_{k=1}^{M}, \qquad \hat{\mathbf{U}}(t) = \{\hat{U}_i(t)\}_{i=1}^{M}, \tag{6.69}$$

where $U(r,t)$ is defined in (6.38). These arrays correspond to a normalized transform pair as follows:

$$\hat{\mathbf{U}}(t) = \frac{1}{M}\mathrm{DCTII}(\mathbf{U}(t)), \qquad \mathbf{U}(t) = \frac{1}{2}\mathrm{DCTIII}(\hat{\mathbf{U}}(t)). \tag{6.70}$$

As indicated in equation (6.38) the function $U(r,t)$ is necessarily an *even* function and therefore the coefficients of the DCT-II of $U(r,t)$ must obey properties

$$\hat{U}_{2i-1}(t) = u_i(t), \qquad \hat{U}_{2i}(t) = 0, \qquad i = 1, 2, \ldots, N. \tag{6.71}$$

It's not difficult to see from equation (6.4) that we must have

$$\frac{\partial A}{\partial t} = \frac{\partial U}{\partial r} \tag{6.72}$$

and hence each side of equation (6.72) must be represented by an *odd* function. In order to compute $a_i'(t)$ we will first compute $u_i(t)$ and from these obtain the Chebyshev coefficients of the r derivative of $U(r,t)$. An explicit formula for the Chebyshev series coefficients $u_i(t) = \hat{U}_{2i-1}(t)$ for $i = 1, \ldots, N$ is defined in (6.38). Instead of a direct evaluation of the sums in equation (6.39), we produce these quantities efficiently by means of recursion relations. Let

$$u_i = \alpha_i^{(1)} + \alpha_i^{(2)} \qquad i = 1, 2, \ldots, N. \tag{6.73}$$

We can produce the coefficients $\alpha_i^{(1)}$ from b_i by applying the recursion (5.47) to obtain

$$\begin{aligned}\alpha_N^{(1)} &= 2(2N-1)b_N \\ \alpha_i^{(1)} &= \alpha_{i+1}^{(1)} + 2(2i-1)b_i, \qquad i = N-1, N-2, \ldots, 1.\end{aligned} \tag{6.74}$$

Similarly, we can produce the coefficients $\alpha_i^{(2)}$ from b_i by applying the recursion (5.64) to obtain

$$\begin{aligned} \alpha_N^{(2)} &= 2b_N \\ \alpha_i^{(2)} &= -\alpha_{i+1}^{(2)} + 2b_i, \qquad i = N-1, N-2, \ldots, 1. \end{aligned} \tag{6.75}$$

With the sum of these last two quantities yielding u_i we can apply the recursion (5.51) to obtain the necessary time derivatives

$$\begin{aligned} a'_N(t) &= 0 \\ a'_i(t) &= a'_{i+1}(t) + 4iu_{i+1}(t), \qquad i = N-1, N-2, \ldots, 1. \end{aligned} \tag{6.76}$$

Based on the definitions we have established in this section, it's not difficult to see that the non-zero elements of the Chebyshev transform of equation (6.5) lead to the following formulas for the evaluation of the time derivatives $b'_i(t)$:

$$b'_1(t) = -\frac{1}{2}f'(t) - \frac{1}{2\lambda_1}f(t) - \frac{1}{\lambda_1}b_1(t) + \frac{1}{\lambda_1 \mathrm{Wo}}\left((1-\beta)g_1(t) + \beta a_1(t) + \lambda_2 a'_1(t)\right) \tag{6.77}$$

and

$$b'_i(t) = -\frac{1}{\lambda_1}b_i(t) + \frac{1}{\lambda_1 \mathrm{Wo}}\left((1-\beta)g_i(t) + \beta a_i(t) + \lambda_2 a'_i(t)\right), \qquad i = 2, 3, \ldots, N-1. \tag{6.78}$$

Values for the time derivatives $a'_i(t)$ in equations (6.77) and (6.78) are obtained from (6.76). The time derivative $b'_N(t)$ is not evaluated as updated values of $b_N(t)$ are produced by enforcing boundary conditions. Consistent with (6.35) and above, values for $g_i = \hat{G}_{2i}$ are computed as follows:

(1) Populate the M-element array of spectral values $\hat{\mathbf{A}}(t) = \{\hat{A}_i(t)\}_{i=1}^{M}$ using

$$\hat{A}_{2i} = a_i, \qquad \hat{A}_{2i-1} = 0, \qquad i = 1, 2, \ldots, N. \tag{6.79}$$

(2) Obtain the array of spatial values $\mathbf{A}(t) = \{A(r_k, t)\}_{k=1}^{M}$ by means of a normalized fast M-point DCT-III:

$$\mathbf{A}(t) = \frac{1}{2}\text{DCTIII}(\hat{\mathbf{A}}(t)). \tag{6.80}$$

(3) Populate the M-element array of spatial values $\mathbf{G}(t) = \{G(r_k, t)\}_{k=1}^{M}$ as the product of functions

$$G(r_k, t) = A(r_k, t)F(A(r_k, t)), \qquad k = 1, 2, \ldots, M. \tag{6.81}$$

(4) Obtain the array of spectral values $\hat{\mathbf{G}}(t) = \{\hat{G}_i(t)\}_{i=1}^{M}$ by means of a normalized fast M-point DCT-II:

$$\hat{\mathbf{G}}(t) = \frac{1}{M}\text{DCTII}(\mathbf{G}(t)). \tag{6.82}$$

Values $g_i = \hat{G}_{2i}$ are then extracted for use in equations (6.77) and (6.78).

Some comments on the procedure outlined above to produce the Chebyshev coefficients of nonlinear terms g_i are in order. While the evaluation of the derivatives $a_i'(t)$ is completed in $\mathcal{O}(N)$ operations, the use of the fast transforms above implies that the evaluation of the derivatives $b_i'(t)$, on the other hand, is completed in $\mathcal{O}(N\log N)$ operations. This, in turn, implies that the computational cost of the algorithm is $\mathcal{O}(N\log N)$ operations per time step. While this cost is not excessive, there have been efforts to reduce the cost of the evaluation of function products through convolution sums [28]. The reason why these algorithms cannot be easily applied in this case is that the viscosity function F is a function of $A(r, t)$ rather than simply $F = F(r)$.

To finalize our description of the time stepping, we note that the non-zero elements of the Chebyshev transform of equation (6.6) lead to the following formula for the evaluation of the time derivatives $c_i'(t)$:

$$c_i'(t) = -\frac{1}{\lambda_1}c_i(t) + h_i(t), \qquad i = 1, 2, 3, \ldots, N. \tag{6.83}$$

In a similar procedure used above to compute g_i, values for $h_i = H_{2i-1}$ in equation (6.83) are computed as follows:

(1) Populate the M-element array of spectral values $\hat{\mathbf{B}}(t) = \{\hat{B}_i(t)\}_{i=1}^{M}$ using

$$\hat{B}_{2i} = b_i, \qquad \hat{B}_{2i-1} = 0, \qquad i = 1, 2, \ldots, N. \tag{6.84}$$

(2) Obtain the array of spatial values $\mathbf{B}(t) = \{B(r_k, t)\}_{k=1}^{M}$ by means of a normalized fast M-point DCT-III:

$$\mathbf{B}(t) = \frac{1}{2}\mathrm{DCTIII}(\hat{\mathbf{B}}(t)). \tag{6.85}$$

(3) Populate the M-element array of spatial values $\mathbf{H}(t) = \{H(r_k, t)\}_{k=1}^{M}$ as the product of functions

$$H(r_k, t) = 2A(r_k, t)\left(\frac{r_k}{2}f(t) + B(r_k, t) - \frac{\lambda_2}{\lambda_1 \mathrm{Wo}}A(r_k, t)\right), \qquad k = 1, 2, \ldots, M. \tag{6.86}$$

Spatial values of $A(r_k, t)$ are retained from the calculation of g_i and re-used here.

(4) Obtain the array of spectral values $\hat{\mathbf{H}}(t) = \{\hat{H}_i(t)\}_{i=1}^{M}$ by means of a normalized fast M-point DCT-II:

$$\hat{\mathbf{H}}(t) = \frac{1}{M}\mathrm{DCTII}(\mathbf{H}(t)). \tag{6.87}$$

Values $h_i = \hat{H}_{2i-1}$ are then extracted for use in equation (6.83).

With the time stepping procedure now fully described, we now turn our attention to the efficient calculation of some flow related quantities of interest. These quantities (i.e. the physical velocity profile and the volumetric flow rate) are not necessary to advance the time level of the solution, so it's optional whether these are computed inside the main time loop, or left as a post-processing exercise after the time stepping is completed. Either way, the algorithms for their calculation rest on the manipulation of the spectral variables.

Spatial values of the *even* velocity profile are stored in the M-element array $\mathbf{W}(t) = \{W(r_k, t)\}_{k=1}^{M}$. In our code, these are obtained by evaluating a DCT-III for the corresponding spectral data:

$$\mathbf{W}(t) = \frac{1}{2}\mathrm{DCTIII}(\hat{\mathbf{W}}(t)) \tag{6.88}$$

where $\hat{\mathbf{W}}(t) = \{\hat{W}_i(t)\}_{i=1}^{M}$ with

$$\hat{W}_{2i} = 0, \qquad \hat{W}_{2i-1} = w_i, \qquad i = 1, 2, \ldots, N. \tag{6.89}$$

We compute the spectral coefficients of the velocity w_i from the coefficients a_i, which correspond to the r-derivative of the velocity, using the algorithm for the anti-derivative (5.28). We thus obtain

$$w_i = (a_{i-1} - a_i)/(4i - 4) \qquad i = 2, 3. \ldots, N. \tag{6.90}$$

The constant of integration is chosen in order to satisfy no-slip conditions, yielding,

$$w_1 = -2 \sum_{i=2}^{N} w_i. \tag{6.91}$$

The second physical quantity of interest we compute is the volumetric flow rate. In terms of the velocity introduced above, equation (3.58) can be rewritten to give the following expression for the non-dimensional flow rate:

$$Q(t) = 2\pi \int_0^1 W(r,t) r dr. \tag{6.92}$$

We compute this quantity without the use of cosine transforms. First, for the even function $W(r,t)$ in equations (6.88) and (6.89) we compute the non-zero Chebyshev coefficients of the product $rW(r,t)$ (resulting in an odd function) by means of the recurrence (5.59):

$$\alpha_i^{(3)} = (w_i + w_{i+1})/2 \qquad i = 1, 2. \ldots, N-1. \tag{6.93}$$

$$\alpha_N^{(3)} = w_N/2. \tag{6.94}$$

Next we compute the non-zero Chebyshev coefficients of the anti-derivative of $rW(r,t)$ (an *even* function in physical space) using the recurrence defined in equation (5.28):

$$\alpha_i^{(4)} = (\alpha_{i-1}^{(3)} - \alpha_i^{(3)})/(4i-4) \qquad i = 2, 3. \ldots, N. \tag{6.95}$$

At this point we are free to set the constant of integration to zero, i.e., $\alpha_1^{(4)} = 0$ but this value is not strictly used in the flowrate calculation below which evaluates the anti-derivative between limits 0 and 1. Indeed using identities $T_{2i}(0) = (-1)^i$ and $T_{2i}(1) = 1$ we obtain our algorithm for computing the flow rate:

$$Q = 2\pi \sum_{i=2}^{N} \alpha_i^{(4)} \left[1 + (-1)^i\right]. \tag{6.96}$$

6.6 Initial Conditions and Prescribed Pressure Gradient

As discussed in the previous section, the solver enforces the vanishing of all flow quantities at $t = 0$ through the conditions on the spectral coefficients in equation (6.58). By assumption, the pressure function $f(t)$ and all its derivatives, which drive the flow, should also vanish at $t = 0$. One has to realize that prescribing a non-zero pressure function $f(t) = \cos(t)$ for $t > 0$, for example, may introduce a discontinuity in the time variable of the solution at $t = 0$. Certainly, the choice $f(t) = \cos(t)$ actually implies that the pressure gradient behaves as a Heaviside function at $t = 0$, but the choice $f(t) = \sin(t)$ which is continuous at $t = 0$, also does have a discontinuity in the first derivative at that point. To make this issue a little more clear, in the cases discussed briefly above, our pressure function should more appropriately be defined as

$$f(t) = \begin{cases} 0 & t \leq 0 \\ \cos(t) & t > 0 \end{cases} \tag{6.97}$$

or

$$f(t) = \begin{cases} 0 & t \leq 0 \\ \sin(t) & t > 0 \end{cases}. \tag{6.98}$$

So defined, one can see that the left and right limits of $f(t)$ or its derivatives at $t = 0$ are not necessarily equal, and we expect these discontinuities to result in corresponding discontinuous derivatives in the solution.

While we will leave the theoretical analysis of the smoothness of the solution in a neighborhood of $t = 0$ for a later work, to remedy this issue a little we will ensure some additional smoothness in the solution in a neighborhood of $t = 0$ (and therefore the order of accuracy of the RK method applied) by means of a more carefully chosen form of the pressure function. In this thesis, we will adopt the following form of pressure gradient function

$$f(t) = \begin{cases} 0 & t \leq 0 \\ \left(1 - \mathrm{e}^{-\alpha t^2}\right) \tilde{f}(t) & t > 0 \end{cases} \tag{6.99}$$

where $\tilde{f}(t) = \cos(t)$ or $\tilde{f}(t) = \sin(t)$, etc. The term $(1 - \mathrm{e}^{-\alpha t^2})$ in equation (6.99) ensures that $f(t)$ smoothly transitions (at least for its first few derivatives!) from 0 to $\tilde{f}(t)$. We choose the decay constant α so that

$$\mathrm{e}^{-\alpha t^2} \leq \epsilon \qquad \text{for} \qquad t \geq 2\pi, \tag{6.100}$$

with ϵ another small parameter to be chosen. In our implementation we take $\epsilon = 1/100$ and hence

$$\alpha = -\frac{1}{4\pi^2} \ln \epsilon = \frac{\ln(10)}{2\pi^2} = 0.116650\ldots \tag{6.101}$$

This means that with α so chosen, $|f(t) - \tilde{f}(t)| \leq 1\%$ for $t \geq 2\pi$, with the difference between the functions decaying exponentially for $t > 2\pi$.

Using these tools, we can now define $f(t)$ applicable to flows driven by constant pressure gradient k as

$$f(t) = \begin{cases} 0 & t \leq 0 \\ k(1 - \mathrm{e}^{-\alpha t^2}) & t > 0 \end{cases} \tag{6.102}$$

Notice that we have left and right limits $f_-(0) = f_+(0)$, $f'_-(0) = f'_+(0)$ but $f''_-(0) = 0$ and $f''_+(0) = 2k\alpha$. That is, the smoothing term ensures that the pressure function (6.102) and its

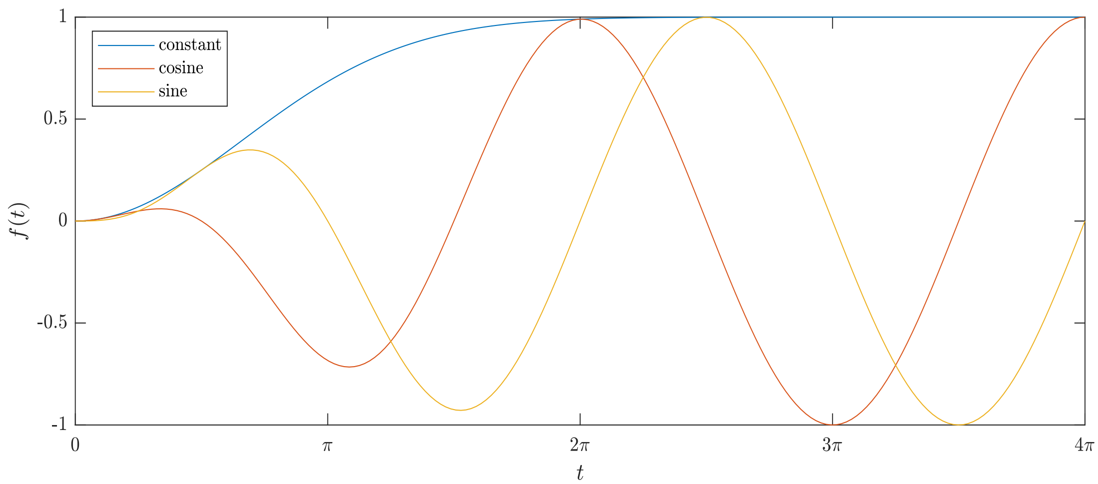

Figure 6.1: Pressure functions corresponding to (6.102), (6.103) and (6.104) labeled as 'constant', 'cosine' and 'sine', respectively, with $k = 1$.

first derivative are continuous at $t = 0$. We also define the $f(t)$ applicable to an oscillating cosine pressure gradient $k\cos(t)$ as

$$f(t) = \begin{cases} 0 & t \leq 0 \\ k(1 - \mathrm{e}^{-\alpha t^2})\cos(t) & t > 0 \end{cases} \tag{6.103}$$

In the same way as in the previous case, we can see that the smoothing term ensures that the pressure function (6.103) and its first derivative are continuous at $t = 0$ since $f_-(0) = f_+(0)$, $f'_-(0) = f'_+(0)$ but $f''_-(0) = 0$ and $f''_+(0) = 2k\alpha$. We also define the $f(t)$ applicable to an oscillating sine pressure gradient $k\sin(t)$ as

$$f(t) = \begin{cases} 0 & t \leq 0 \\ k(1 - \mathrm{e}^{-\alpha t^2})\sin(t) & t > 0 \end{cases} \tag{6.104}$$

In this case we can see that the smoothing term ensures that the pressure function (6.104) and its first two derivatives are continuous at $t = 0$ since $f_-(0) = f_+(0)$, $f'_-(0) = f'_+(0)$, $f''_-(0) = f''_+(0)$ but $f'''_-(0) = 0$ and $f'''_+(0) = 6k\alpha$.

6.7 Stability Considerations

Experimenting with the code a little, it quickly becomes obvious that the algorithm is not stable for an arbitrary choice of the time step Δt (we might naively chose this quantity to only satisfy an accuracy criteria for the solution). Fixing all other code parameters and documenting values of Δt above which the algorithm ceases to be stable readily points to the fact that it is subject to a diffusive-type stability constraint of the form

$$\frac{\Delta t}{(\Delta r)^2_{\mathrm{min}}} < \mathrm{const}, \tag{6.105}$$

where $(\Delta r)^2_{\mathrm{min}}$ is the smallest spacing between spatial sampling points on the interval $r \in (-1, 1)$. On the Chebyshev grid (6.11), this quantity is not constant, and indeed the smallest value of the spatial step occurs at the domain boundary:

$$(\Delta r)_{\mathrm{min}} = r_1 - r_2 = \cos\left(\frac{\Delta\theta}{2}\right) - \cos\left(\frac{3\Delta\theta}{2}\right) = 2\sin(\Delta\theta)\sin\left(\frac{\Delta\theta}{2}\right), \tag{6.106}$$

where the constant step size in the θ variable is given by equation (6.12). Taylor expansion of the expression (6.106) reveals the well-known quadratic relationship between the step size in the θ-variable and the minimum spatial step size:

$$(\Delta r)_{\mathrm{min}} = (\Delta\theta)^2 + \mathcal{O}(\Delta\theta)^4 \tag{6.107}$$

Conducting further numerical experiments with the code using different values of parameters λ_1, λ_2 and Wo indicates that the stability criteria (6.105) can be rewritten in the more useful form

$$\frac{\lambda_2(\Delta t)}{\lambda_1 \mathrm{Wo}(\Delta\theta)^4} < \mathrm{const.} \tag{6.108}$$

In what follows, experimenting with the code, we will document critical values of the stability parameter (6.108) below which the code is stable for different code parameters λ_1, λ_2 and Wo. Ultimately we will numerically deduce a stability boundary as a function of the number

N	$(N_t)_{\text{crit}}$	$\left.\frac{\lambda_2(\Delta t)}{\lambda_1 \text{Wo}(\Delta\theta)^4}\right\|_{\text{crit}}$
5	78	1.3961703217835280
10	2,350	0.73226131819382989
15	12,695	0.68598663124026027
20	41,400	0.66478198466139049
25	102,990	0.65240653599736154
30	216,270	0.64422838572066188
35	404,325	0.63839836512394343
40	694,505	0.63403659320601535
45	1,118,435	0.63065058649332273
50	1,712,015	0.62794530171675944
55	2,515,425	0.62573243534883694
60	3,573,110	0.62388974420392695
65	4,933,790	0.62233175824004017
70	6,650,460	0.62099721076183956
75	8,780,390	0.61984115232279757
80	11,385,125	0.61882990488704437

Table 6.1: Critical stability values obtained with parameters $\lambda_1 = 1$, $\lambda_2 = 1/2$, $\beta = 1$, $\text{Wo} = 30$ and $T_{\text{max}} = 10P = 20\pi$. The code is stable for all values of N_t greater than or equal to the critical values listed; similarly the code is stable for all values of $\frac{\lambda_2(\Delta t)}{\lambda_1 \text{Wo}(\Delta\theta)^4}$ less than or equal to the critical values listed. Oscillatory flow with pressure input (6.103).

of spatial points N.

Our first experiments deal with the physical case corresponding to $\lambda_1 = 1$, $\lambda_2 = 1/2$, $\beta = 1$, $\text{Wo} = 30$ and $T_{\text{max}} = 10P = 20\pi$. The non-linear terms do not contribute to the solution in this case as $\beta = 1$. Critical values of the number of time steps N_t for a fixed number of spatial sampling points N are documented in Table 6.1, as is the critical stability parameter resulting from these values. Inspecting the data, it quickly becomes obvious that the critical stability parameter is well approximated by a rational curve of the form

$$\left.\frac{\lambda_2(\Delta t)}{\lambda_1 \text{Wo}(\Delta\theta)^4}\right|_{\text{crit}} \sim \zeta_0 + \frac{\zeta_1}{N} + \frac{\zeta_2}{N^2} + \frac{\zeta_3}{N^3} + \dots. \tag{6.109}$$

Values of the parameters ζ_i can be deduced using the data in Table 6.1 by solving a linear system of equations. We did have concerns that the critical stability parameters in Table 6.1

N	$(N_t)_{\text{crit}}$	$\left.\frac{\lambda_2(\Delta t)}{\lambda_1 \text{Wo}(\Delta\theta)^4}\right\vert_{\text{crit}}$
5	76,340	1.4082594057733486
10	2,351,710	0.73141780570525794
15	12,696,615	0.68584539917208354
20	41,398,215	0.66479460642908184
25	102,987,910	0.65241344725070849

Table 6.2: Critical stability values obtained with parameters $\lambda_1 = 1$, $\lambda_2 = 1/2$, $\beta = 1$, $\text{Wo} = 30$ and $T_{\text{max}} = 10^4 P$. The code is stable for all values of N_t greater than or equal to the critical values listed; similarly the code is stable for all values of $\frac{\lambda_2(\Delta t)}{\lambda_1 \text{Wo}(\Delta\theta)^4}$ less than or equal to the critical values listed. Oscillatory flow with pressure input (6.103).

corresponding to smaller values of N were under-resolved simply due to the very small values of N_t required for stability in these cases. To illustrate this concern, for $N = 5$ in the first line of the table, choosing $N_t = 78$ or $N_t = 79$ results in over a 1% error in the calculation of $\frac{\lambda_2(\Delta t)}{\lambda_1 \text{Wo}(\Delta\theta)^4}$, or equivalently an error in the first decimal place. We therefore re-ran the experiments in these cases with all code values remaining the same as in the previous runs, except with a much larger final time T_{max}. The resulting data is documented in Table 6.2. Solving a system of linear equations for the five unknowns ζ_i, $i = 1, \ldots, 5$ using data corresponding to $N = 15, 20, 25$ in Table 6.2 and $N = 75, 80$ Table 6.1, for physical case with $\lambda_1 = 1$, $\lambda_2 = 1/2$, $\beta = 1$, $\text{Wo} = 30$ we obtain the following approximation for the stability boundary:

$$\begin{aligned}\left.\frac{\lambda_2(\Delta t)}{\lambda_1 \text{Wo}(\Delta\theta)^4}\right\vert_{\text{crit}} \sim\ & 0.6037086479694682 + \frac{1.205592726544756}{N} \\ + \ & \frac{0.3840072431250268}{N^2} - \frac{5.497460782120228}{N^3} \\ + \ & \frac{85.35785957251943}{N^4}. \end{aligned} \tag{6.110}$$

In order to get a sense of how changes in the code parameters impact the location of the stability boundary we next examine the results of numerical experiments dealing with the physical case corresponding to $\lambda_1 = 3/4$, $\lambda_2 = 2/5$, $\beta = 1$, $\text{Wo} = 15$ and $T_{\text{max}} = 7P = 14\pi$.

N	$(N_t)_{\text{crit}}$	$\left.\frac{\lambda_2(\Delta t)}{\lambda_1 \text{Wo}(\Delta\theta)^4}\right\vert_{\text{crit}}$
5	170	0.94994657633618496
10	3,525	0.72890338887997852
15	18,975	0.68534935614346149
20	61,835	0.66465841897028666
25	153,805	0.65237644746241652
30	322,975	0.64420386450753497
35	603,805	0.63838409870315116
40	1,037,140	0.63402862958363271
45	1,670,210	0.63064521467717460
50	2,556,625	0.62794126708039677
55	3,756,380	0.62573035422659351
60	5,335,855	0.62388843153641482
65	7,367,805	0.62233070860444795
70	9,931,365	0.62099646708485545
75	13,112,065	0.61984037579181095
80	17,001,810	0.61882903764674857

Table 6.3: Critical stability values obtained with parameters $\lambda_1 = 3/4$, $\lambda_2 = 2/5$, $\beta = 1$, $\text{Wo} = 15$ and $T_{\text{max}} = 7P = 14\pi$. The code is stable for all values of N_t greater than or equal to the critical values listed; similarly the code is stable for all values of $\frac{\lambda_2(\Delta t)}{\lambda_1 \text{Wo}(\Delta\theta)^4}$ less than or equal to the critical values listed. Oscillatory flow with pressure input (6.103).

N	$(N_t)_{\text{crit}}$	$\left.\frac{\lambda_2(\Delta t)}{\lambda_1 \text{Wo}(\Delta\theta)^4}\right\|_{\text{crit}}$
5	242,780	0.94466261438718968
10	5,039,435	0.72815874118659363
15	27,108,040	0.68529058238122320
20	88,338,040	0.66463017912053413
25	219,729,365	0.65234864574787632

Table 6.4: Critical stability values obtained with parameters $\lambda_1 = 3/4$, $\lambda_2 = 2/5$, $\beta = 1$, $\text{Wo} = 15$ and $T_{\text{max}} = 10^4 P$. The code is stable for all values of N_t greater than or equal to the critical values listed; similarly the code is stable for all values of $\frac{\lambda_2(\Delta t)}{\lambda_1 \text{Wo}(\Delta\theta)^4}$ less than or equal to the critical values listed. Oscillatory flow with pressure input (6.103).

Again, in this case, the non-linear terms do not contribute to the solution since $\beta = 1$. Critical values of the number of time steps N_t for a fixed number of spatial sampling points N are documented in Table 6.3, as is the critical stability parameter resulting from these values. Again suspicious that the critical stability parameters in Table 6.3 corresponding to smaller values of N were under-resolved, we re-ran the experiments with all code values remaining the same as in the previous runs, except with a much larger final time T_{max}; the resulting data is documented in Table 6.4. Solving a system of linear equations for the five unknowns ζ_i, $i = 1, \ldots, 5$ using data corresponding to $N = 15, 20, 25$ in Table 6.4 and $N = 75, 80$ Table 6.3, for physical case with $\lambda_1 = 3/4$, $\lambda_2 = 2/5$, $\beta = 1$, $\text{Wo} = 15$ we obtain the following approximation for the stability boundary:

$$\begin{aligned}
\left.\frac{\lambda_2(\Delta t)}{\lambda_1 \text{Wo}(\Delta\theta)^4}\right|_{\text{crit}} &\sim 0.6036960639728150 + \frac{1.207497066075241}{N} \\
&+ \frac{0.2845840962629897}{N^2} - \frac{3.148043646923103}{N^3} \\
&+ \frac{38.60912946640193}{N^4}
\end{aligned} \tag{6.111}$$

In a preliminary comparison between the stability boundaries in equation (6.110) and equation (6.111), it appears that the dominant terms ζ_0 and ζ_1 are either independent of the parameters λ_1, λ_2 and Wo or very weakly dependent on these values.

Finally, in order to get a sense of how changes in the code parameters (especially the inclusion of the non-linear terms) impact the location of the stability boundary we examine the results of numerical experiments dealing with the physical case corresponding to $\lambda_1 = 1$, $\lambda_2 = 1/2$, $\beta = 1/10$, Wo $= 30$ and $T_{\text{max}} = 10P = 20\pi$. For these cases, we use the Powell-Eyring viscosity model with $\Lambda = 10$. Critical values of the number of time steps N_t for a fixed number of spatial sampling points N are documented in Table 6.5, as is the critical stability parameter resulting from these values. Assuming that the critical stability parameters in Table 6.5 corresponding to smaller values of N were under-resolved, we re-ran the experiments with all code values remaining the same as in the previous runs, except with a much larger final time T_{max}; the resulting data is documented in Table 6.6. Solving a system of linear equations for the five unknowns ζ_i, $i = 1, \ldots, 5$ using data corresponding to $N = 15, 20, 25$ in Table 6.6 and $N = 75, 80$ Table 6.5, for physical case with $\lambda_1 = 1$, $\lambda_2 = 1/2$, $\beta = 1/10$ (Powell-Eyring model with $\Lambda = 10$), Wo $= 30$ we obtain the following approximation for the stability boundary:

$$\begin{aligned} \left.\frac{\lambda_2(\Delta t)}{\lambda_1 \mathrm{Wo}(\Delta\theta)^4}\right|_{\text{crit}} &\sim 0.6036925279535342 + \frac{1.208307949592186}{N} \\ &+ \frac{0.2165885172282228}{N^2} - \frac{0.6118535585091607}{N^3} \\ &- \frac{64.11458246119600}{N^4} \end{aligned} \tag{6.112}$$

In comparing the three stability boundaries, it seems clear that the values of ζ_i for $i \geq 2$ are strongly dependent on the code parameters, but values ζ_0 and ζ_1 are either independent of these parameters or very weakly dependent on them. Further numerical experiments coupled with a theoretical analysis will shed further light on this issue, but based on our numerical studies in this section, we are prepared to present what we think is a general stability boundary of the algorithm as follows:

$$\left.\frac{\lambda_2(\Delta t)}{\lambda_1 \mathrm{Wo}(\Delta\theta)^4}\right|_{\text{crit}} \sim 0.6037 + \frac{1.21}{N} \tag{6.113}$$

In the simplest terms, the stability restriction can be reduced further to simply state that

N	$(N_t)_{\text{crit}}$	$\left.\frac{\lambda_2(\Delta t)}{\lambda_1 \text{Wo}(\Delta\theta)^4}\right\vert_{\text{crit}}$
5	145	0.74656329706480318
10	2,390	0.72000076870544427
15	12,735	0.68383181223212375
20	41,435	0.66422043208468651
25	103,025	0.65218489610025099
30	216,310	0.64410925459144941
35	404,360	0.63834310743763167
40	694,540	0.63400464211217866
45	1,118,475	0.63062803252831345
50	1,712,055	0.62793063056031884
55	2,515,465	0.62572248517765028
60	3,573,145	0.62388363301975769
65	4,933,825	0.62232734348760110
70	6,650,495	0.62099394259824492
75	8,780,430	0.61983832858308130
80	11,385,170	0.61882745895534863

Table 6.5: Critical stability values obtained with parameters $\lambda_1 = 1$, $\lambda_2 = 1/2$, $\beta = 1/10$, $\text{Wo} = 30$ and $T_{\text{max}} = 10P = 20\pi$. Powell-Eyring model with $\Lambda = 10$. The code is stable for all values of N_t greater than or equal to the critical values listed; similarly the code is stable for all values of $\frac{\lambda_2(\Delta t)}{\lambda_1 \text{Wo}(\Delta\theta)^4}$ less than or equal to the critical values listed. Oscillatory flow with pressure input (6.103).

N	$(N_t)_{\text{crit}}$	$\left.\frac{\lambda_2(\Delta t)}{\lambda_1 \text{Wo}(\Delta\theta)^4}\right\vert_{\text{crit}}$
5	144,730	0.74280285759821219
10	2,390,620	0.71951316225517592
15	12,735,315	0.68376125606042104
20	41,437,010	0.66417219889101797
25	103,026,655	0.65216809560594158

Table 6.6: Critical stability values obtained with parameters $\lambda_1 = 1$, $\lambda_2 = 1/2$, $\beta = 1/10$, $\text{Wo} = 30$ and $T_{\text{max}} = 10^4 P$. Powell-Eyring model with $\Lambda = 10$. The code is stable for all values of N_t greater than or equal to the critical values listed; similarly the code is stable for all values of $\frac{\lambda_2(\Delta t)}{\lambda_1 \text{Wo}(\Delta\theta)^4}$ less than or equal to the critical values listed. Oscillatory flow with pressure input (6.103).

the code is stable in all cases provided

$$\frac{\lambda_2(\Delta t)}{\lambda_1 \mathrm{Wo}(\Delta\theta)^4} < 0.6037. \tag{6.114}$$

Chapter 7

Results and Discussion

In Chapter 6 of this thesis we developed a fast algorithm for computing numerical solutions of the equations of motion of a viscous fluid subject to the Generalized Oldroy-B stress model corresponding to the flow of a viscoelastic fluid with a shear rate dependent viscosity function. In this chapter we examine in detail the results of our code for different viscosity models (Powell-Eyring, Yeleswarapu and Adjusted Carreau) over a range of the parameters when the flow is driven by a pressure gradient function $f(t)$ which is a simple harmonic function of time. Our goal in this numerical study is to document steady state periodic solutions of the problem. To do this, we evolve the system, which is initially at a state of rest, over several periods of the input pressure gradient function (we denote this initial evolution time, before which the solution is not in steady state, as T). Our presumption in this approach is that any transient behaviour of the system will decay over time, leaving only the steady state solutions for $t > T$.

Our primary case of study corresponds to a low Womersley number flow with parameters arising in a typical blood flow sourced from the literature; see Chapter 3. In particular, for this case, we use

$$\begin{gathered} \mathrm{Wo} = 0.2365, \qquad \beta = 0.0616, \\ \lambda_1 = 1.923, \qquad \lambda_2 = 0.127, \quad \text{and} \quad \Lambda = 140. \end{gathered} \tag{7.1}$$

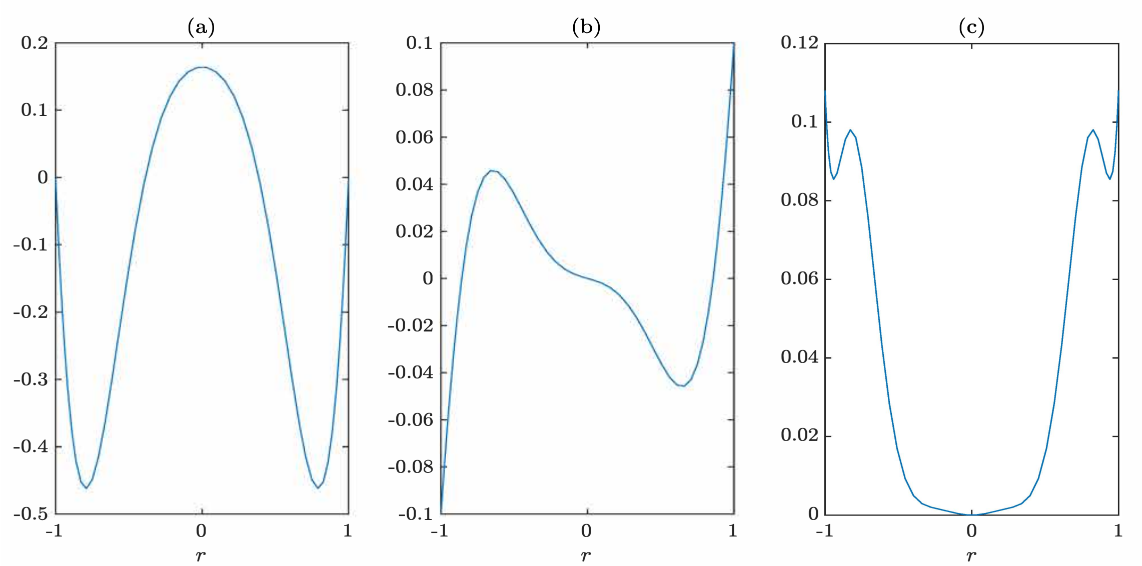

Figure 7.1: Exact solutions with parameters $\lambda_1 = 1$, $\lambda_2 = 1/2$, $\beta = 1$, Wo $= 30$ and $f(t) = \cos(t)$. The velocity profile $u_z(r,t)$ and stress profiles $S_{rz}(r,t)$ and $S_{zz}(r,t)$ are plotted in figures (a), (b) and (c), respectively, at $t = 40\pi$ using $M = 50$ points.

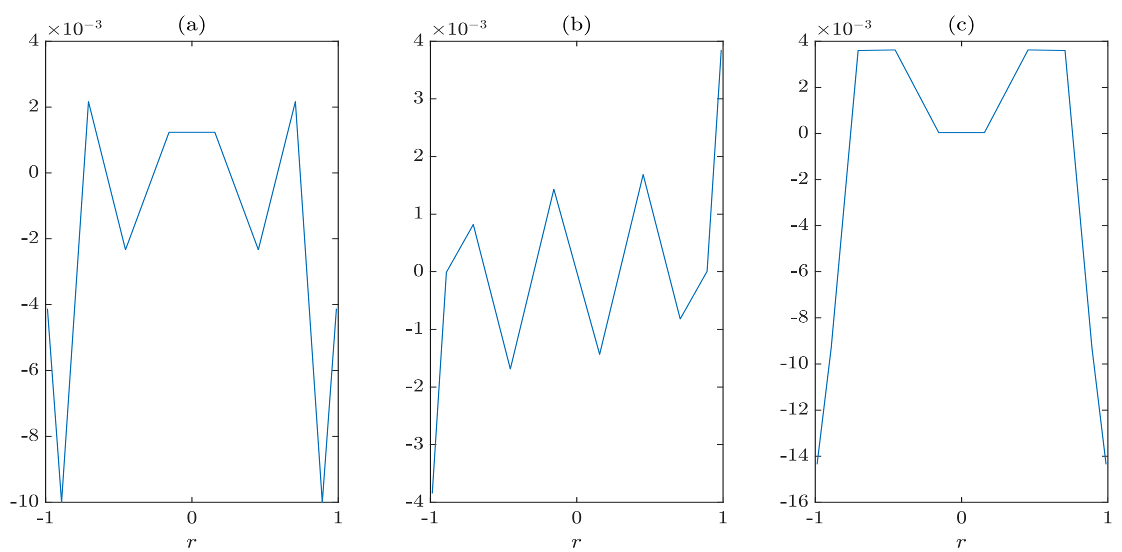

Figure 7.2: Absolute error of computed solutions with parameters $\lambda_1 = 1$, $\lambda_2 = 1/2$, $\beta = 1$, Wo $= 30$ and $f(t) = \cos(t)$. The absolute error of the velocity profile $u_z(r,t)$ and stress profiles $S_{rz}(r,t)$ and $S_{zz}(r,t)$ are plotted in figures (a), (b) and (c), respectively, at $t = 40\pi$ using $M = 10$ points.

To get some sense for the dependence of the solutions on the parameters, we will introduce small variations in these one at a time separately and present the corresponding solutions, and noting changes that arise. Given the physical significance of the parameters, most of our efforts will be spent here. Still, we will also present a limited set of solutions corresponding to moderate and high Womersley numbers so that the behaviour of the system can be more completely documented.

Before presenting a set of numerical results, we first establish the validity of the code by testing the numerical results against cases with known exact solutions; see Chapter 4.

7.1 Code Validation

In what follows we compare the results of our code against evaluations of exact solutions for viscosity ratio $\beta = 1$, a case which corresponds to the standard Oldroyd-B stress model (2.24). In fact, we use the mathematically equivalent case with $\beta = 1/2$ and $F = 1$, since this later case represents a better test of our code as it uses all subroutines, in particular those needed for the (usually nonlinear) viscosity function calculation. The parameters used for this comparison are as follows:

$$\mathrm{Wo} = 30, \qquad \beta = 1, \qquad \lambda_1 = 1, \qquad \lambda_2 = 1/2. \tag{7.2}$$

The velocity profile $u_z(r,t)$ and stress profiles $S_{rz}(r,t)$ and $S_{zz}(r,t)$ are plotted in Figure 7.1. The pressure gradient input is taken as $f(t) = \cos(t)$ evaluated at $t = 40\pi$. Solution values are computed in Matlab on the Chebyshev grid (6.11) with $M = 50$ (i.e. $N = 25$) using the real part of expressions (4.27), (4.17), and (4.35). The principal square root of $\sqrt{-i\psi}$ is assumed in our computations. Note that the velocity $u_z(r,t)$ and shear stress $S_{rz}(r,t)$ are 2π-periodic functions, while the normal stress $S_{zz}(r,t)$ is a π-periodic function of time. We will use this basic case in order to compute absolute errors with numerical solutions corresponding to various r-grid refinements, demonstrating the rapid convergence of the algorithm in the grid spacing.

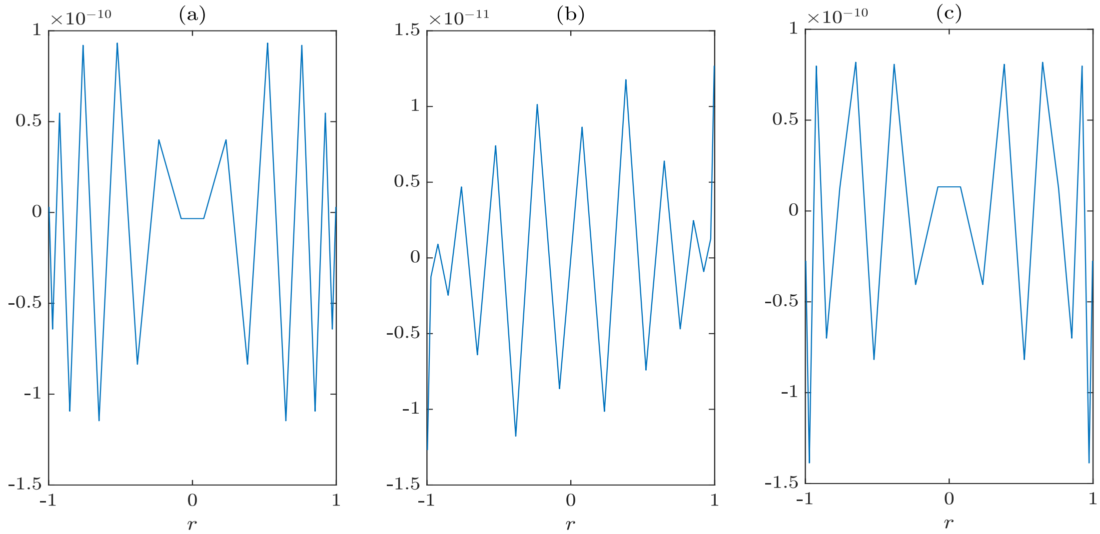

Figure 7.3: Absolute error of computed solutions with parameters $\lambda_1 = 1$, $\lambda_2 = 1/2$, $\beta = 1$, Wo $= 30$ and $f(t) = \cos(t)$. The absolute error of the velocity profile $u_z(r, t)$ and stress profiles $S_{rz}(r, t)$ and $S_{zz}(r, t)$ are plotted in figures (a), (b) and (c), respectively, at $t = 40\pi$ using $M = 20$ points.

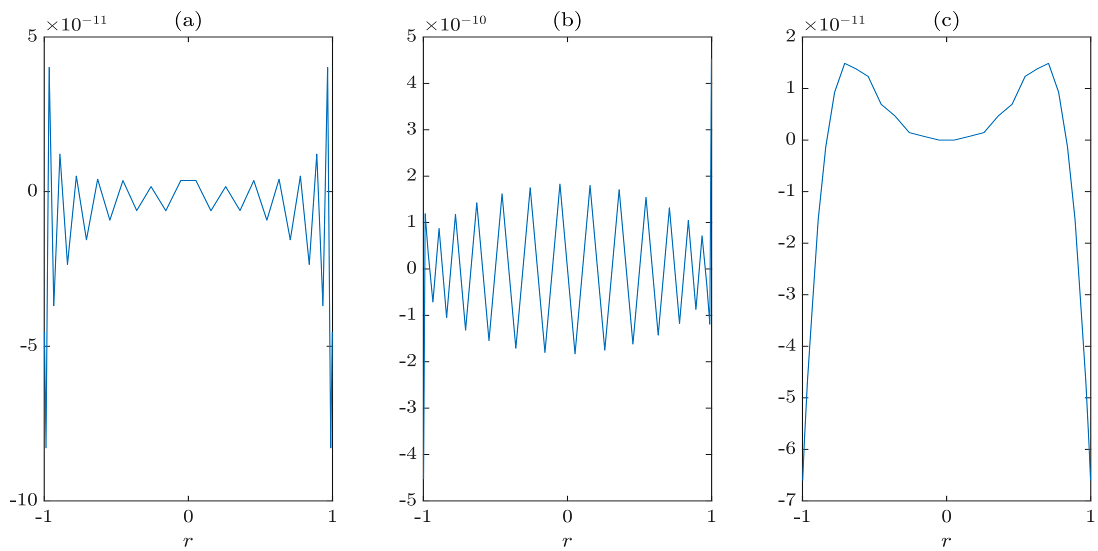

Figure 7.4: Absolute error of computed solutions with parameters $\lambda_1 = 1$, $\lambda_2 = 1/2$, $\beta = 1$, Wo $= 30$ and $f(t) = \cos(t)$. The absolute error of the velocity profile $u_z(r, t)$ and stress profiles $S_{rz}(r, t)$ and $S_{zz}(r, t)$ are plotted in figures (a), (b) and (c), respectively, at $t = 40\pi$ using $M = 30$ points.

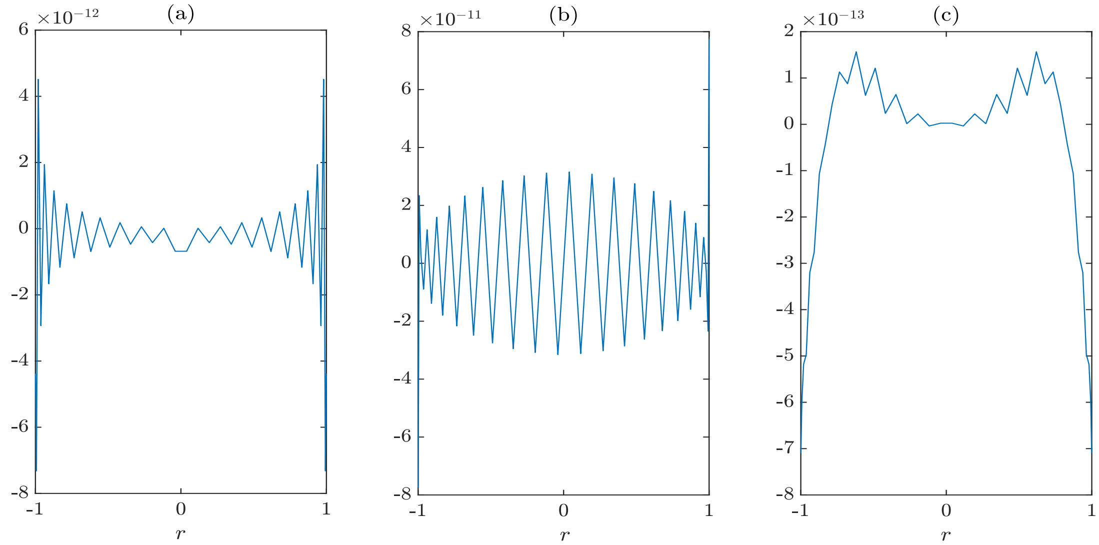

Figure 7.5: Absolute error of computed solutions with parameters $\lambda_1 = 1$, $\lambda_2 = 1/2$, $\beta = 1$, $\mathrm{Wo} = 30$ and $f(t) = \cos(t)$. The absolute error of the velocity profile $u_z(r,t)$ and stress profiles $S_{rz}(r,t)$ and $S_{zz}(r,t)$ are plotted in figures (a), (b) and (c), respectively, at $t = 40\pi$ using $M = 40$ points.

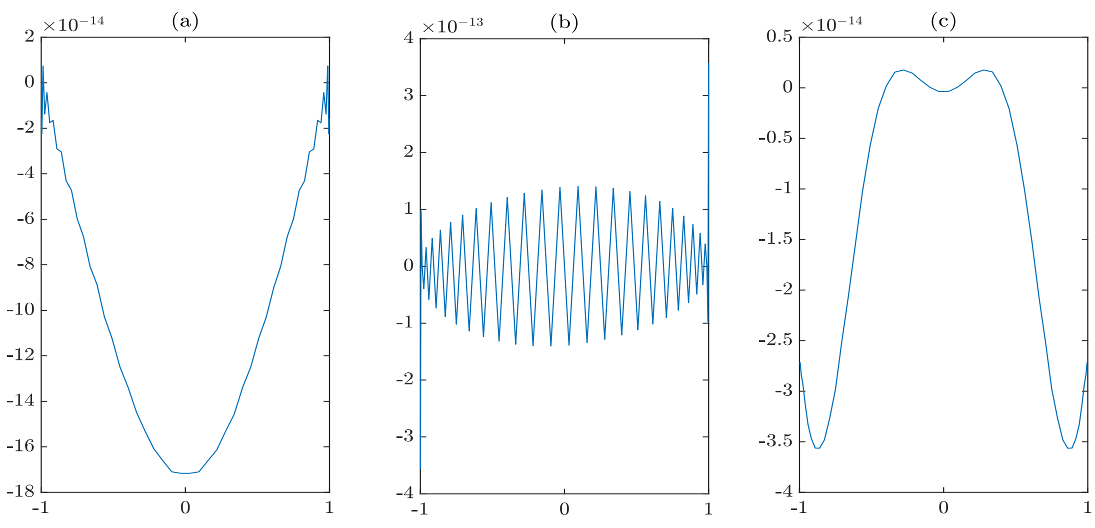

Figure 7.6: Absolute error of computed solutions with parameters $\lambda_1 = 1$, $\lambda_2 = 1/2$, $\beta = 1$, $\mathrm{Wo} = 30$ and $f(t) = \cos(t)$. The absolute error of the velocity profile $u_z(r,t)$ and stress profiles $S_{rz}(r,t)$ and $S_{zz}(r,t)$ are plotted in figures (a), (b) and (c), respectively, at $t = 40\pi$ using $M = 50$ points.

The absolute error of the velocity and stress profiles using $N = 5$ or equivalently $M = 10$ are plotted in Figure 7.2. Even with this very course grid, the numerical solutions all have absolute errors of order $\mathcal{O}(10^{-3})$. The same comparison is conducted in Figure 7.3, Figure 7.4, Figure 7.5 and Figure 7.6 for Chebyshev grids corresponding to $N = 10$, $N = 15$, $N = 20$ and $N = 25$, respectively; relative errors are $\mathcal{O}(10^{-10})$, $\mathcal{O}(10^{-10})$, $\mathcal{O}(10^{-11})$ and $\mathcal{O}(10^{-13})$, respectively. Clearly the solution experiences extremely rapid convergence between $N = 5$ and $N = 10$; convergence is slow thereafter but reaches double-precision accuracies.

7.2 Low Womersley Number Problems

We now turn our attention to the main topic of this chapter, i.e., the behaviour of the numerical solutions with code parameters defined as in (7.1). These are the solutions which should most closely resemble measurements of blood flow. Solutions of the problem over one period with start time $T = 16\pi$ using the Powell-Eyring viscosity model (2.14), the Yeleswarapu model (2.17) and the Carreau model (2.23) are depicted in Figure 7.7, Figure 7.8, and Figure 7.9, respectively. We note from the figures that all solutions are in a single-harmonic steady state flow by $T = 16\pi$ and that all solutions are well-approximated by low-order polynomials. In their fully-developed state, the velocity $u_z(r,t)$ and shear stress $S_{rz}(r,t)$ are 2π-periodic functions, while the normal stress $S_{zz}(r,t)$ is a π-periodic function of time. Note in particular the flattening of the velocity profiles towards the centreline of the tubes, which is characteristic of blood flows. Clearly there are only very small differences between results corresponding to different viscosity models, but we do note that the Carreau model predicts a S_{zz} stress that is about 20 % higher than the other models on the tube wall, but is qualitatively similar to the other cases of viscous stress model.

To get some sense for how the solutions behave for a small change in the Womersley number, we set $\mathrm{Wo} = 1$ with other parameters fixed as per equation (7.1). Solutions of the problem over one period beginning at time $T = 16\pi$ using the Powell-Eyring viscosity model (2.14), the Yeleswarapu model (2.17) and the Carreau model (2.23) are depicted in

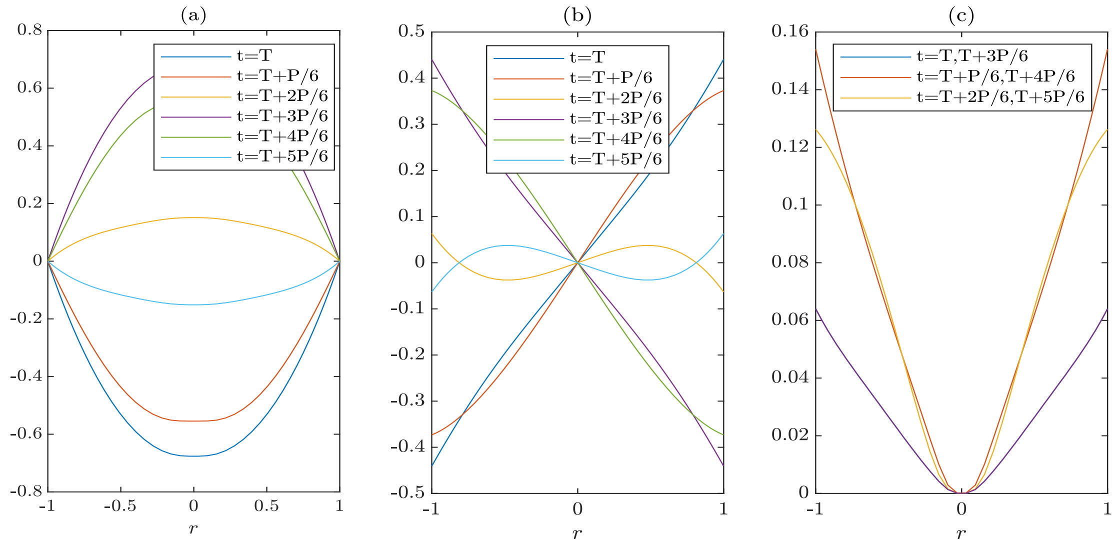

Figure 7.7: Computed solutions with parameters $\lambda_1 = 1.923$, $\lambda_2 = 0.127$, $\beta = 0.0616$, $\mathrm{Wo} = 0.2365$ with cosine pressure gradient (6.103) and Powell-Eyring viscosity model (2.14) with $\Lambda = 140$. The velocity profile $u_z(r,t)$ and stress profiles $S_{rz}(r,t)$ and $S_{zz}(r,t)$ are plotted in figures (a), (b) and (c), respectively, over one period with $T = 16\pi$ using $N = 25$ points.

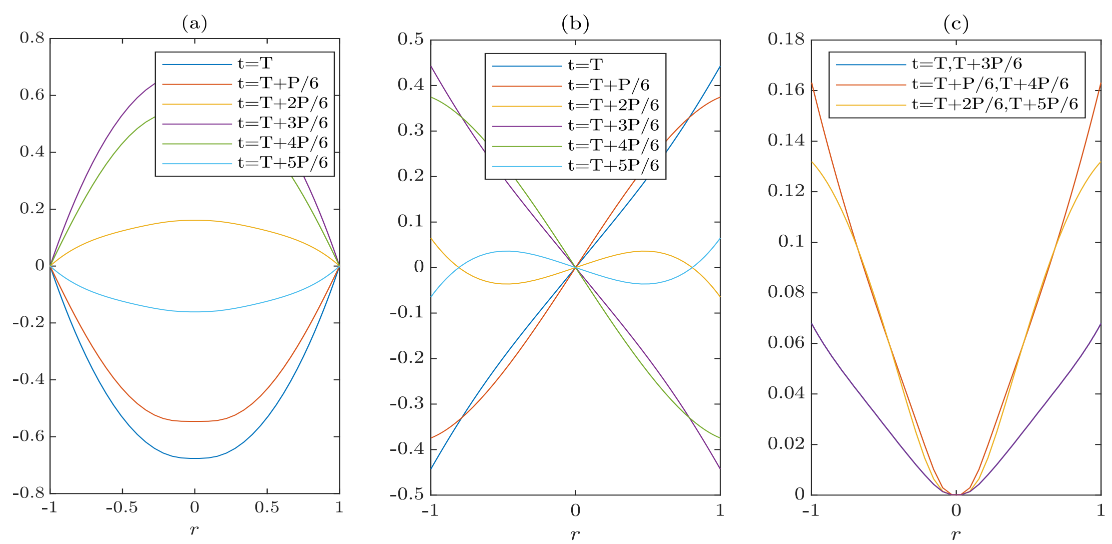

Figure 7.8: Computed solutions with parameters $\lambda_1 = 1.923$, $\lambda_2 = 0.127$, $\beta = 0.0616$, $\mathrm{Wo} = 0.2365$ with cosine pressure gradient (6.103) and Yeleswarapu viscosity model (2.17) with $\Lambda = 140$. The velocity profile $u_z(r,t)$ and stress profiles $S_{rz}(r,t)$ and $S_{zz}(r,t)$ are plotted in figures (a), (b) and (c), respectively, over one period with $T = 16\pi$ using $N = 25$ points.

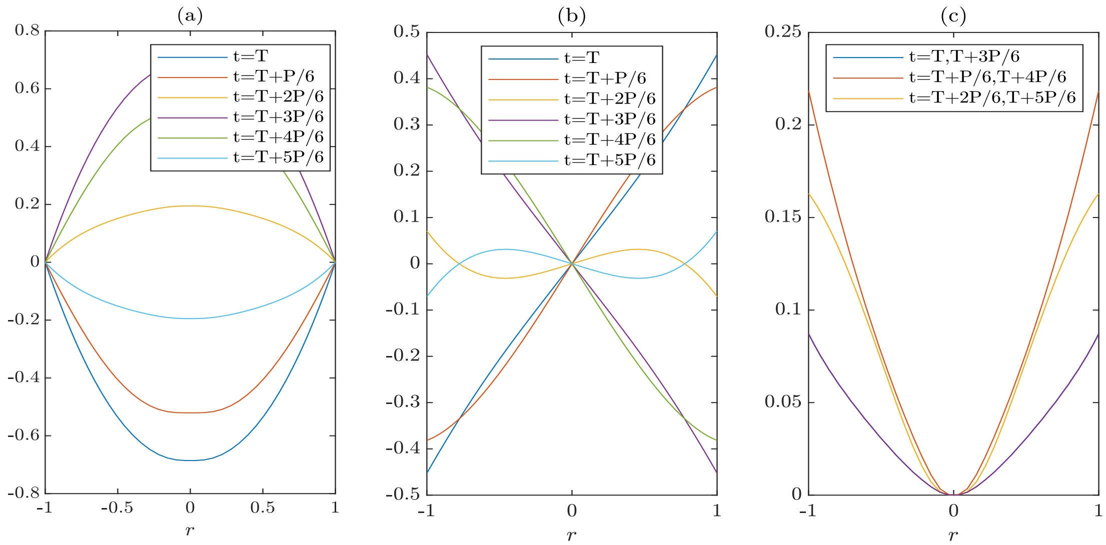

Figure 7.9: Computed solutions with parameters $\lambda_1 = 1.923$, $\lambda_2 = 0.127$, $\beta = 0.0616$, $\mathrm{Wo} = 0.2365$ with cosine pressure gradient (6.103) and Carreau viscosity model (2.23) with $\Lambda = 140$. The velocity profile $u_z(r,t)$ and stress profiles $S_{rz}(r,t)$ and $S_{zz}(r,t)$ are plotted in figures (a), (b) and (c), respectively, over one period with $T = 16\pi$ using $N = 25$ points.

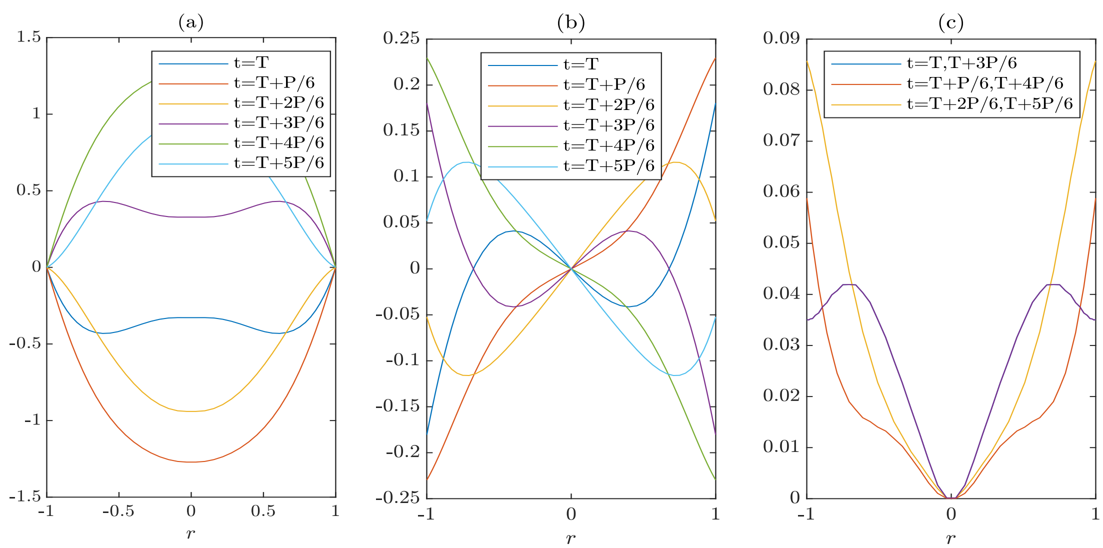

Figure 7.10: Computed solutions with parameters $\lambda_1 = 1.923$, $\lambda_2 = 0.127$, $\beta = 0.0616$, $\mathrm{Wo} = 1.0$ with cosine pressure gradient (6.103) and Powell-Eyring viscosity model (2.14) with $\Lambda = 140$. The velocity profile $u_z(r,t)$ and stress profiles $S_{rz}(r,t)$ and $S_{zz}(r,t)$ are plotted in figures (a), (b) and (c), respectively, over one period with $T = 16\pi$ using $N = 25$ points.

Figure 7.10, Figure 7.11, and Figure 7.12, respectively. We can see that the main effect of this increase in Womersley number is to increase the amplitude of the velocity profile and decrease the amplitudes of the stress profiles. The velocity $u_z(r,t)$ and shear stress $S_{rz}(r,t)$ are 2π-periodic functions, while the normal stress $S_{zz}(r,t)$ is a π-periodic function of time. The Carreau model predicts a S_{zz} stress that is nearly 50 % higher than the other models on the tube wall, but is qualitatively similar to the other cases.

To get some sense for how the solutions behave for a small change in the shear thinning parameter, we set $\Lambda = 70$ with other parameters fixed as per equation (7.1). Solutions of the problem over one period beginning at time $T = 16\pi$ using the Powell-Eyring viscosity model (2.14), the Yeleswarapu model (2.17) and the Carreau model (2.23) are depicted in Figure 7.13, Figure 7.14, and Figure 7.15, respectively. We can see that the main effect of this increase in shear thinning parameter Λ is to increase the amplitude of the S_{zz} stress by nearly 100 % but with only small changes to the other flow quantities. The velocity $u_z(r,t)$ and shear stress $S_{rz}(r,t)$ are 2π-periodic functions, while the normal stress $S_{zz}(r,t)$ is a π-periodic function of time. The Carreau model predicts a S_{zz} stress that is nearly 12 % higher than the other models on the tube wall, but is qualitatively similar to the other cases.

Next, to get some sense for how the solutions behave for a change in the viscosity ratio, we set $\beta = 0.2$ with other parameters fixed as per equation (7.1). Solutions of the problem over one period with start time $T = 16\pi$ using the are depicted in Figure 7.16, Figure 7.17, and Figure 7.18, respectively. We can see that the main effect of this increase in the viscosity ratio β is to slightly decrease the amplitude of the velocity $u_z(r,t)$, slightly increase the amplitude of the shear stress S_{rz}, but to significantly increase the amplitude of the normal stress S_{zz} by a factor of nearly 300 %. The velocity $u_z(r,t)$ and shear stress $S_{rz}(r,t)$ are 2π-periodic functions, while the normal stress $S_{zz}(r,t)$ is a π-periodic function of time. The Carreau model predicts a S_{zz} stress that is in line with the other models on the tube wall, and is qualitatively similar to the other cases.

Finally, to get some sense for how the solutions behave for a change in the relaxation time λ_1, we set $\lambda_2 = 0.5$ with other parameters fixed as per equation (7.1). Solutions of

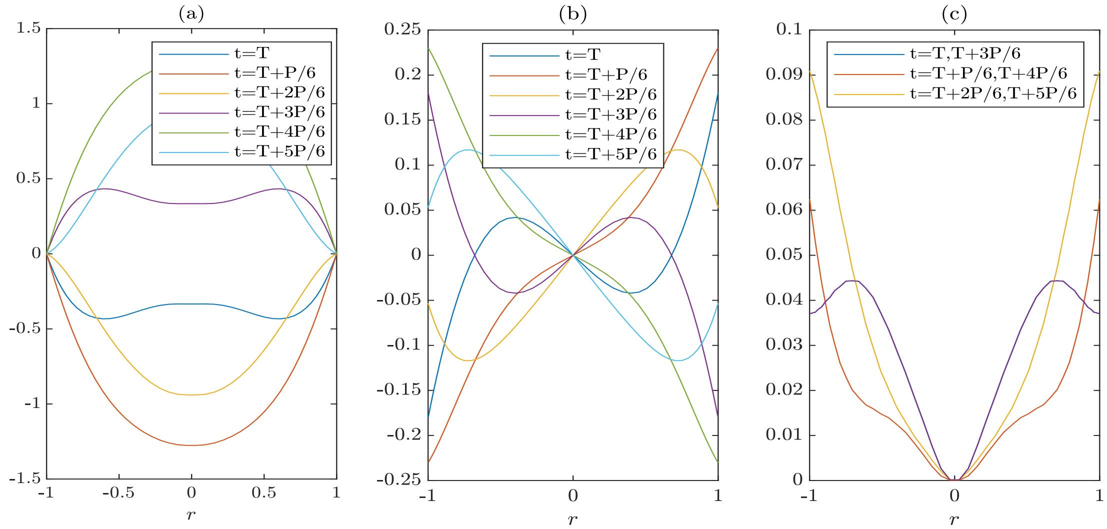

Figure 7.11: Computed solutions with parameters $\lambda_1 = 1.923$, $\lambda_2 = 0.127$, $\beta = 0.0616$, $\mathrm{Wo} = 1.0$ with cosine pressure gradient (6.103) and Yeleswarapu viscosity model (2.17) with $\Lambda = 140$. The velocity profile $u_z(r,t)$ and stress profiles $S_{rz}(r,t)$ and $S_{zz}(r,t)$ are plotted in figures (a), (b) and (c), respectively, over one period with $T = 16\pi$ using $N = 25$ points.

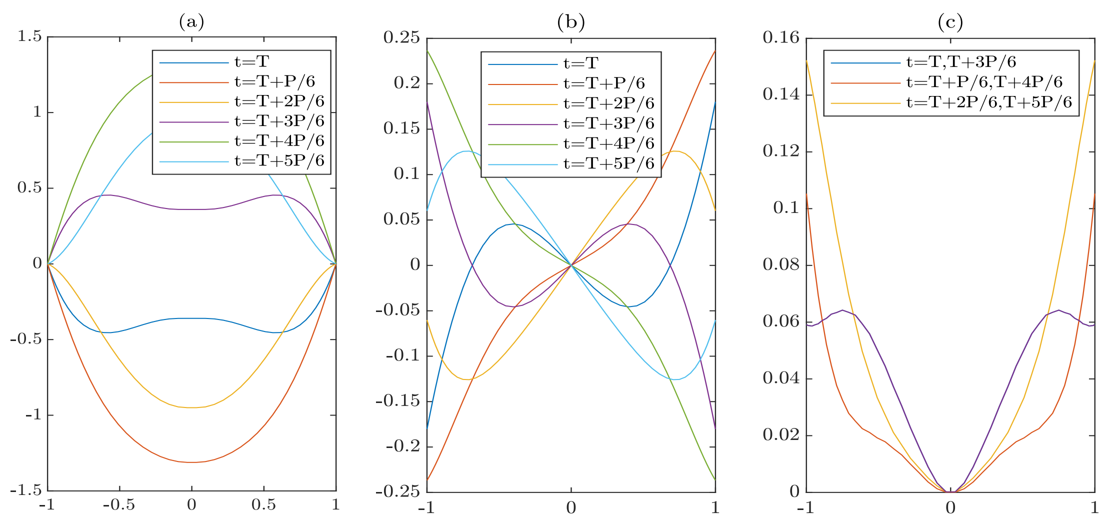

Figure 7.12: Computed solutions with parameters $\lambda_1 = 1.923$, $\lambda_2 = 0.127$, $\beta = 0.0616$, $\mathrm{Wo} = 1.0$ with cosine pressure gradient (6.103) and Carreau viscosity model (2.23) with $\Lambda = 140$. The velocity profile $u_z(r,t)$ and stress profiles $S_{rz}(r,t)$ and $S_{zz}(r,t)$ are plotted in figures (a), (b) and (c), respectively, over one period with $T = 16\pi$ using $N = 25$ points.

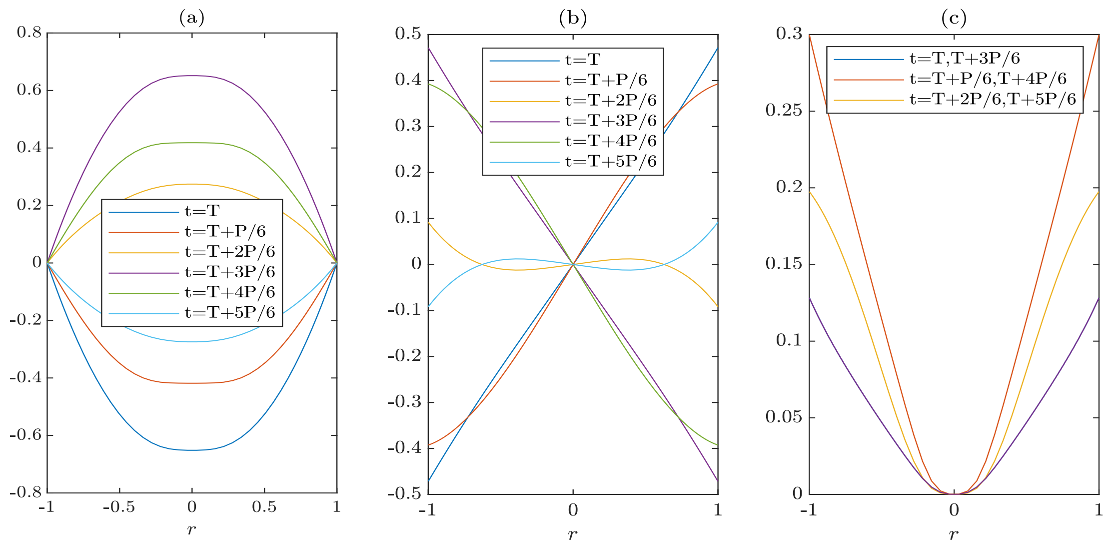

Figure 7.13: Computed solutions with parameters $\lambda_1 = 1.923$, $\lambda_2 = 0.127$, $\beta = 0.0616$, $\mathrm{Wo} = 0.2365$ with cosine pressure gradient (6.103) and Powell-Eyring viscosity model (2.14) with $\Lambda = 70$. The velocity profile $u_z(r,t)$ and stress profiles $S_{rz}(r,t)$ and $S_{zz}(r,t)$ are plotted in figures (a), (b) and (c), respectively, over one period with $T = 16\pi$ using $N = 25$ points.

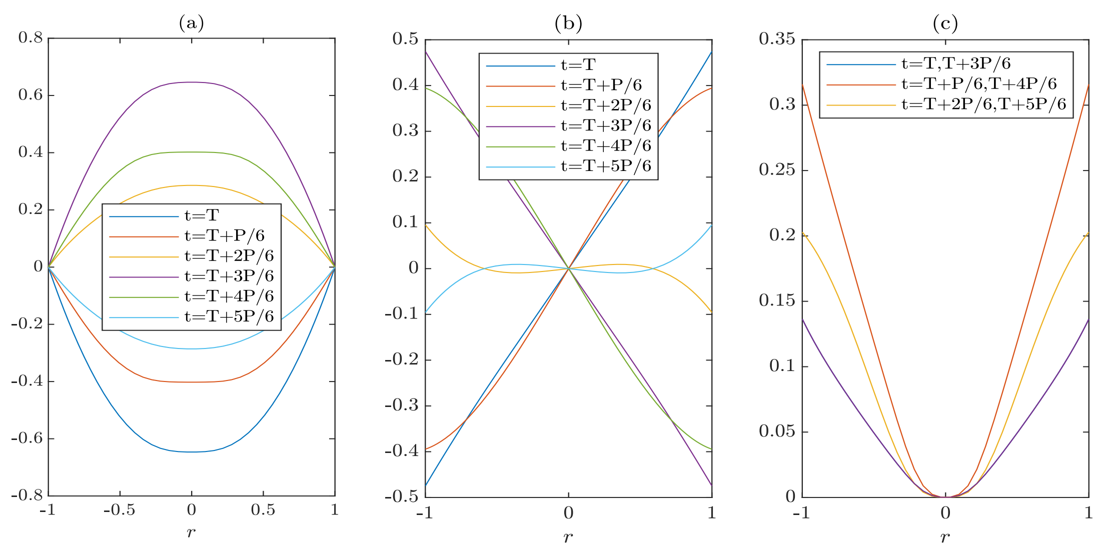

Figure 7.14: Computed solutions with parameters $\lambda_1 = 1.923$, $\lambda_2 = 0.127$, $\beta = 0.0616$, $\mathrm{Wo} = 0.2365$ with cosine pressure gradient (6.103) and Yeleswarapu viscosity model (2.17) with $\Lambda = 70$. The velocity profile $u_z(r,t)$ and stress profiles $S_{rz}(r,t)$ and $S_{zz}(r,t)$ are plotted in figures (a), (b) and (c), respectively, over one period with $T = 16\pi$ using $N = 25$ points.

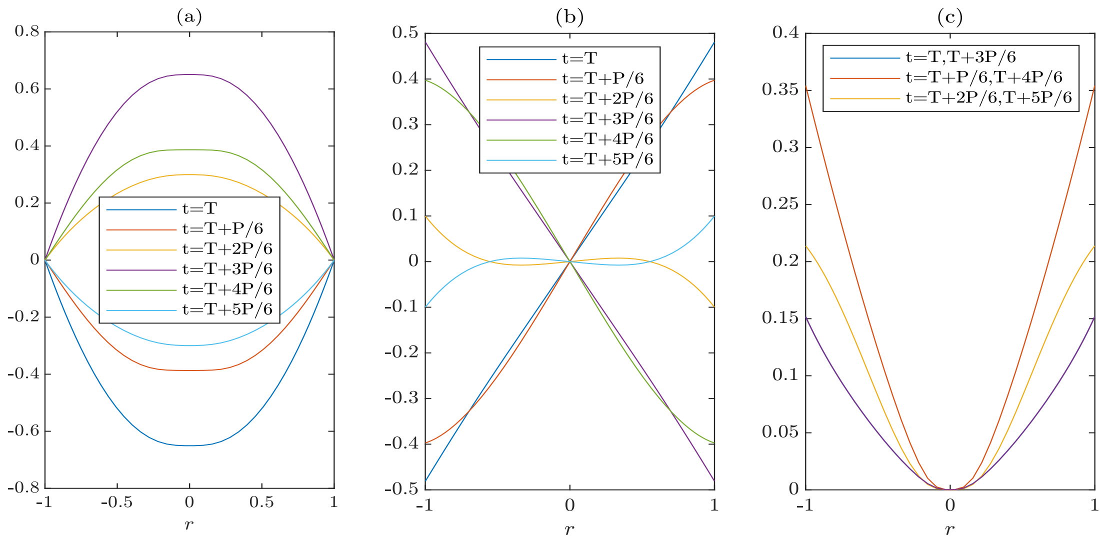

Figure 7.15: Computed solutions with parameters $\lambda_1 = 1.923$, $\lambda_2 = 0.127$, $\beta = 0.0616$, $\mathrm{Wo} = 0.2365$ with cosine pressure gradient (6.103) and Carreau viscosity model (2.23) with $\Lambda = 70$. The velocity profile $u_z(r,t)$ and stress profiles $S_{rz}(r,t)$ and $S_{zz}(r,t)$ are plotted in figures (a), (b) and (c), respectively, over one period with $T = 16\pi$ using $N = 25$ points.

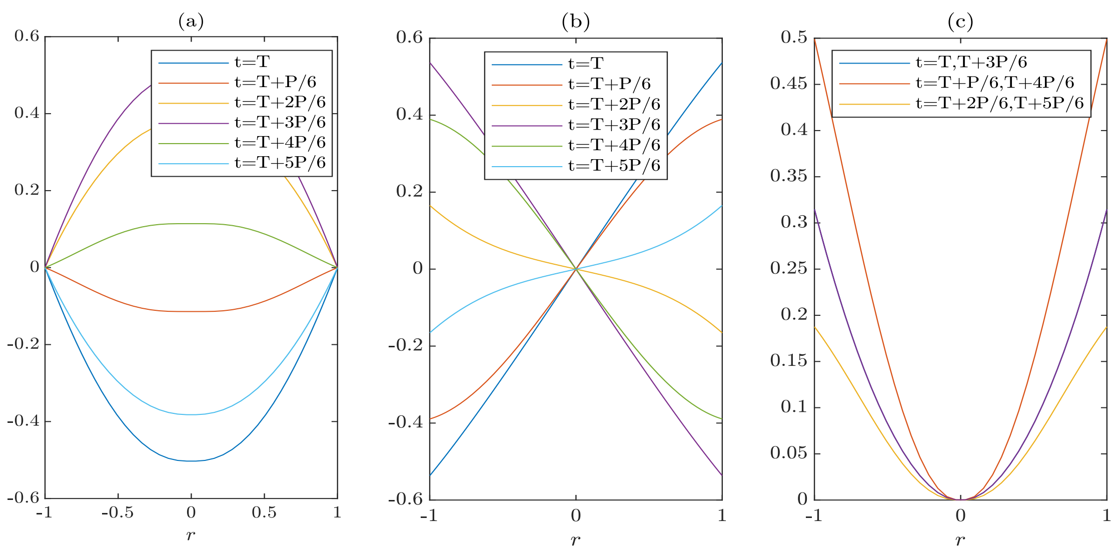

Figure 7.16: Computed solutions with parameters $\lambda_1 = 1.923$, $\lambda_2 = 0.127$, $\beta = 0.2$, $\mathrm{Wo} = 0.2365$ with cosine pressure gradient (6.103) and Powell-Eyring viscosity model (2.14) with $\Lambda = 140$. The velocity profile $u_z(r,t)$ and stress profiles $S_{rz}(r,t)$ and $S_{zz}(r,t)$ are plotted in figures (a), (b) and (c), respectively, over one period with $T = 16\pi$ using $N = 25$ points.

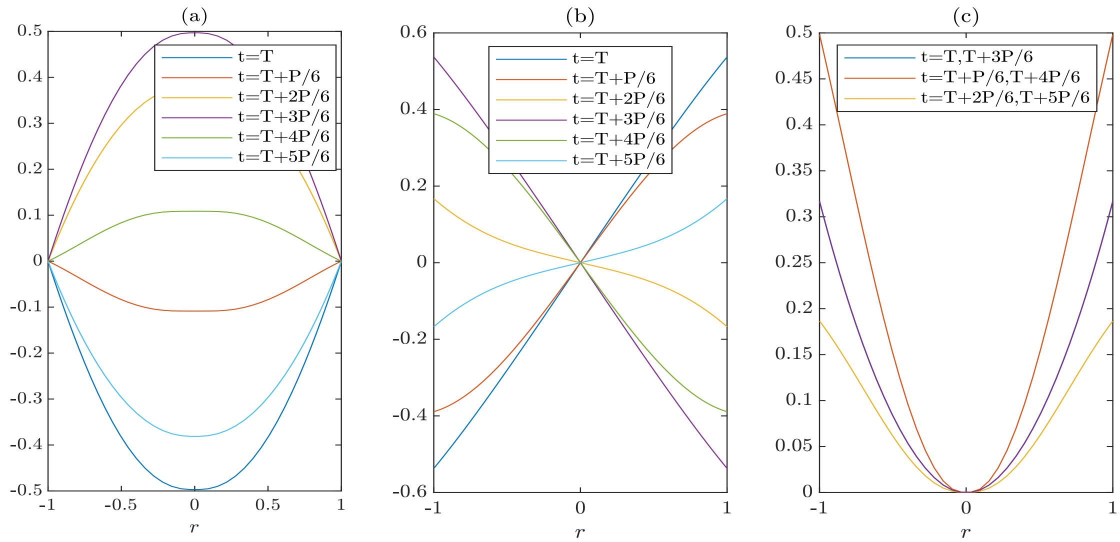

Figure 7.17: Computed solutions with parameters $\lambda_1 = 1.923$, $\lambda_2 = 0.127$, $\beta = 0.2$, Wo $=$ 0.2365 with cosine pressure gradient (6.103) and Yeleswarapu viscosity model (2.17) with $\Lambda = 140$. The velocity profile $u_z(r,t)$ and stress profiles $S_{rz}(r,t)$ and $S_{zz}(r,t)$ are plotted in figures (a), (b) and (c), respectively, over one period with $T = 16\pi$ using $N = 25$ points.

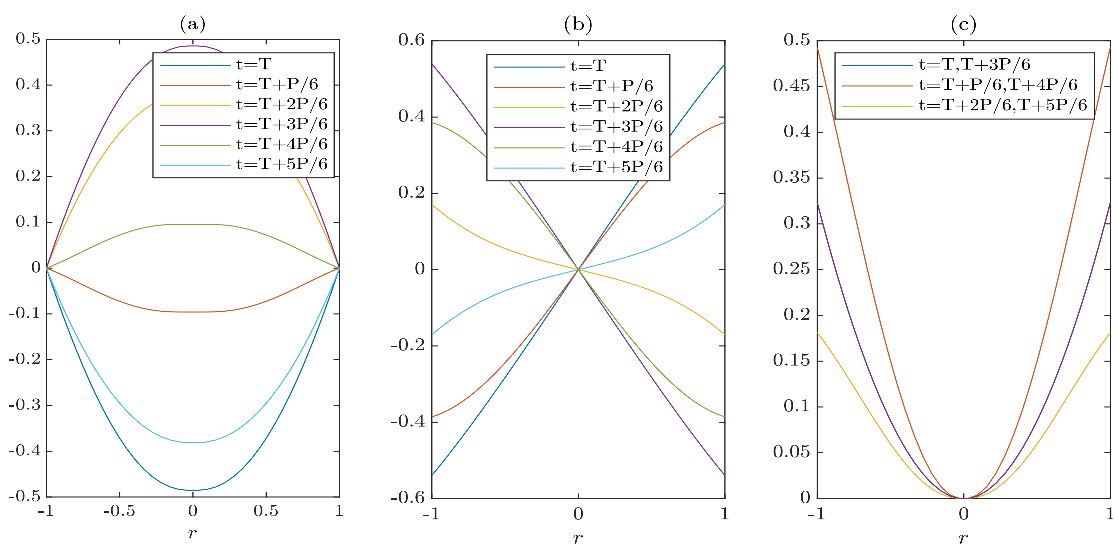

Figure 7.18: Computed solutions with parameters $\lambda_1 = 1.923$, $\lambda_2 = 0.127$, $\beta = 0.2$, Wo $=$ 0.2365 with cosine pressure gradient (6.103) and Carreau viscosity model (2.23) with $\Lambda = 140$. The velocity profile $u_z(r,t)$ and stress profiles $S_{rz}(r,t)$ and $S_{zz}(r,t)$ are plotted in figures (a), (b) and (c), respectively, over one period with $T = 16\pi$ using $N = 25$ points.

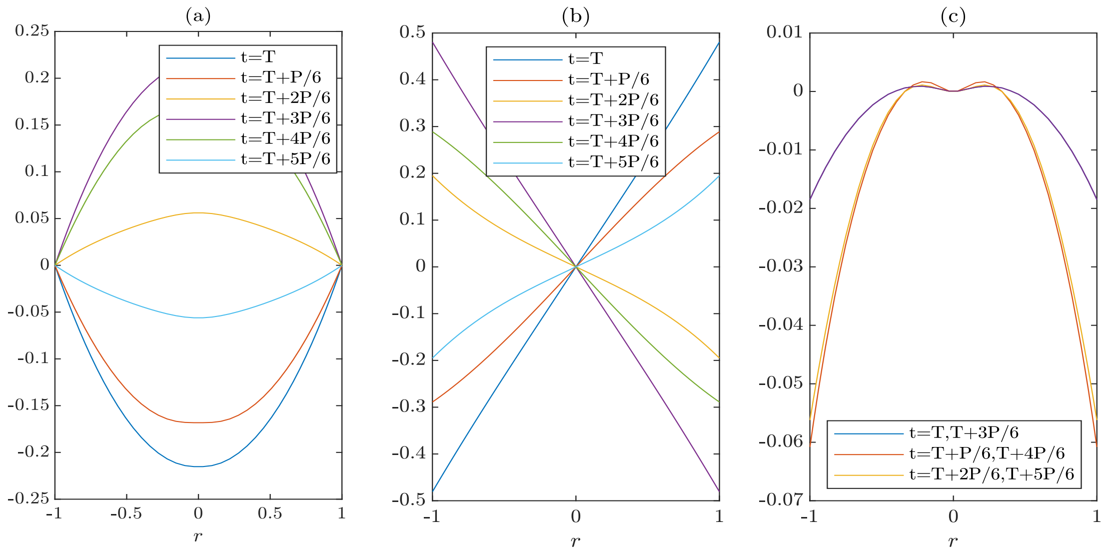

Figure 7.19: Computed solutions with parameters $\lambda_1 = 1.923$, $\lambda_2 = 0.5$, $\beta = 0.0616$, $\mathrm{Wo} = 0.2365$ with cosine pressure gradient (6.103) and Powell-Eyring viscosity model (2.14) with $\Lambda = 140$. The velocity profile $u_z(r,t)$ and stress profiles $S_{rz}(r,t)$ and $S_{zz}(r,t)$ are plotted in figures (a), (b) and (c), respectively, over one period with $T = 16\pi$ using $N = 25$ points.

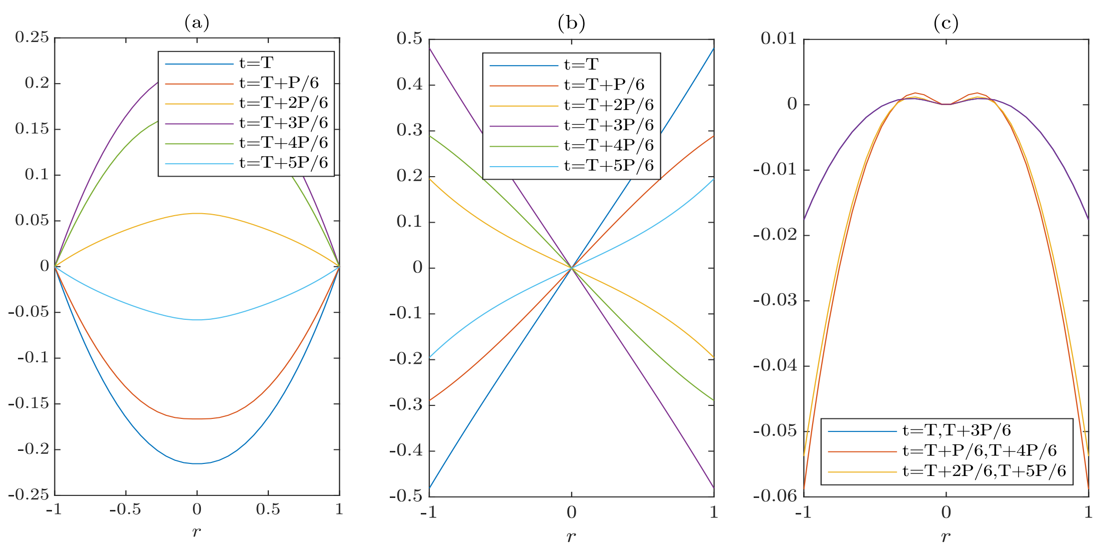

Figure 7.20: Computed solutions with parameters $\lambda_1 = 1.923$, $\lambda_2 = 0.5$, $\beta = 0.0616$, $\mathrm{Wo} = 0.2365$ with cosine pressure gradient (6.103) and Yeleswarapu viscosity model (2.17) with $\Lambda = 140$. The velocity profile $u_z(r,t)$ and stress profiles $S_{rz}(r,t)$ and $S_{zz}(r,t)$ are plotted in figures (a), (b) and (c), respectively, over one period with $T = 16\pi$ using $N = 25$ points.

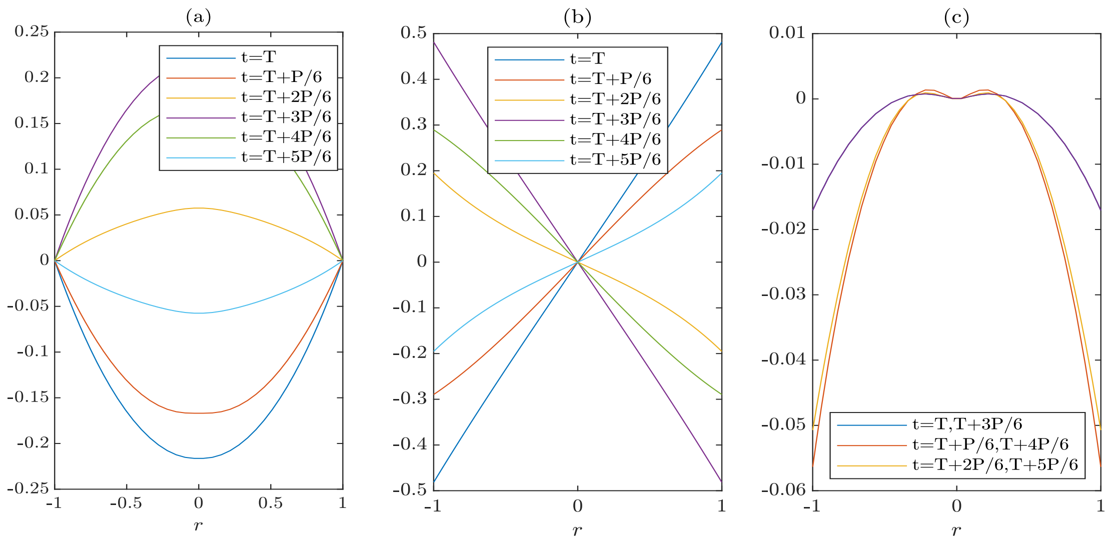

Figure 7.21: Computed solutions with parameters $\lambda_1 = 1.923$, $\lambda_2 = 0.5$, $\beta = 0.0616$, $\mathrm{Wo} = 0.2365$ with cosine pressure gradient (6.103) and Carreau viscosity model (2.23) with $\Lambda = 140$. The velocity profile $u_z(r,t)$ and stress profiles $S_{rz}(r,t)$ and $S_{zz}(r,t)$ are plotted in figures (a), (b) and (c), respectively, over one period with $T = 16\pi$ using $N = 25$ points.

the problem over one period with start time $T = 16\pi$ using the Powell-Eyring viscosity model (2.14), the Yeleswarapu model (2.17) and the Carreau model (2.23) are depicted in Figure 7.19, Figure 7.20, and Figure 7.21, respectively. The effect of this change in relaxation time is to significantly reduce the amplitudes of the velocity $u_z(r,t)$ and normal stress S_{zz} stress, shift its phase by 90 degrees. There were only small changes to the S_{rz} stress. The velocity $u_z(r,t)$ and shear stress $S_{rz}(r,t)$ are 2π-periodic functions, while the normal stress $S_{zz}(r,t)$ is a π-periodic function of time.

7.3 Moderate Womersley Number Problems

Based on the results of the previous section, it's pretty clear that the Powell-Eyring viscosity model (2.14), the Yeleswarapu model (2.17) and the Carreau model (2.23) all predict similar results (with perhaps some over prediction of the S_{zz} stress by the Carreau model that needs to be studied a little further). For this reason, in what follows, we will limit the presentation of results to the Powell-Eyring model at moderate Womersley numbers. While cases of moderate Womersley number are less representative of blood flow problems, the behaviour of the solutions here are actually quite informative on how we may expect the system to respond to perturbations in the input pressure gradient $f(t)$.

In what follows, we set the Womersley number at $\mathrm{Wo} = 30$ with other parameters fixed as per equation (7.1). Solutions of the problem over one period with start time $T = 16\pi$ using the Powell-Eyring viscosity model (2.14) are depicted in Figure 7.22. What immediately should be noted is that each the velocity $u_z(r,t)$, shear stress $S_{rz}(r,t)$ and normal stress $S_{zz}(r,t)$ are all 2π-periodic functions of time. This stands in clear contrast to the case of low Womersley numbers detailed above, where the normal stress $S_{zz}(r,t)$ is a π-periodic function of time. Also note that the shear stress profile $S_{rz}(r,t)$ is slightly asymmetric. What is happening here is that the development time $T = 16\pi$ has not been sufficent for the solution to reach its periodic steady state, and due to the nonlinear nature of the time evolution of the problem, multiple frequencies contribute to the solution at this stage.

In order to investigate things further, we repeat the numerical experiments above while extending the flow development time T. Solutions of the problem over one period with $T = 48\pi$ using the Powell-Eyring viscosity model (2.14) are depicted in Figure 7.23. Still, at this stage, the velocity $u_z(r,t)$, shear stress $S_{rz}(r,t)$ and normal stress $S_{zz}(r,t)$ are all 2π-periodic functions of time, albeit the normal stress is very nearly π-periodic. Further increasing the development time to $T = 96\pi$ results in the velocity $u_z(r,t)$ and shear stress $S_{rz}(r,t)$ being 2π-periodic functions, while the normal stress $S_{zz}(r,t)$ being a π-periodic function of time; see Figure 7.24.

We can summarize these observations as follows. Flows corresponding to moderate Womersley numbers Wo require longer development times T than low Womersley number flows in order to reach a steady state when the system is started from rest. The evolution of the flow in this development stage is nonlinear with multiple frequencies contributing to the time evolution of the problem. The nonlinear contributions from multiple frequencies, which are essentially transient, are primarily isolated to a boundary layer near the tube wall.

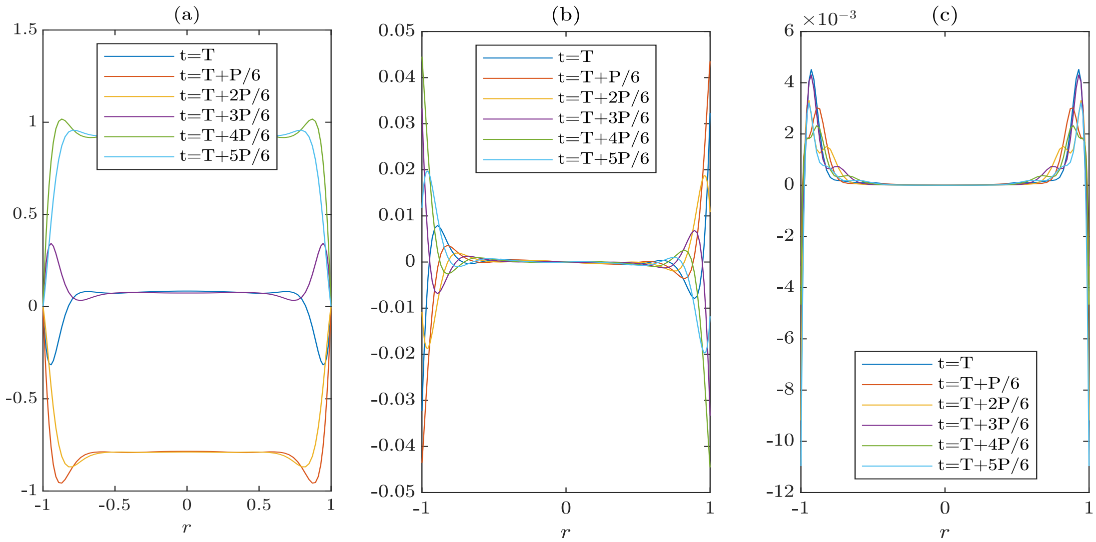

Figure 7.22: Computed solutions with parameters $\lambda_1 = 1.923$, $\lambda_2 = 0.127$, $\beta = 0.0616$, $\mathrm{Wo} = 30$ with cosine pressure gradient (6.103) and Powell-Eyring viscosity model (2.14) with $\Lambda = 140$. The velocity profile $u_z(r,t)$ and stress profiles $S_{rz}(r,t)$ and $S_{zz}(r,t)$ are plotted in figures (a), (b) and (c), respectively, over one period with $T = 16\pi$ using $N = 35$ points.

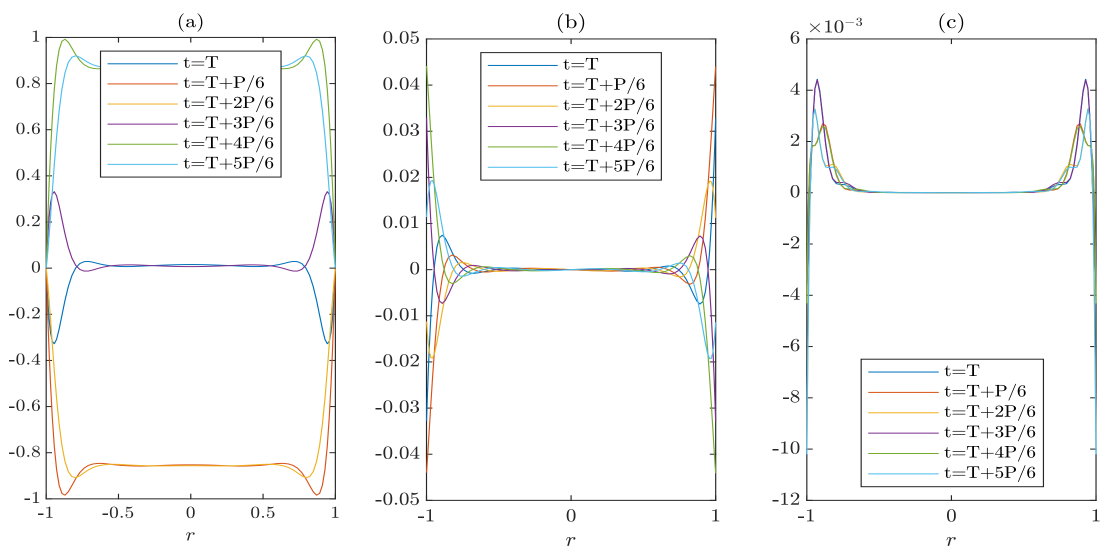

Figure 7.23: Computed solutions with parameters $\lambda_1 = 1.923$, $\lambda_2 = 0.127$, $\beta = 0.0616$, $\mathrm{Wo} = 30$ with cosine pressure gradient (6.103) and Powell-Eyring viscosity model (2.14) with $\Lambda = 140$. The velocity profile $u_z(r,t)$ and stress profiles $S_{rz}(r,t)$ and $S_{zz}(r,t)$ are plotted in figures (a), (b) and (c), respectively, over one period with $T = 48\pi$ using $N = 35$ points.

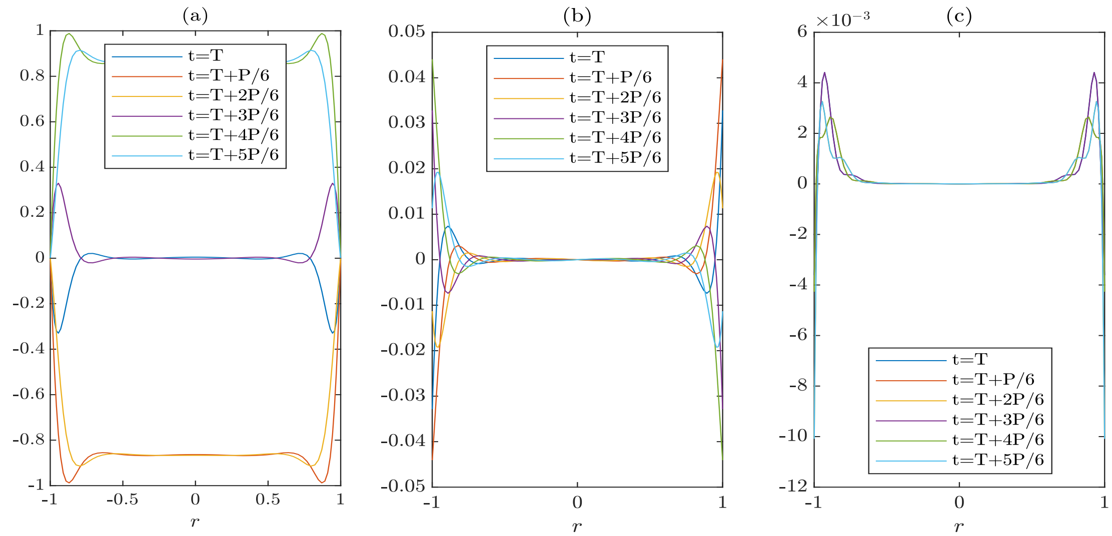

Figure 7.24: Computed solutions with parameters $\lambda_1 = 1.923$, $\lambda_2 = 0.127$, $\beta = 0.0616$, $\mathrm{Wo} = 30$ with cosine pressure gradient (6.103) and Powell-Eyring viscosity model (2.14) with $\Lambda = 140$. The velocity profile $u_z(r, t)$ and stress profiles $S_{rz}(r, t)$ and $S_{zz}(r, t)$ are plotted in figures (a), (b) and (c), respectively, over one period with $T = 96\pi$ using $N = 35$ points.

That is, critical nonlinear evolution processes that ultimately result in the periodic steady state play out mostly in the boundary layers. While we leave this issue for future work, we expect that if we were to perturb the steady state with a pressure pulse (say a pressure function with a Gaussian envelope) then we would expect multiple frequencies to be excited for a short time, whose contributions will be primarily visible in the fluid boundary layers. Contributions from these excited frequencies will die over time as the pulse passes and the flow settles back down into its steady state.

7.4 High Womersley Number Problems

In order to present results describing solutions over a range of Womersley numbers Wo, in what follows, we briefly document flows corresponding to a high Womersley number $\mathrm{Wo} = 100$. As in the case of moderate Womersley numbers, we limit the presentation of results to the Powell-Eyring model for viscosity.

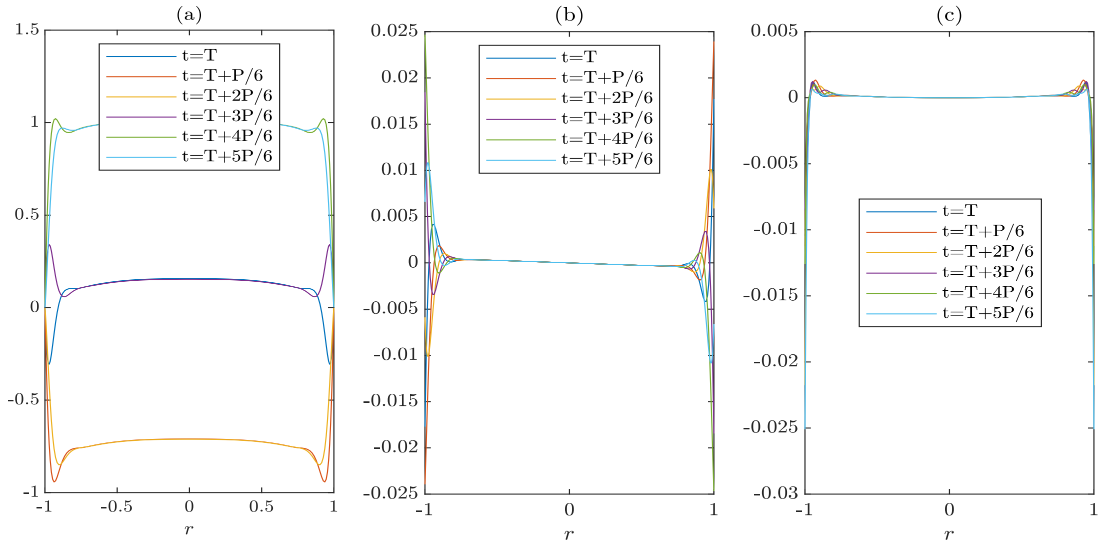

Figure 7.25: Computed solutions with parameters $\lambda_1 = 1.923$, $\lambda_2 = 0.127$, $\beta = 0.0616$, Wo $= 100$ with cosine pressure gradient (6.103) and Powell-Eyring viscosity model (2.14) with $\Lambda = 140$. The velocity profile $u_z(r,t)$ and stress profiles $S_{rz}(r,t)$ and $S_{zz}(r,t)$ are plotted in figures (a), (b) and (c), respectively, over one period with $T = 20\pi$ using $N = 55$ points.

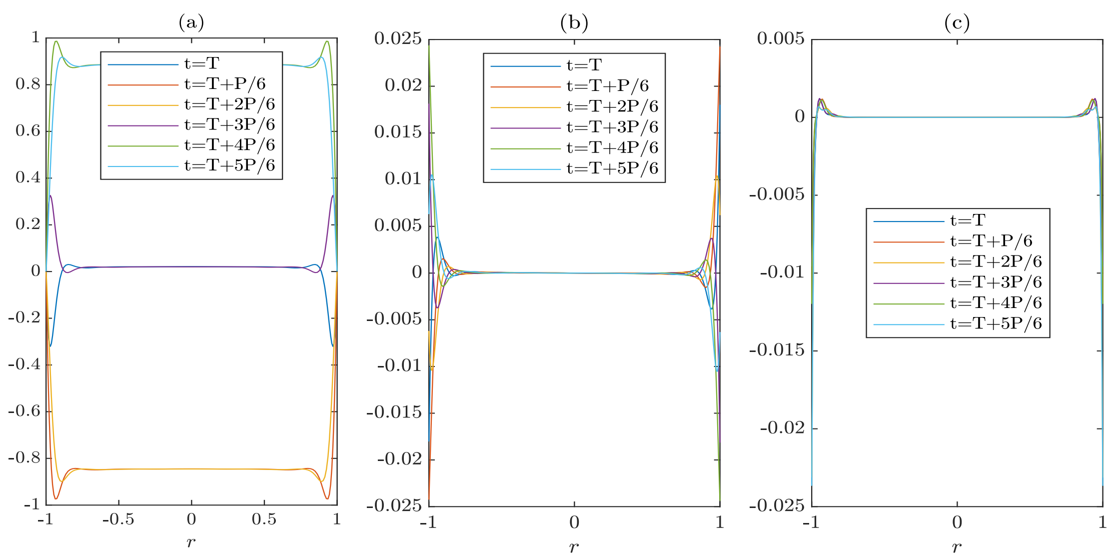

Figure 7.26: Computed solutions with parameters $\lambda_1 = 1.923$, $\lambda_2 = 0.127$, $\beta = 0.0616$, Wo $= 100$ with cosine pressure gradient (6.103) and Powell-Eyring viscosity model (2.14) with $\Lambda = 140$. The velocity profile $u_z(r,t)$ and stress profiles $S_{rz}(r,t)$ and $S_{zz}(r,t)$ are plotted in figures (a), (b) and (c), respectively, over one period with $T = 100\pi$ using $N = 55$ points.

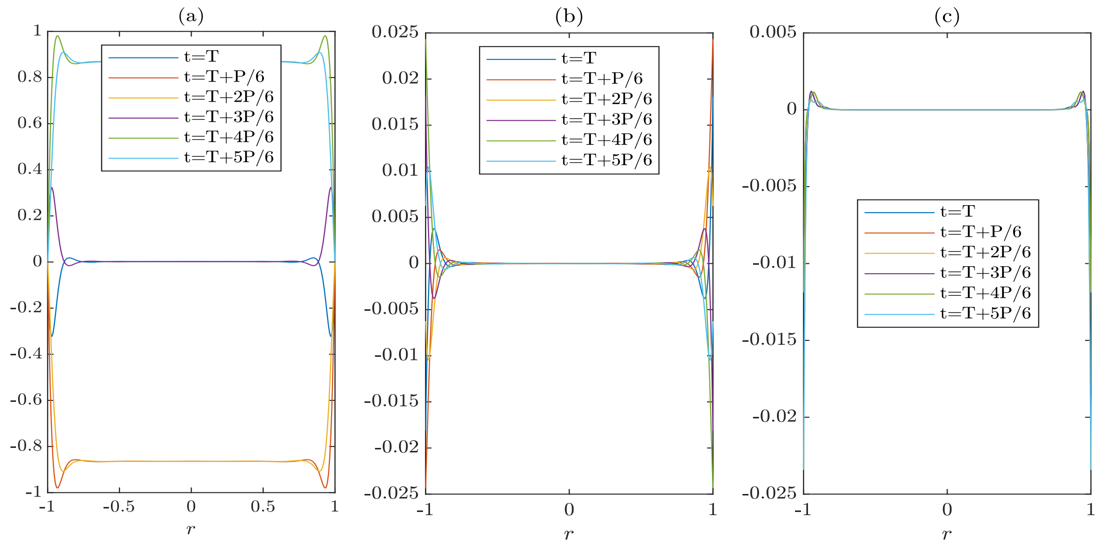

Figure 7.27: Computed solutions with parameters $\lambda_1 = 1.923$, $\lambda_2 = 0.127$, $\beta = 0.0616$, $\mathrm{Wo} = 100$ with cosine pressure gradient (6.103) and Powell-Eyring viscosity model (2.14) with $\Lambda = 140$. The velocity profile $u_z(r,t)$ and stress profiles $S_{rz}(r,t)$ and $S_{zz}(r,t)$ are plotted in figures (a), (b) and (c), respectively, over one period with $T = 200\pi$ using $N = 55$ points.

Setting the Womersley number at $\mathrm{Wo} = 100$ with other parameters fixed as per equation (7.1), solutions of the problem over one period with start time $T = 20\pi$ using the Powell-Eyring viscosity model (2.14) are depicted in Figure 7.25. The velocity $u_z(r,t)$, shear stress $S_{rz}(r,t)$ and normal stress $S_{zz}(r,t)$ are all 2π-periodic functions of time; clearly the development time $T = 20\pi$ has not been sufficiently long for the system to reach its expected steady state where the normal stress is a π-periodic functions of time. Nonlinear contributions to the flow are visible in a neighborhood of the tube wall. Solutions for the same problem with a longer development time $T = 100\pi$ are depicted in Figure 7.26. Again, in this case, the development time $T = 100\pi$ has not been sufficiently long for the system to reach its expected steady state. Further increasing the development time to $T = 200\pi$ results in the velocity $u_z(r,t)$ and shear stress $S_{rz}(r,t)$ being 2π-periodic functions, while the normal stress $S_{zz}(r,t)$ being a π-periodic function of time; see Figure 7.27.

What should be clear from this look at high Womersley numbers is that these flows require even longer development times T to reach a steady state flow than do flows corresponding to low or moderate Womersley numbers when the system is started from rest. The transient nonlinear contributions to the flow are further isolated to a narrow boundary layer near the tube wall. Any perturbation to the steady state flow should excite multiple frequencies whose contributions are primarily visible in the boundary layers. Contributions from these excited frequencies will take much longer to die out after a perturbation in the pressure gradient than in low and moderate Womersley number flows.

Chapter 8

Conclusions and Future Work

This thesis presents an efficient Chebyshev-tau spectral solver solver to compute numerical solutions of the equations of motion of a viscous fluid subject to the Generalized Oldroy-B stress model corresponding to the flow of a viscoelastic fluid with a shear rate dependent viscosity function. The code relies on a fourth order Runge-Kutta time stepping procedure with $\mathcal{O}(N\log N)$ operations per time step, enabled by the use of fast cosine transforms. A comparison of code results with known solutions in the case of linear flows indicates that the solution converges very rapidly in the number of unknowns. This solver is a significant improvement to what was previously available for this problem [1, 14] and allows us to compare results corresponding to different shear rate dependent viscosity models by Powell-Eyring, Yeleswarapu and Carreau over long evolution times.

Our comparison of viscosity models did not produce any clear favorites. Indeed, results from all three models studies were strikingly similar, with perhaps some over prediction of the S_{zz} stress by the Carreau model that needs to be studied a little further. One issue that arises with the Yeleswarapu viscosity model is that it's not strictly even about $\dot{\gamma} = 0$. This is an issue, since the argument it accepts is the absolute value of the non-dimensional shear rate $\dot{\gamma}$. The result is that the fourth derivative of the Yeleswarapu viscosity model is actually singular in a neighborhood of $\dot{\gamma} = 0$. Such singularities cannot be physical and have implications for the convergence rates of the numerical algorithms applied; while the limitations are not severe in this case, a spectral convergence rate in the numerical algorithm cannot be achieved as a result. Viscosity models that are even functions of $\dot{\gamma}$ do not suffer from these self-inflicted problems and are likely more physically realistic models on that basis. We would on this basis recommend the use of the Powell-Eyring or Carreau models.

In our numerical studies at low Womersley numbers, which are most significant in blood flow applications, the following dependence of computed solutions on the parameters of the problem became apparent:

(1) The effect of an increase in the Womersley number Wo is to increase the amplitude of the velocity profile and decrease the amplitudes of the stress profiles.

(2) The effect of a decrease in the shear thinning parameter Λ is an increase in the amplitude of the normal stress S_{zz} with only small changes to the other flow quantities.

(3) The effect of an increase in the viscosity ratio β is to decrease the amplitude of the velocity $u_z(r,t)$, increase the amplitude of the shear stress $S_{rz}(r,t)$, and to significantly increase the amplitude of the normal stress $S_{zz}(r,t)$.

(4) The effect of an increase to the relaxation time λ_2 is to significantly reduce the amplitudes of the velocity $u_z(r,t)$ and normal stress $S_{zz}(r,t)$, also shifting the phase of the normal stress. Only small changes to the shear stress $S_{rz}(r,t)$ result.

While the main themes of this thesis deal with steady state solutions of the problem, our observations on the transient behavior of the system are interesting and warrant further study in the future. The development time T for a flow, initially at rest, to reach a periodic steady state increases with the Womersley number Wo. The transient flows which exist for $t < T$ are characterized by nonlinear contributions to the field quantities from a range of frequencies; the transient solutions are not simply π or 2π periodic as in the linear case. These transient contributions to the field quantities are primarily isolated to a narrow boundary layer near the tube wall. We expect that if we were to perturb the steady state with a pressure pulse (say a pressure function with a Gaussian envelope) then we would see multiple frequencies excited for a short time, whose contributions will be primarily visible in the fluid boundary layers. Contributions to the flow quantities from these excited frequencies will die over time as the pulse passes and the flow settles back down into its steady state. We plan to carry out a detailed study of transient solutions along these lines.

Another interesting application area to which the current work can be extended is the flow of oil in pipelines. This may require some minor modification of the constitutive relations so that they are more suitable in approximating the physical behaviour of a different fluid, but in principle the changes should be minor.

Bibliography

[1] K.K. Yeleswarapu, M.V. Kameneva, K.R. Rajagopal, and J.F. Antaki. "The flow of blood in tubes: theory and experiment". In: *Mechanics Research Communications* 25 (3 1998), pp. 257–262.

[2] S. Uchida. "The pulsating viscous flow superimposed on the steady laminar motion of incompressible fluid in a circular pipe". In: *Zeitschrift für angewandte Mathematik und Physik* 7 (1956), pp. 403–422.

[3] M. Zamir. "Mechanics of pulsatile flow in a tube". In: *Comments Theo Bio* 4 (1996), pp. 31–61.

[4] D.N. Ku. "Blood flow in arteries". In: *Annu. Rev. Fluid Mech.* 29 (1997), pp. 399–434.

[5] T. Sexl. "Über den von E.G. Richardson entdeckten "Annulareffekt"". In: *Zeitschrift für Physik* 61 (1930), pp. 349–362.

[6] J.R. Womersley. "Oscillatory motion of a viscous liquid in a thin-walled elastic tube -I: The linear approximation for long waves". In: *Philisophical Magazine* 46 (1955), pp. 199–221.

[7] T. Bodnar, A. Sequeira, and M. Prosi. "On the shear-thinning and viscoelastic effects of blood flow under various flow rates". In: *Applied Mathematics and Computation* 217 (2011), pp. 5055–5067.

[8] N. Bessonov, A. Sequeira, S. Simakov, Y. Vassilevski, and V. Volpert. "Methods of Blood Flow Modelling". In: *Mathematical Modelling of Natural Phenomena* 11 (1 2016), pp. 1–25.

[9] J.G. Oldroyd. "On the formulation of rheological equations of state". In: *Proc. R. Soc. Lond. Ser. A* 200 (1063 1950), pp. 523–541.

[10] M. Renardy and B. Thomases. "A mathematician's perspective on the Oldroyd B model: Progress and future challenges". In: *Journal of Non-Newtonian Fluid Mechanics* 239 (2021), p. 104573.

[11] M. Anand and K.R. Rajagopal. "A shear-thinning viscoelastic fluid model for describing the flow of blood". In: *International Journal of Cardiovascular Medicine and Science* 4 (2 2004), pp. 59–68.

[12] N. Sun and D. DeKee. "Simple shear, hysteresis, and yield stress in biofluids". In: *Canadian Journal of Chemical Engineering* 79 (2001), pp. 36–41.

[13] R.G. Owens. "A new microstructure-based constitutive model for human blood". In: *Journal of Non-Newtonian Fluid Mechanics* 140 (1-3 2006), pp. 57–70.

[14] G. Pontrelli. "Pulsatile Blood Flow in a Pipe". In: *Computers & Fluids* 27 (3 1998), pp. 367–380.

[15] J.N. Reddy. *An Introduction to Continuum Mechanics*. 2nd ed. Cambridge University Press, 2013.

[16] W.P. Graebel. *Advanced Fluid Mechanics*. Academic Press, 2007.

[17] A. Morozov and S.E. Spagnolie. "Introduction to Complex Fluids". In: *Complex Fluids in Biological Systems: Experiment, Theory, and Computation*. Springer New York, 2015, pp. 3–52.

[18] M. Zamir. *The Physics of Pulsatile Flow*. Biological Physics Series. Springer Verlag, 2000.

[19] S.H. Maslen. "Transverse velocities in fully developed flows". In: *Quarterly of Applied Mathematics* 16 (1958), pp. 173–175.

[20] K.D. Rahaman and H. Ramkissoon. "Unsteady axial viscoelastic pipe flows". In: *Journal of Non-Newtonian Fluid Mechanics* 57 (1995), pp. 27–38.

[21] M. Abramowitz and I.A. Stegun. *Handbook of Mathematical Functions with Formulas, Graphs, and Mathematical Tables*. Applied mathematics series. U.S. Government Printing Office, 1964.

[22] G.N. Watson. *A treatise on the theory of Bessel functions*. 2nd ed. Cambridge University Press, 1944.

[23] J.C. Mason and D.C. Handscomb. *Chebyshev polynomials*. Chapman & Hall/CRC, 2003.

[24] T.J. Rivlin. *Chebyshev Polynomials: From Approximation Theory to Algebra and Number Theory*. 2nd ed. Pure and Applied Mathematics: A Wiley Series of Texts, Monographs and Tracts ; v. 10. John Wiley & Sons Inc., 1990.

[25] W.H. Press, S.A. Teukolsky, W.T. Vetterling, and B.P. Flannery. *Numerical Recipes: The Art of Scientific Computing*. 2nd ed. Vol. 1. Cambridge University Press, 1992.

[26] URL: `http://www.fftw.org/`.

[27] R.G. Owens and T.N. Phillips. *Computational Rheology*. Imperial College Press, 2002.

[28] C. Canuto, M.Y. Hussaini, A. Quarteroni, and T.A. Zang. *Spectral Methods in Fluid Dynamics*. Springer Series in Computational Physics. Springer Verlag, 1988.

[29] H.M. Srivastava and H.L. Manocha. *A Treatise on Generating Functions*. Ellis Horwood Series in Mathematics and its Applications. Halsted Press, 1984.

[30] J.C. Butcher. *The Numerical Analysis of Ordinary Differential Equations: Runge-Kutta and General Linear Methods*. Wiley-Interscience, 1987.